LBL-28968

Center for Advanced Materials

CAM

Weldment Mechanical Properties of Aluminum-Copper-Lithium Alloy, 2090, at Ambient and Cryogenic Temperatures

A.J. Sunwoo
(Ph.D. Thesis)

May 1990

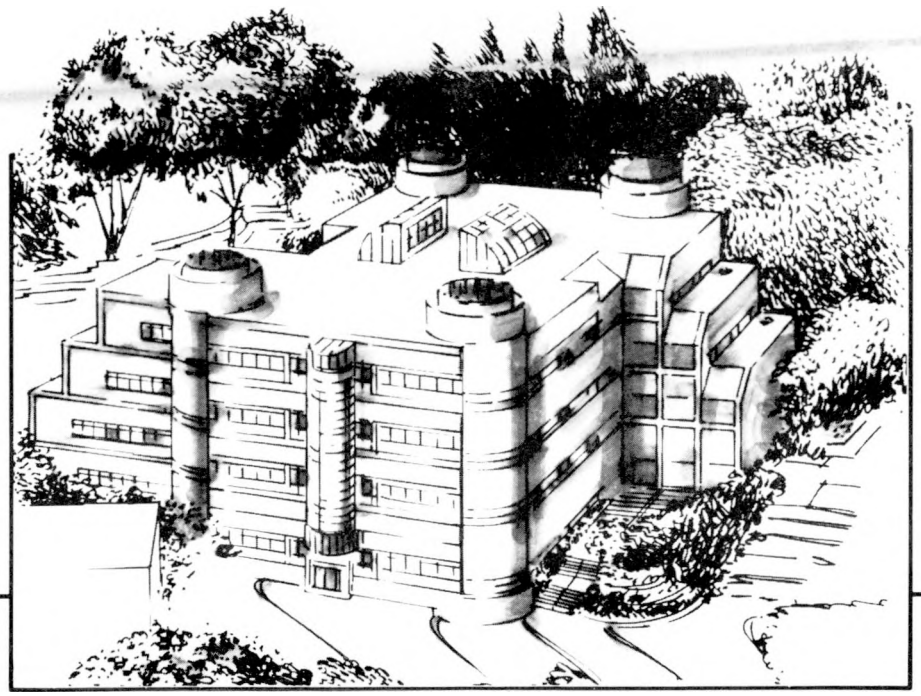

Materials and Chemical Sciences Division

Lawrence Berkeley Laboratory • University of California

ONE CYCLOTRON ROAD, BERKELEY, CA 94720 • (415) 486-4755

Prepared for the U.S. Department of Energy under Contract DE-AC03-76SF00098

LBL--28968

DE90 014178

WELDMENT MECHANICAL PROPERTIES OF ALUMINUM-COPPER-LITHIUM ALLOY, 2090, AT AMBIENT AND CRYOGENIC TEMPERATURES

Anne Jin Sunwoo

Ph.D. Dissertation

Department of Materials Science and Mineral Engineering
University of California, Berkeley

and

Center for Advanced Materials
Materials and Chemical sciences Division
Lawrence Berkeley Laboratory
1 Cyclotron Road
Berkeley, California 94720

May 1990

This work is funded by the Director, Office of Energy Research, Office of Basic Energy Science, Materials Sciences Division of the U.S. Department of Energy under Contract No. DE-AC03-76SF00098

WELDMENT MECHANICAL PROPERTIES OF ALUMINUM-COPPER-LITHIUM ALLOY, 2090, AT AMBIENT AND CRYOGENIC TEMPERATURES

Anne Jin Sunwoo

ABSTRACT

Weldment mechanical properties of Al-Cu-Li alloy, 2090, at ambient and cryogeinc temperatures have been investigated. The primary objective of this work is to develop a mechanistic understanding of the weldment mechanical properties with specific emphasis on their relation to the fusion zone and heat affected zone microstructures.

In the fusion zone, prior thermomechanical processing of the base metal is erased during welding. The as-welded and post-weld heat treated fusion zones lack the precipitates, size, volume fraction, and homogeneity of the base metal. The T_1 precipitates are found either in the vicinity of other intermetallics or at the boundaries. Low weldment elongation is caused by the formation of intermetallics and continous film on the boundaries.

Even with alloy addition to the fusion zone, the strength mismatch continues to exist due to the difference in strengthening mechanism: solid solution strengthening in the fusion zone and precipitation strengthening in the base metal. The ultimate tensile strength of the as-welded weldments is only 50% of the base metal yield strength, and localized deformation occurs in the softer fusion zone. A weldment elongation increases substantially with increasing Cu content in the fusion zone at both test temperatures. Magnesium additions to the fusion zone change the dendrite morphology, affecting the distribution of Cu segregation at the boundaries. The Mg welds show higher yield strengths, but the Cu-Mg combination leads to embrittlement.

The difference in properties of the heat affected zone and the base metal is primarily caused by the dissolution of strengthening phases. At 578 K, the strength degrades due to dissolution of δ' phase and at 773 K, dissolution of T_1 phase. At 648 K, the growth of the equilibrium phases occurs: T_1 at both the matrix and the subgrain boundaries, and T_2 at the grain boundaries. The problem region in the weldment will be the partially melted region and the fusion boundary. This is due to dissolution of the strengthening phases in the matrix and the formation of equilibrium phases and intermetallics at the boundaries.

Table of Contents

I. INTRODUCTION

A. MOTIVATION FOR THE STUDY

Aluminum-lithium alloys are of considerable interest to the aircraft and aerospace industries since they have the potential to reduce overall density by 7-10% and to increase specific elastic modulus by 10-12%, as compared to other commercially available Al alloys. The specific advantage of the alloy 2090-T81 is that the strength-toughness combination of 2090-T81 increases substantially as temperature is decreased from 293 K to 4 K [Glazer, 1989]. Since these cryogenic mechanical properties of 2090-T81 may be useful in cryogenic tankage for aerospace structure, many studies [Feng, et al., 1984; Wyss and Sanders, 1988; Glazer, et al., 1986] have been dedicated to the overall understanding of the microstructure and mechanical properties of 2090.

An important possible application considered for 2090 is cryogenic fuel tankage for space vehicles, which requires a welded construction. Limited work has been done to understand the weldability of 2090. Most of the relevant studies have focused on the hot cracking susceptibility [Cross et.al.,1986; Lippold,1989, Kramer, et al., 1989]. There are other critical weldability issues that must be addressed, such as susceptibility to fusion zone porosity, degradation of the as-welded and post-weld aged mechanical properties, and environmental effects.

There are three distinct regions in the weldment: the fusion zone, the heat affected zone, and the unaffected base metal. The fusion zone is the region where the metal has been melted and resolidified so that prior thermomechanical processing of the base metal has been erased. The weld properties are mainly governed by the as-cast microstructure and the solute distribution in the fusion zone. The heat affected zone (HAZ), on the other hand, is created adjacent to the fusion zone due to heat conduction from the molten metal during welding. Because the HAZ is a transition region between the fusion zone and the unaffected base metal, a temperature gradient was present. The microstructural and property changes at a particular point in the HAZ depends on the peak temperature of the thermal cycle at that point. The unaffected base metal in the weldment maintains its initial mechanical properties.

There are many problems associated with producing a sound weld [Martukantz, et al., 1987; Sunwoo and Morris, 1989], including particularly the strength mismatch and low ductility in the weldments. In many cases, the base metal is peak-aged prior to welding to attain high strength-toughness combination, and the weldment is utilized in the as-welded condition. The difference in thermomechanical processing between the parent metal and the weld results in inferior weldment properties.

B. OBJECTIVES

In the present work, processing issues such as the fusion zone porosity and hot cracking sensitivity were addressed only as far as necessary to produce sound welds. The primary objective of this work was to develop a mechanistic understanding of the weldment mechanical properties with special emphasis on their relation to the fusion zone and heat affected zone microstructures. With this understanding, the improvement of weld properties can be effectively approached. In addition, the as-welded and post-weld-aged weldment mechanical properties at temperature can be helpful input to cryogenic tank design.

This work is divided in two parts, based on the two regions in the weldment: the fusion zone and the heat affected zone. A material's properties (including weld properties) are determined by the chemistry and microstructure. The microstructure, in turn, is determined by its chemistry and processing. To study weld properties systematically, therefore, the effects of processing were first studied, and then the influence of chemistry on the microstructure and properties of the weld. The advantage of this approach is that only one variable is changed at a time, providing more controlled study. Thus, any changes in the fusion zone microstructure and weld properties will be caused by the effects of processing. Otherwise, the alloy addition during welding simultaneous changes the microstructure, and both the microstructure and chemistry will influence the weld properties.

The objective of the processing study was to determine the effects of welding processes and various post-weld heat treatments on the fusion zone microstructure and solute/precipitate distribution and correlate them to the as-welded and aged weld mechanical properties. The objective of the chemistry study was to examine the influence of various alloy additions to the 2090 fusion zone in the simulated industrial welding condition.

The heat affected zone of the weldment is studied since 2090 is a precipitation-strengthened alloy and any thermal cycle will be affect the precipitation behavior. The HAZ study investigates the influence of the HAZ peak temperatures on the microstructure and properties of 2090.

II. BACKGROUND

A. AL-CU-LI ALLOY, 2090

The chemistry and thermomechanical processing of 2090-T81 [Rioja, et al., 1986] has been primarily studied in detail and adjusted to produce the desired properties. The nominal composition of 2090 is, in wt-%, 3.0 Cu-2.2 Li-0.12 Zr-Al. Conventional thermomechanical processing consists of homogenization, cold rolling to 4.3mm (0.17in) sheet, solution heat treatment, stretch for 4.6%, and then peak-age. This procedure produces a favorable combination of the volume fraction, size, and distribution of the strengthening phases, ensuing high strength.

The precipitates present in aged 2090 [Gregson and Flower, 1987; Tosten, et al., 1988] are summarized in Table II.1. The δ' is an ordered, coherent phase that tends to precipitate during quenching from solution heat treatment [Noble and Thompson, 1971, Khachaturyan, et al, 1988, Jensrud and Ryum, 1984]. Both θ' and T_1 are semicoherent phases that precipitate during subsequent aging. Of these, the equilibrium phase T_1 is the most dominant strengthening phase and tends to form on {111} matrix planes and at the subgrain boundaries. The other equilibrium precipitate present is the $T_2(Al_6CuLi_3)$ [Bartage, et al., 1987] that forms at the grain boundaries and adversely affects the elongation. The small addition of Zr to 2090 results in the formation of $\beta'(Al_3Zr)$ which is a metastable, coherent dispersoid that tends to precipitate during homogenization [Gregson and Flower, 1987; Gu. et al, 1985]. The β' stabilizes the subgrain structure and suppresses recrystallization during subsequent processing.

Table II.1 The precipitates that are present in aged 2090.

Phase	Composition	Crystal Structure	Morphology and Habit Plane	
δ'	Al_3Li	$L1_2$ (FCC)	spherical	on β' and θ'
β'	Al_3Zr	$L1_2$	spherical	
θ'	Al_2Cu	tetragonal	plate	{100}
T_1	Al_2CuLi	hexagonal	plate	{111}
T_2	Al_6CuLi_3	icosahedral	plate	{100}

B. WELDABILITY OF 2090

The factors that determine the weldability of a material are ability to produce a sound weld and the property compatibility between the weld and the parent metal. Before the weldment properties can be determined, the problems associated with welding had to be solved. The following sections present the preliminary work that was conducted to establish the welding conditions.

B.1 Problems Associated with Welding 2090

The ability to produce a sound weld is determined by the composition of the material, the welding process and procedure. Two common welding problems in this alloy are fusion zone porosity and hot cracking. Porosity is simply a gas entrapped during solidification. Proper cleaning procedure of material to be welded and controlled welding parameters should minimize porosity. However, 2090 with Li addition tends to form lithium hydride (LiH) stringers during processing [Rioja, 1989]. Then during welding, LiH decomposes and evolves hydrogen. The probability of having fusion zone porosity depends on the solidification rate of the process, limiting the time available for hydrogen to diffuse to the surface. The welding process that seems to be most susceptible to porosity is laser welding, due to combination of initial beam reflection, high thermal diffusivity of Al, and vaporization of volatile alloying elements [Marsico and Kassowsky, 1989]. In this work, the electron beam (EB) fusion zone was more susceptible to porosity than in the gas tungsten arc (GTA) fusion zone, due to faster solidification rate. To insure minimum porosity in the GTA fusion zone, welding was performed in an inert atmosphere.

Porosity is a minor defect in comparison to hot cracking. Hot cracking was initially theorized to be a rupture caused by a large solidification range and critical shrinkage strain [Pumphrey and Jennings, 1948]. However, Cross, et al. [1986] showed that a binary Al-Li alloy with a maximum solid-solution solubility of 4.0 wt-% is most susceptible to hot cracking at 2.6 wt-% lithium. Similarly, the hot cracking susceptibility of an Al-Cu alloy with a maximum solubility of 6 wt-% is greatest at about 3.0% [Clyne and Davies, 1977]. These studies have shown that 2090 is highly susceptible to hot cracking due to the amount of Cu and Li present in the alloy. It has been theorized that due to the nature of solidification, if there are enough solutes available to segregate and coat the boundaries, then that combined with shrinkage stresses will result in hot cracking. Borland [1960], and Clyne and Davies [1977] modified the previous concepts and suggested that hot cracking is influenced by the wettability of dendrites by the interdendritic eutectic liquid as well as the time available for the eutectic liquid to heal the crack.

In the current study, it was found that 2090 is sensitive to time at temperature (solidification and cooling rates) and welding arc condition (continuous vs. pulsed). For constant shrinkage stresses, hot cracking occurred during GTA welding and not during EB welding. However, hot cracking can be controlled during GTA welding by utilizing a water-cooled chill block, which increases the solidification and cooling rates.

The driving force for hot cracking is affected by the constitutional undercooling of the welding process, which controls the time available for the solutes to segregate to the dendrite boundaries as well as the dendrite morphology from columnar to equiaxed dendrites [Lees, 1946; Dvornak, et al., 1989]. The advantage of having equiaxed dendrites is that they can accommodate strain more easily and heal the incipient cracks more effectively [Spencer, et al., 1972]. Moreover, since hot cracking is an intergranular cracking phenomenon, the fine equiaxed grains require more energy to propagate the crack.

Hot cracking also occurred with the change in the GTAW arc condition from a continuous current to a pulsed current. The pulsed current technique is utilized in most cases because it reduces the overall heat input and allows for better control of penetration. Instead, pulsed current welding enhances hot cracking. At this time, there is a limited understanding of this hot cracking behavior caused by the change in the arc condition.

B.2 External Effects on the Weld Properties

The influences on the weld properties are divided into the internal effects and the external effects. The internal effects are defined as the effects caused by the fusion zone conditions such as the dendrite morphology, solute and precipitate distributions, and the external effects consider the influence of the base metal conditions such as the orientation and tempers on the weld properties. The internal effects are discussed in detail in the Chapter III.

B.2.1 Influence of the Base Metal Orientation

The 2090 microstructure is highly elongated about the rolling direction, and as such, the anisotropic mechanical behavior of 2090-T8 has been well documented and is attributed to hot rolling texture components, precipitation of certain variants of precipitates and grain shape [Fricke and Przystupa, 1989].

The orientation of the base metal at which the welds are produced is important, because fusion zone grow epitaxially from the parent metal [Savage, et al., 1965]. The fusion zone grain/dendrite structures tend to acquire the size and growth orientation from the parent grains. These dendrites grow normal to the weld pool until impingement occurs from the neighboring grains/dendrites. The dendrites with preferred orientation continue to grow [Savage and Aronson, 1966].

As a result, the difference in the GTA weldment strengths as a function of base metal orientation is found. The welds produced in parallel to the rolling direction seem to have higher strength than that of the transverse direction for the same welding conditions and parameters, as summarized in Table II.2. This may be attributed to the same mechanisms as the base metal, preferential grain growth and precipitation. To improve the poorer weld properties, henceforth, all the welds are produced transverse to the rolling direction.

Table II.2 Tensile properties of the peak-aged gas tungsten arc weldments as a function of base metal orientation.

Orientation	Yield Strength MPa(ksi)	UTS[1] MPa(ksi)	Elongation[2] (%)
parallel GTAW	375(54)	390(57)[1]	0.5
transverse GTAW	315(46)	370(54)[1]	1.0

Note: Strengths given to nearest 5 MPa and elongations given to nearest 0.5%.
[1] Fracture strength.
[2] 25.4 mm gage length.

B.2.2 Influence of the Base Metal Temper Conditions

The base metal temper conditions also have an influence on the weld properties. The base metal temper condition determines the strength mismatch between the base metal and the weld. In most applications, the base metal is utilized in the peak-aged condition while the weld is in the as-welded condition. When the influence of the base metal tempers, T3 and T8, on the as-welded EB and GTA weldment properties are compared, Table II.3, the actual weld strengths did not change with the base metal temper conditions. However, the ultimate tensile strengths of both the EB and GTA welds are too low to induce yielding in 2090-T8. The joint efficiencies of the EB and GTA weldments decrease from 68% and 63% to 41% and 30%, respectively with increasing base metal strength. In addition, the strength mismatch has a deleterious effect on the elongation of the EB weldment.

Table A.2 Tensile properties of the base metal, electron beam weldments and gas tungsten arc weldments tested at 293 K.

Base Metal Temper	σ_{YS} MPa(ksi)	σ_{UTS} MPa(ksi)	Elongation (%)
T3			
BM	280(41)	350(51)	11.0
EBW	195(28)	290(42)	5.5
GTAW	180(26)	265(39)	3.5
T8			
BM	575(83)	610(88)[1]	9.5
EBW	205(30)	285(41)[1]	1.5
GTAW	145(21)	265(38)	3.5

Note: Strengths given to nearest 5 MPa and elongations given to nearest 0.5%.
[1] Fracture strength.

C. OTHER WELDABLE AL ALLOYS

2090 was initially intended to replace the conventional high strength Al alloys, such as 2024 and 7075. Because 2090 is a promising alloy for weight-limited cryogenic applications, the weldability of 2090 is mostly compared to the 2219 (Al-6.3 Cu), which is currently being used for welded cryogenic application. 2219 contains high Cu and no Li and as such, the problems associated with welding are not a major concern. Comparison between the base metal and as-welded weld properties (Table II.4) shows that various base metal heat treatments have no influence on the weld strengths, but the elongations decrease with the higher base metal strengths.

Table II.4 Comparison between the properties of 2219 and 7075 and its respective as-welded weld properties.

	σ_{YS} MPa(ksi)	σ_{UTS} MPa(ksi)	Joint Efficiency[7] (%)	Elongation %
2219-T87[1,2]	395(57)	475(69)		10
weldment[3,4]	215(31)	310(45)	55%	2.0
2219-T62[1,2]	295(43)	415(60)		11
weldment[3,4]	215(31)	310(45)	72%	3.5
2219-T37[1,2]	345(50)	405(59)		12
weldment[3,4]	185(27)	295(43)	55%	4.0
7075-T6[5]	505(73)	600(87)		11
weldment[4,6]	310(45)	325(47)	62%	1.0
2219 weldments				
Peak-aged[3,4]	260(38)	295(43)	67%	2.5
SHT & Aged[3,4]	295(43)	415(60)	100%	9.0

Note: Strengths given to nearest 5 MPa and elongations given to nearest 0.5%.
T37=solution heat treated (SHT) and cold worked; T62/T6=SHT and aged; T87=aged T37.
[1] Nock, Holt and Sprowls, 1961.
[2] Data are from longitudinal sheet specimens, and transverse data are similar.
[3] Nelson, Kaufman and Wanderer, 1969. Welds are produced tranverse to the rolling direction on a 3.2 mm sheet.
[4] 55.8 mm gage length.
[5] Aluminum standards and data, The Aluminum Association, Inc., 1984.
[6] Welds are produced parallel to the rolling direction on a 3.2 mm sheet.
[7] A ratio of weld yield strength to base metal yield strength.

7075, on the other hand, is composed of 1.6 Cu-2.5 Mg-5.6Zn-Al. Because of the Cu addition in 7075, the alloy is highly susceptible to hot cracking [Cross and Olson, 1988]. 7075 is generally welded using 4043 (Al-5.0 Si) filler, which has very narrow

solidification range. Compared to the 2219, the strengths of both the base metal and weldment are higher due to the solute (Mg+Zn) content. Adversely, the increase in weld strength results in a decrease in weld elongation.

The improvement in weld strengths of 2219 can be accomplished with post-weld heat treatments. The post-weld heat treated properties of 2219 weldments are summarized in Table II.4. The joint efficiency of the post-weld aged weldment increases to 67% from 55% and the elongation remains the same. By homogenizing the Cu distribution in the fusion zone, compatibility in both strength and ductility is achieved between the base metal and weldment.

The 2xxx and 7xxx series alloys are the heat treatable alloys where they obtain their strengths through precipitate strengthening. The 1xxx, 3xxx, 5xxx, and 6xxx series alloys obtain their strengths through solid solution strengthening. The advantages of using these alloys in the welded applications are that the strength compatibility between the parent metal and the weld is feasible. In addition, deformation is uniform throughout the weldment, which results in a significantly higher elongation than that of the 2xxx and 7xxx series alloys [Kaufman and Johnson].

III. EFFECTS OF PROCESSING ON THE FUSION ZONE

A. INTRODUCTION

While the base metal has been studied intrinsically, there are very few studies of the weldment properties on 2090. Because the properties are directly related to the microstructure, an understanding of the fusion zone microstructure is needed to effectively improve the weld properties. The objective of this section is to develop a mechanistic understanding of 2090 weldment mechanical properties through characterization of the fusion zone microstructure. Specific emphasis is placed on characterizing the precipitation development and distribution in the EB and GTA fusion zones.

B. BACKGROUND

The two welding processes chosen for this study are electron beam (EB) and gas tungsten arc (GTA) welding. EB welding is a high energy density process with a low heat input, while GTA welding is a low energy density process with higher heat input. The heat input (H_{net}) required to produce a full penetration weld on 3.2 mm sheet using EB and GTA welding differs by one order of magnitude, 43 J/mm and 310 J/mm, respectively. Using simplified two-dimensional flow equations [AWS Welding Handbook] for thin plate,

$$S_t = L\, H_{net} / 2\pi k\rho C\, (T_m - T_o)^2 \quad \text{and} \quad R = 2\pi k\rho C\, (t / H_{net})^2\, (T_c - T_o)^3$$

S_t = solidification time, s
R = cooling rate, °C/s
L = heat of fusion, (1.028 J/mm^3)
k = thermal conductivity, (0.120 J/s mm K)
ρ = density, (2.6×10^{-3} g/mm^3)
C = specific heat, (1.25 J/g K)

the estimated solidification and cooling rates for EB welding are 0.05s and 3200°C/s, respectively, and for GTA welding are 0.33s and 62°C/s, respectively. The difference in constitutional undercooling of EB and GTA welding will affect the dendrite formation and the solute distribution in the fusion zone and in turn the weld properties.

C. EXPERIMENTAL PROCEDURES

The as-received base metal sheet was thermomechanically processed to a T3 condition: cold rolled, solution heat treated, and stretched 4.6%. From the as-received sheet, the weld coupons were cut to 100 mm x 200 mm dimensions and then processing oxides and distortion were machined off, reducing the final thickness from 4.3 mm to 3.2 mm.

The weld coupons were chemically cleaned with 5 vol-% sodium hydroxide in water for one minute, followed by a concentrated nitric acid rinse. Autogenous (no filler addition), bead-on-plate welds were produced transverse to the rolling direction. The welding parameters used for EB and GTA welding are listed in Table III.1. For both

processes, travel speeds that are slightly faster than the typical speeds were used to minimize distortion, the heat affected zone size, and hot cracking. For GTA welding, direct current straight polarity and continuous current were used. A 2.4 mm diameter electrode with tip angled 90°-120° was used to produce a narrow weld width. Shielding gas of 75% He-25% Ar with the flow rate of 12 L/min was utilized. GTA welding was performed in an inert atmosphere on a water-cooled chill block. EB welding was performed in vacuum, $4x10^{-4}$ torr. (These precautions, mechanical and chemical cleaning, fast travel speeds, welding in an inert atmosphere, and use of a water-cooled chill block, were taken to prevent porosity and hot cracking.)

The base metal and weldments were artificially aged at 160°C, 190°C, and 230°C to the peak-strength (designated as T8). The optimum temperatures for solution heat treatment (SHT) were determined using differential scanning calorimetry. The solutionized and aged process consists of a three-step heat treatment: 535°C for 15min, 550°C for 15min, water quench, and subsequent aging at 160°C.

After the heat treatment, both the base metal and the weldments were machined into tensile specimens. For the weldments, the reinforcement was machined off, reducing the final thickness of the composite tensile specimens to 2.54 mm. Figure III.1 shows the tensile specimen configurations. The tensile tests were conducted at 293 K and 77 K, but only the specimens aged at 160°C were tested at 77 K.

Transmission electron microscopy (TEM) specimens were made from the base metal in the following conditions: 160°C for 32 hours, 230°C for 16 hours, and solutionized and aged at 160°C for 16 hours, and from the EB and GTA fusion zones: as-welded, 160°C for 1, 8, 16, and 32 hours, 230°C for 16 hours, and solutionized and aged at 160°C for 16 hours. The foils were prepared from disks by mechanically polishing to 0.125 mm thickness and then jet-polishing using a potential of 20V in a 20% nital solution cooled to 243 K. The foils were viewed at 100 KV using a Philips EM 301. All of the centered dark field images were taken using a two-beam condition on a [110] zone axis. Energy dispersive x-ray spectroscopy (EDS) was performed on a scanning electron microscopy, Philips EM 400, to analyze the intermetallics composition.

Table III.1 Parameters used for gas tungsten arc welding and electron beam welding.

	GTAW	EBW
Current:	110 A	9.5 mA
Voltage:	18-20 V	80 kV
Travel speed:	6.4 mm/s	16.9 mm/s
Electrode diameter:	2.4 mm	-
Electrode angle:	90-120 deg	-
Electrode to work distance:	1.6 mm	280 mm
Shielding gas:	75% He-25% Ar	
Vacuum pressure:		$2x10^{-4}$ Torr

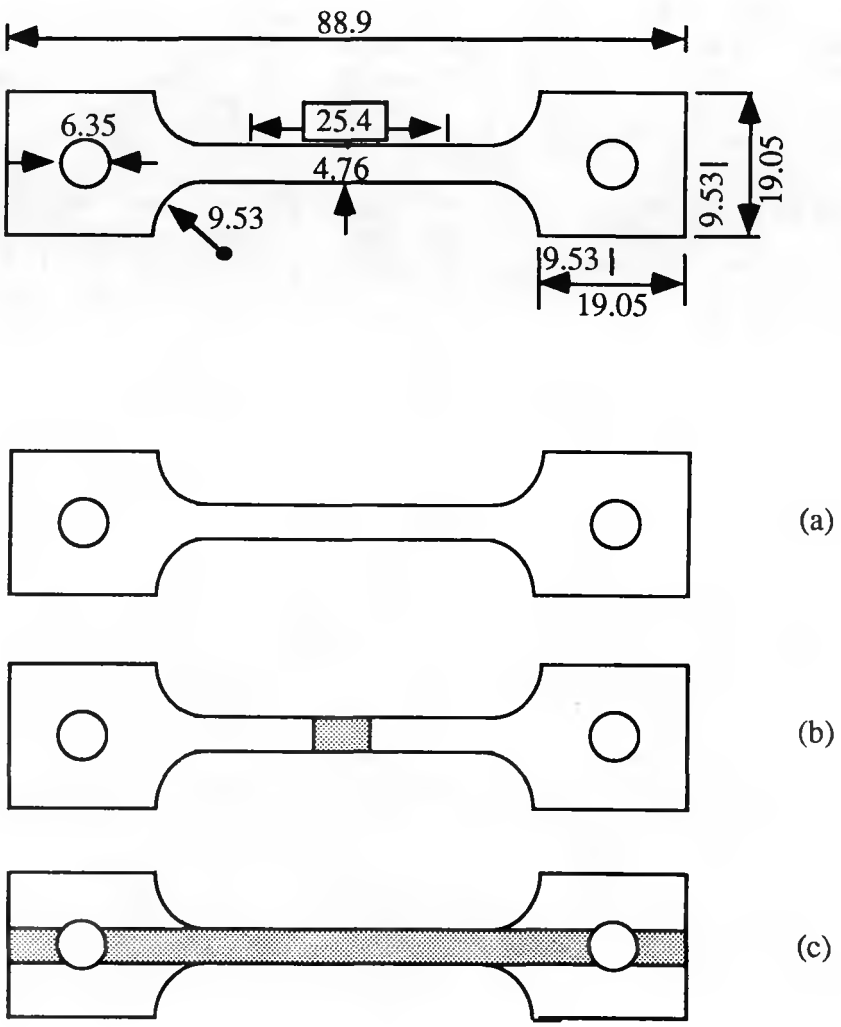

Figure III.1: Tensile specimen configurations: a) base metal, b) composite weld, c) all-weld metal. Dimensions are in mm, and the shaded regions represent the fusion zone.

D. RESULTS

D.1 Microstructure

Figure III.2 shows the composite optical micrographs of the base metal, EB and GTA fusion zones. Due to the type of thermomechanical processing the 2090 has undergone, the microstructure contains highly elongated and "pancake-like" grains with short dimension in the short-transverse direction. The grain size is difficult to measure. In the weldments, the EB fusion zone consists of fine equiaxed dendrites and their average size is approximately 10 μm. The average cellular dendrite and grain sizes of the GTA fusion zone are approximately 20 μm and 150 μm, respectively. The dendrite size was determined by averaging both length and width of the dendrites. The EB and GTA fusion zone widths are 3.2 mm and 6.4 mm, respectively.

D.2 Chemical and Energy Dispersive X-ray Analysis

The results of atomic absorption spectroscopy indicate that the composition of autogenous GTA welds was similar to that of the base metal, 2.8Cu-2.2Li-0.12Zr-Al. There was no Li loss; instead, a slight Cu loss was found which is attributed to scatter in the data.

Although the overall change in the weld composition was insignificant, the differences in solute segregation was expected between the EB and GTA fusion zones due to the different cooling rates. Copper segregation was studied qualitatively using energy dispersive x-ray (EDX) line scans conducted across the dendrites of the as-welded EB and GTA fusion zones.

Figure III.3 shows the concentration profiles of Al and Cu in the EB fusion zone. Different sensitivity scales were used for Al and Cu due to the large difference in concentration. The Cu scale was an order of magnitude larger than the Al scale. The Al concentration profile showed Al depleted regions near the dendrite boundaries and at the intermetallics. The Cu concentration profile of the same line showed peaks near the boundaries but not at the intermetallics. These changes in Al and Cu concentrations were small in the EB fusion zone.

More pronounced Cu segregation was found in the GTA fusion zone than in the EB fusion zone. Zr was also analyzed since the Al depleted regions were present at the intermetallics without the corresponding Cu peaks. Figure III.4a shows the concentration profiles of Al and Cu using the same sensitivity scales as in Figure III.3. The Al valleysand Cu peaks are better defined in the GTA fusion zone, but the general trend is similar to that in the EB fusion zone, with Al valleys corresponding to Cu peaks at the dendrite boundaries. Figure III.4b shows the concentration profiles of Al and Zr within the same region. The Al concentration profile is the same as in Figure III.4a. The Zr concentration profile showed small fluctuations along the dendrite, matching Al depleted regions. The line scan displayed a strong presence of a Zr-containing phase at the dendrite boundary. The difference in Cu homogeneity is expected to affect the precipitation behavior (i.e., size, volume fraction, and distribution) in the fusion zone.

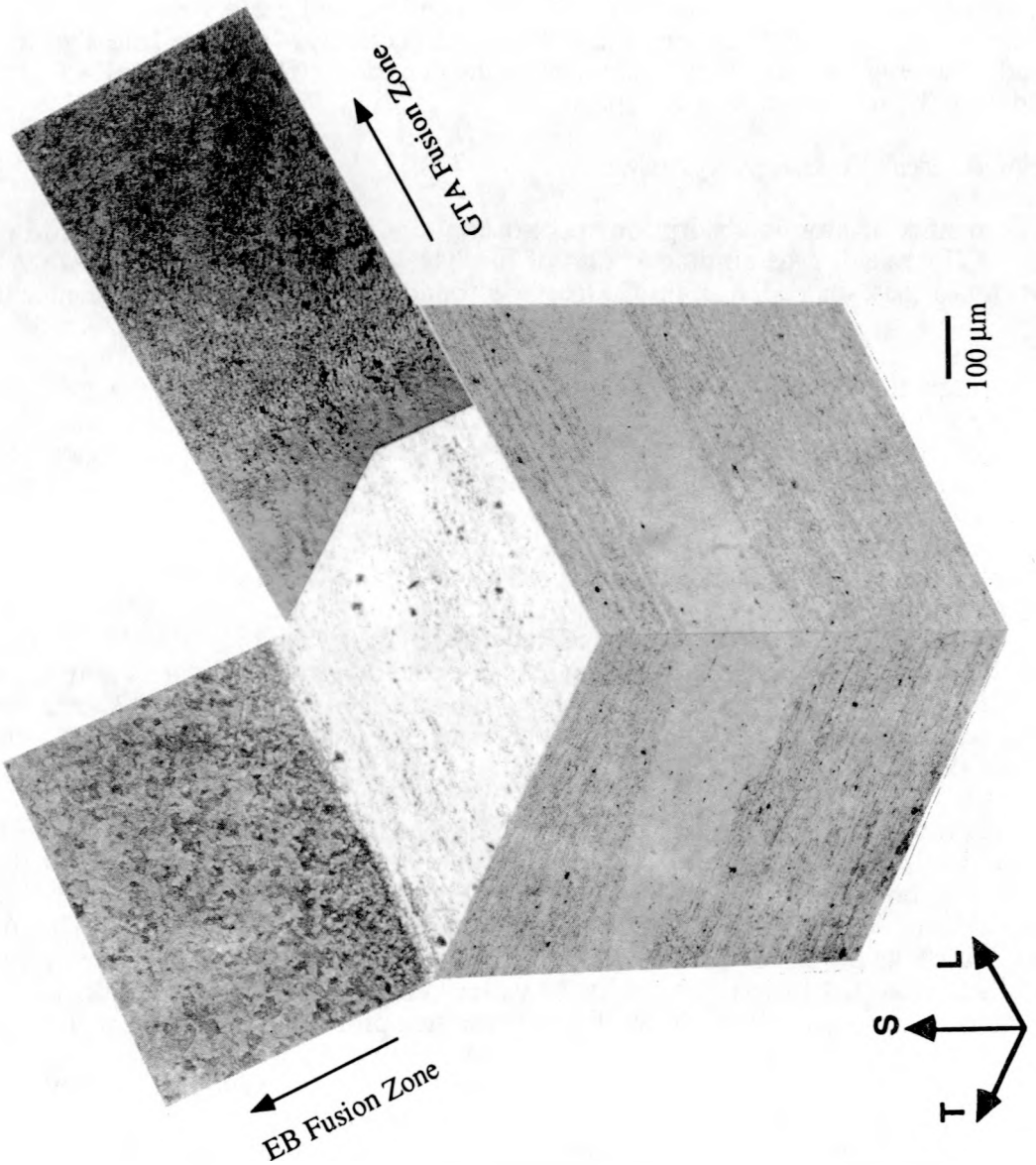

Figure III.2: Composite optical micrographs showing the grain structures of 2090, and EB and GTA fusion zones. (XBB903-2648)

D.3 Transmission Electron Microscopy

D.3.1 The Base Metal

Transmission electron microscopy (TEM) of 2090 in the T8 condition reveals the homogeneity and high volume fraction of the strengthening phases. Figure III.5 shows the centered dark field (CDF) images of δ' and T_1 precipitates in peak-aged base metal. the images were taken using the superlattice reflection and two edge-on variants of T_1, respectively. As observed in other studies [Rioja et.al.,1986; Gregson and Flower, 1987; Tosten et.al. 1988], the δ' CDF image displays three different δ' morphologies: small discrete spherical particles of δ', δ' that has encapsulated the β', and δ' that has coated the coherent, broad faces of the θ' phase. In addition, a distinct δ' and θ' precipitate free zone (PFZ) exists adjacent to the grain boundary due to the Li depletion resulting from the concurrent presence of the equilibrium phases up to and at the grain boundary. On the other hand, the T_1 CDF images show T_1 uniformly distributed throughout the matrix as well as heterogeneously outlining the subgrain boundary.

The selected area diffraction (SAD) pattern of an overaged base metal in Figure III. 6 shows no superlattice reflection and only faint T_1 reflections and streaks. The corresponding bright field (BF) image of T_1 reveals less densely distributed T_1 in the matrix. In the solutionized and aged condition, the 2090 lacked T_1 phase in the matrix. Figure III.7 shows a bright field (BF) and δ' CDF pair of a base metal specimen solutionized and aged for 16 hours at 160°C. The micrographs reveal mostly homogeneous δ' and some β' that has been encapsulated by δ'. Unlike the T8 tempered condition, T_1 precipitates are only found at the boundaries, and not in the matrix.

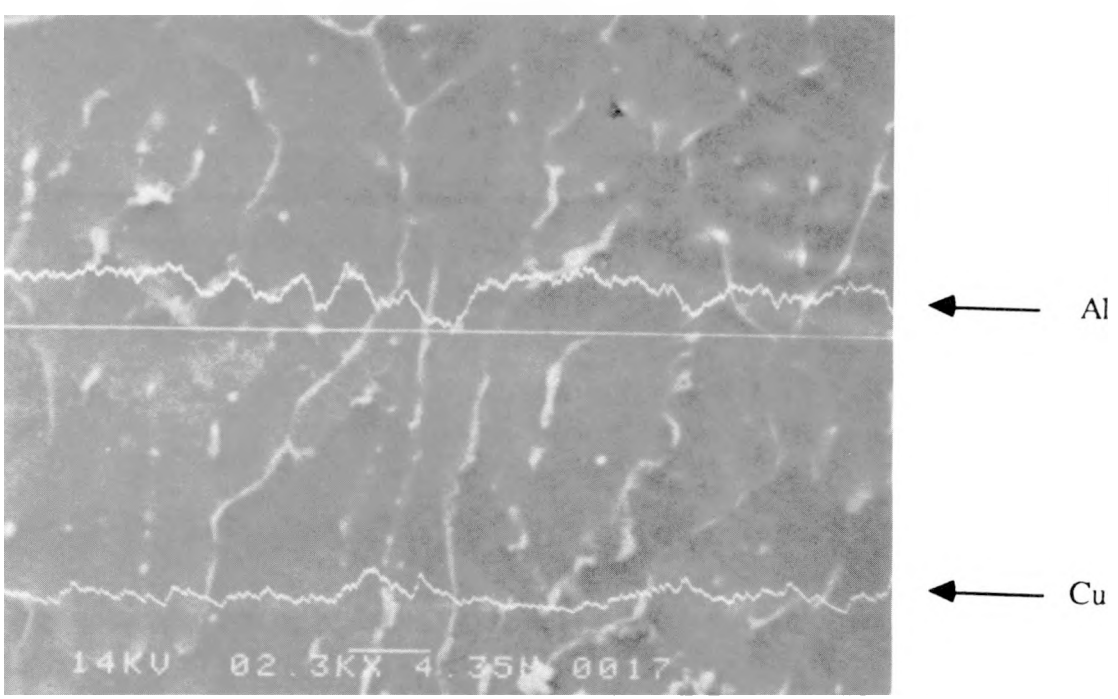

Figure III.3: EDX line scan of EB fusion zone showing the concentration profiles of Al and Cu. (XBB883-2257)

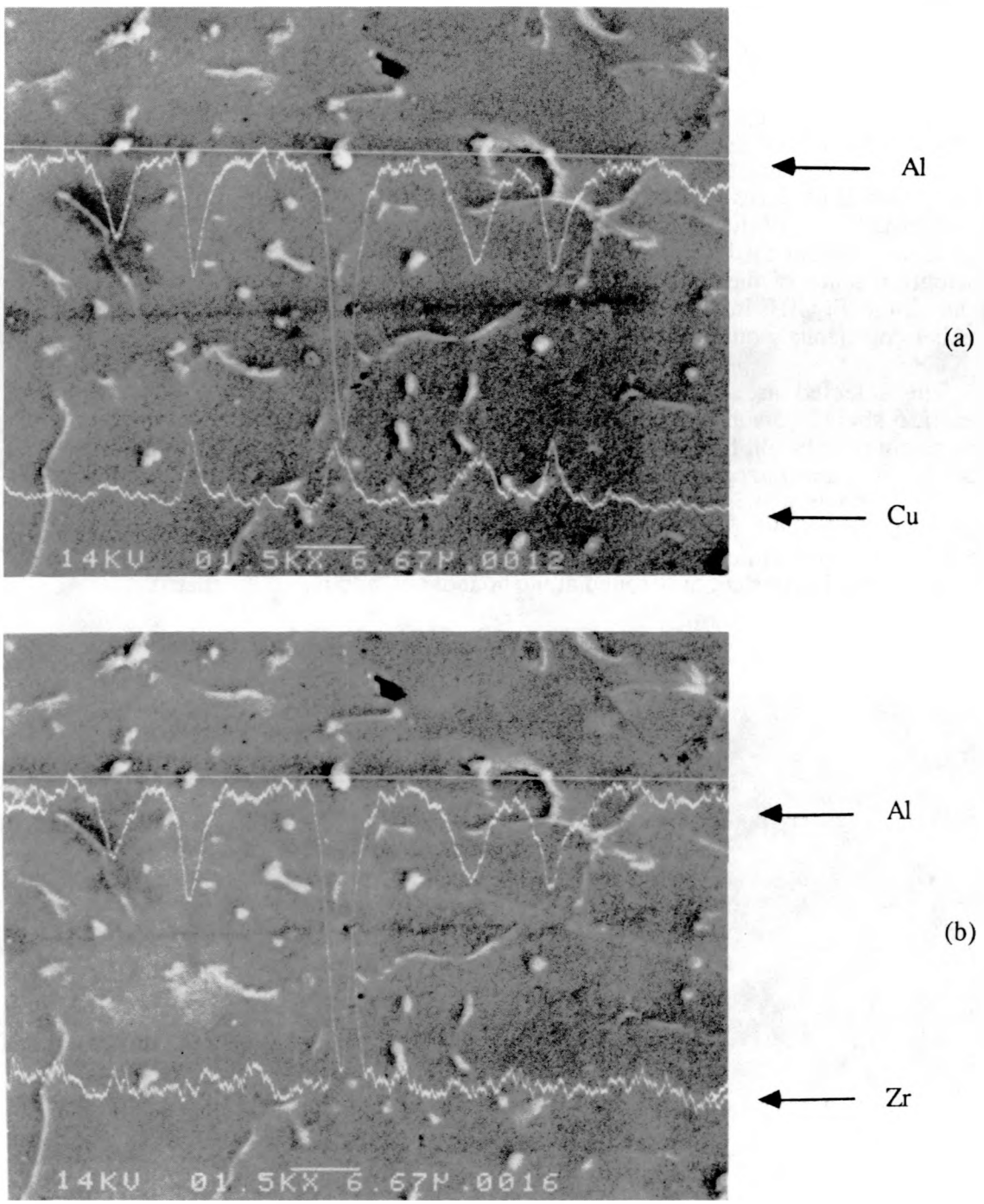

Figure III.4: EDX line scan of GTA fusion zone: a) concentration profiles of Al and Cu, b) concentration profiles of Al and Zr. (XBB883-2252)

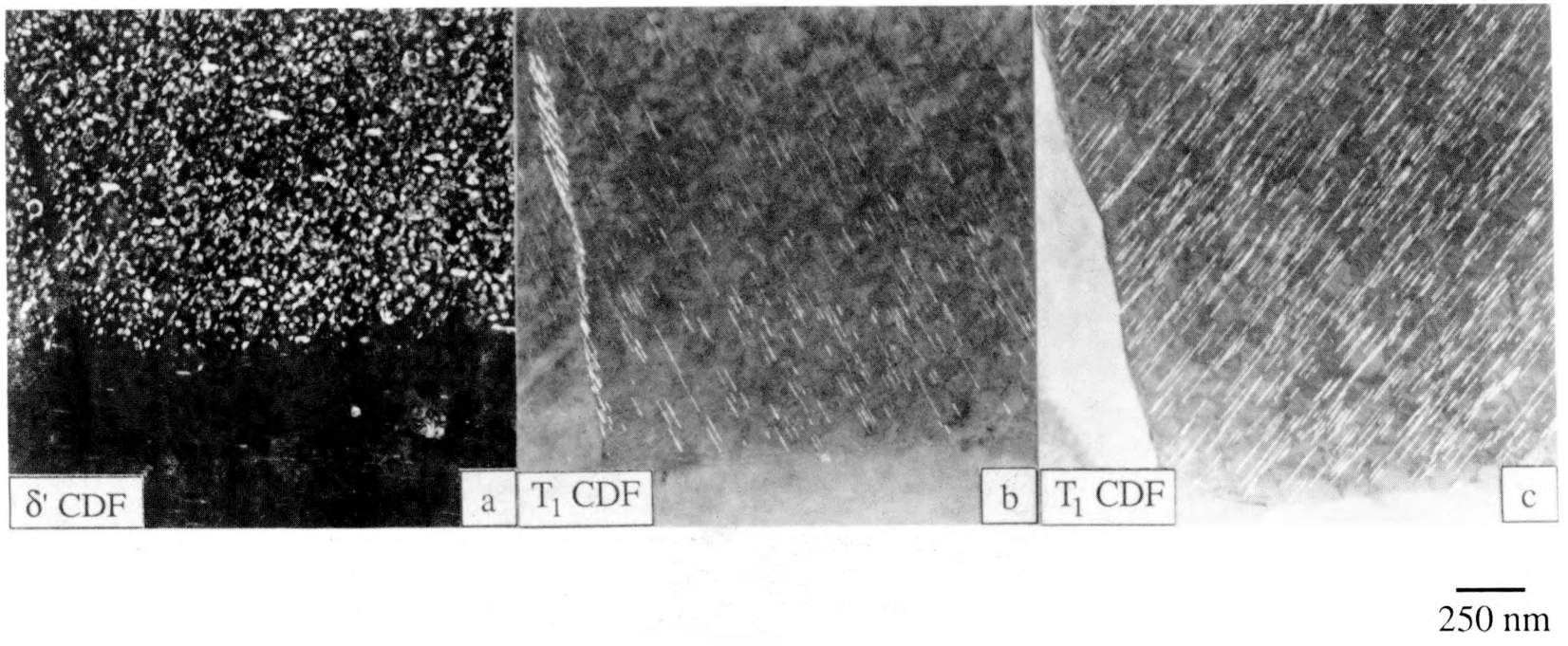

Figure III.5: TEM micrographs of 2090-T8: a) δ' CDF showing three different morphologies of δ' and precipitate free zone adjacent to the grain boundary, b) and c) T_1 CDF displaying homogeneous distribution of T_1 in the matrix and outlining the subgrain boundary. (XBB897-5786A)

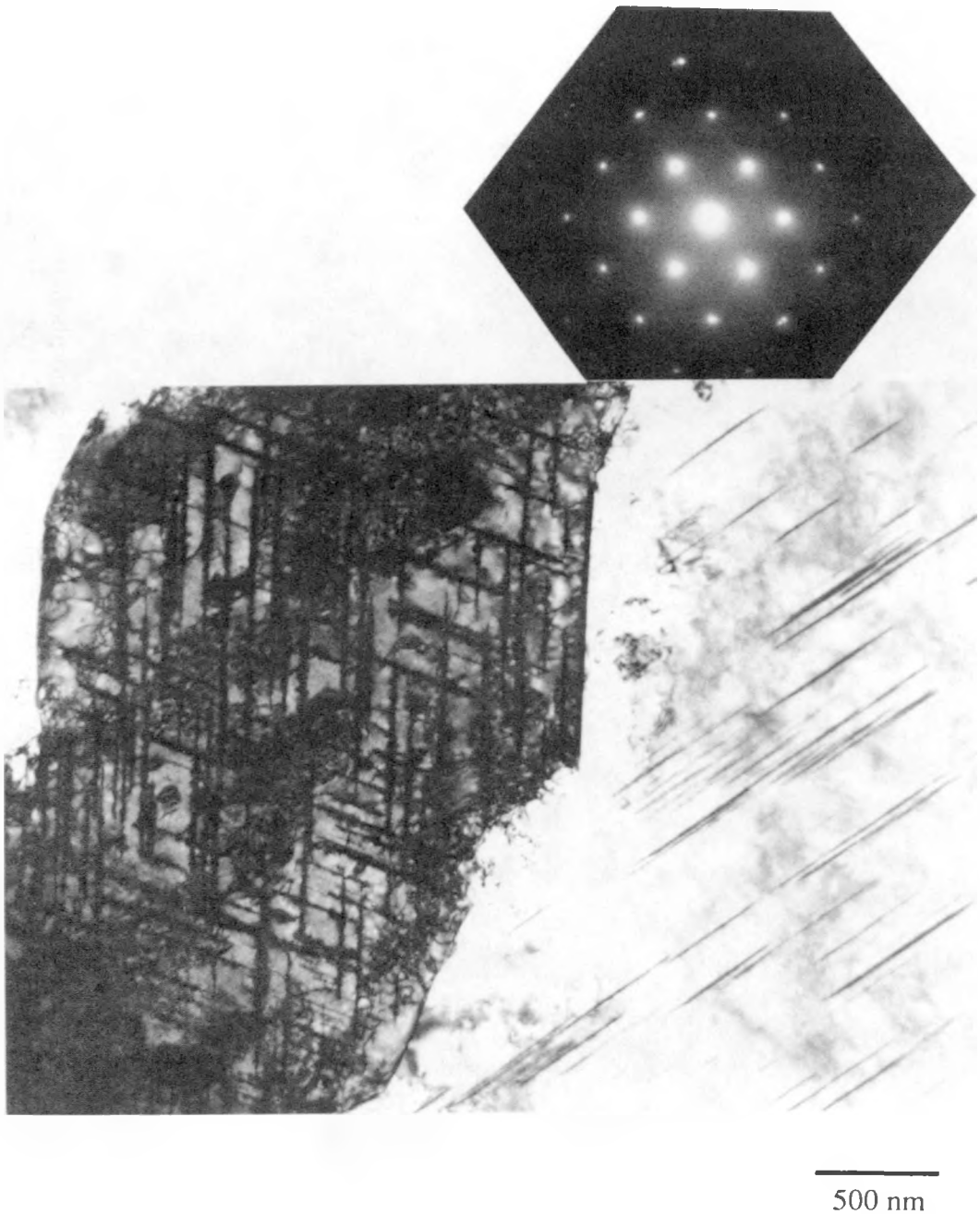

Figure III. 6: TEM micrograph of over-aged 2090. The SAD pattern of [110] zone axis reveals only the subtle T_1 streaks and reflections and the bright field image shows mostly of T_1 in the matrix. (XBB903-269)

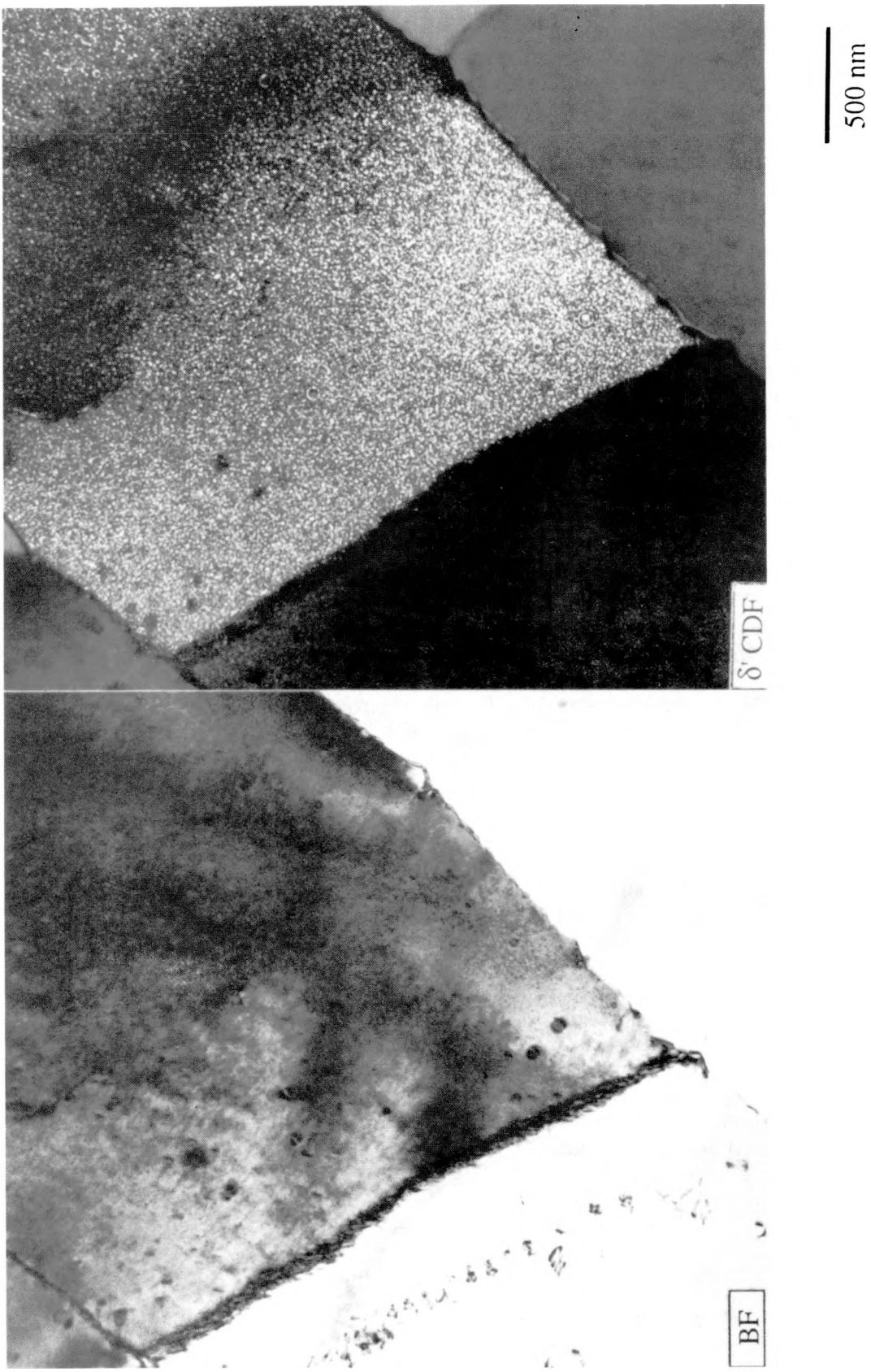

Figure III.7: TEM bright field and δ' CDF pair of 2090 solutionized and aged for 16 hours at 160°C. (XBB903-2692)

D.3.2 The Fusion Zone

D.3.2.1 Aging Response of the Fusion Zone

The effect of aging on precipitation in the fusion zone is apparent from the evolution of selected area diffraction (SAD) patterns. Figure III.8 shows the SAD patterns of a <110> zone axis in the GTA fusion zones at minimum aging time from one hour aged to an over-aged condition. Figure III.7f is a schematic illustration of the [011] zone axis containing the superlattice reflections of the δ' and β' precipitates, the <100> streaks from the θ' precipitates, the <111> streaks and the reflections at 1/3 {113} from thin T_1 precipitates [Huang and Ardell, 1987].

The superlattice reflections are faint after aging for only one hour. As the aging time increases, the superlattice reflections become more prominent indicating the coarsening of δ'. After aging for 16 hours, the θ' streaks in the <100> direction are observed with subtle T_1 streaks in the <111> directions. In the peak-aged condition, the SAD pattern is similar to the schematic illustration with discrete superlattice reflections, θ' streaks, and T_1 streaks and reflections. In the overaged condition, the superlattice reflections, and the θ' and T_1 streaks have disappeared and only the T_1 reflections are present.

D.3.2.2 The Under-Aged Microstructure

With post-weld aging, an inhomogeneous distribution of Cu and Li results in a nonuniform distribution of precipitates in the fusion zone. Figure III.9 shows a δ' CDF image from an EB fusion zone aged for one hour. The micrograph reveals three undesirable features: a nonuniform distribution of δ' in the matrix, the formation of intermetallics at the boundaries and also at the triple points, and a continuous film between the intermetallics. The globular intermetallics seen at the dendrite boundaries have been documented as the T_2 phase [Bartage, 1987], while the round intermetallic is unknown at this time. Figure III.10 shows the CDF images of δ' in the 8 hour aged EB and GTA fusion zones. The EB matrix still has inhomogeneous distribution of δ', while the GTA matrix has a more uniform distribution of δ'.

After aging for 16 hours, θ' and T_1 start to appear adjacent to the boundary and in the vicinity of other intermetallics, forming a θ' precipitate localized zone (PLZ). The bright field (BF) and CDF images of δ' in the EB fusion zone is shown in Figure III.11. Only the EB welds have significant concentrations of θ' within 250 nm of the dendrite boundary with the T_1 sparsely distributed within the region: the fine streaks are caused by an edge-on variant of θ' precipitates. The micrographs also reveal an edge-on view of T_1 (Figure III.11a) and T_2 (as indicated in Figure III.11b) at the boundaries. The presence of T_1 at the boundary has a little effect on the distribution of δ', whereas the T_2 at the boundary is associated with a narrow δ' precipitate free zone. The localization of θ' is also observed in the vicinity of the intermetallics, as shown in the BF and δ' CDF pair of the GTA fusion zone aged for 16 hours in Figure III.12. The combination of a solute concentration gradient and strain field around these intermetallics appears to promote preferential nucleation of the precipitates.

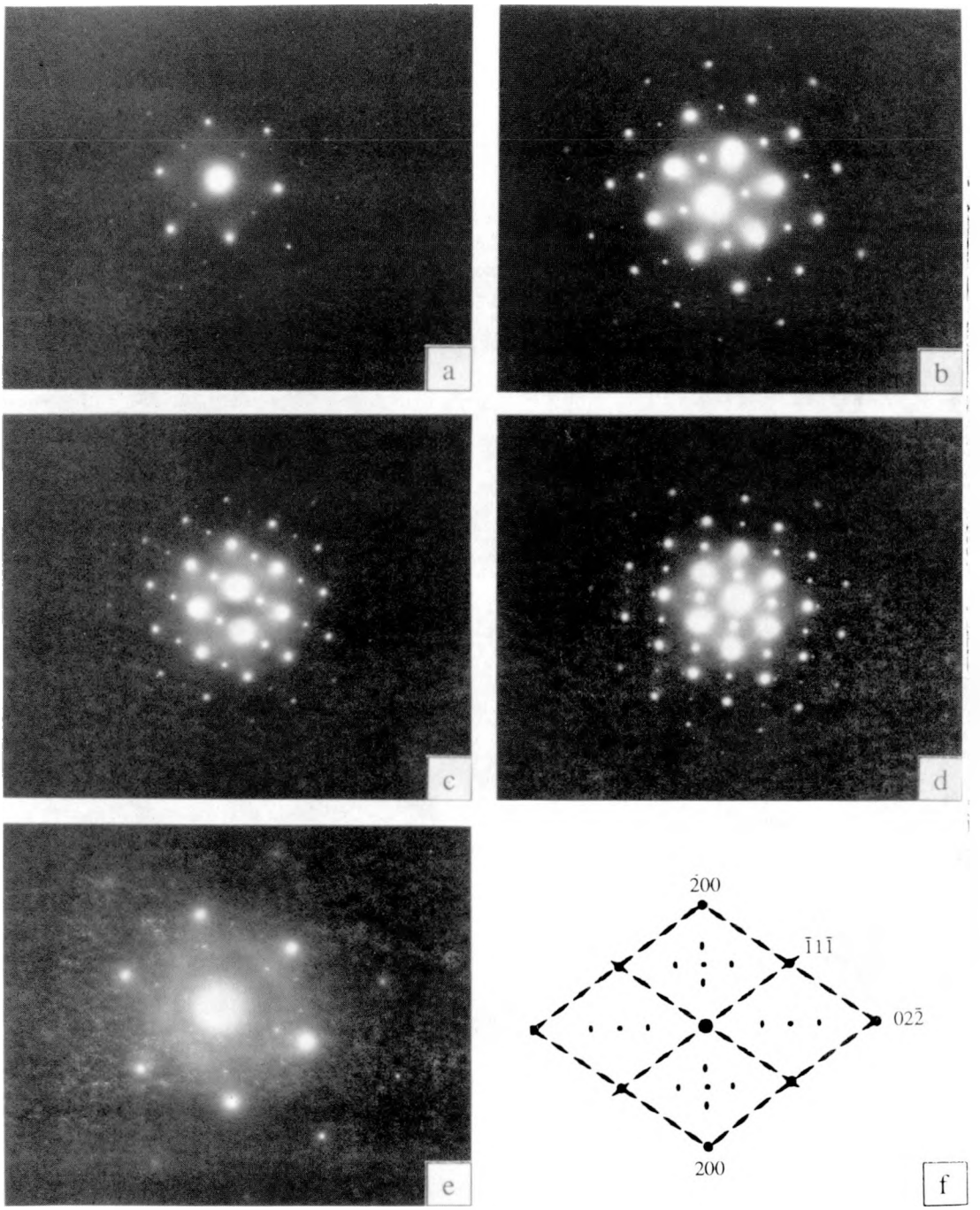

Figure III.8: TEM SAD patterns of <110> zone axis from GTA fusion zone in the post-weld aged conditions: a) one hour, b) 8 hours, c) 16 hours, d) 32 hours at 433 K representing the peak-aged condition, e) 16 hours at 503 K representing the over-aged condition, f) an idealized illustration of [011] zone axis. (XBB890-10203)

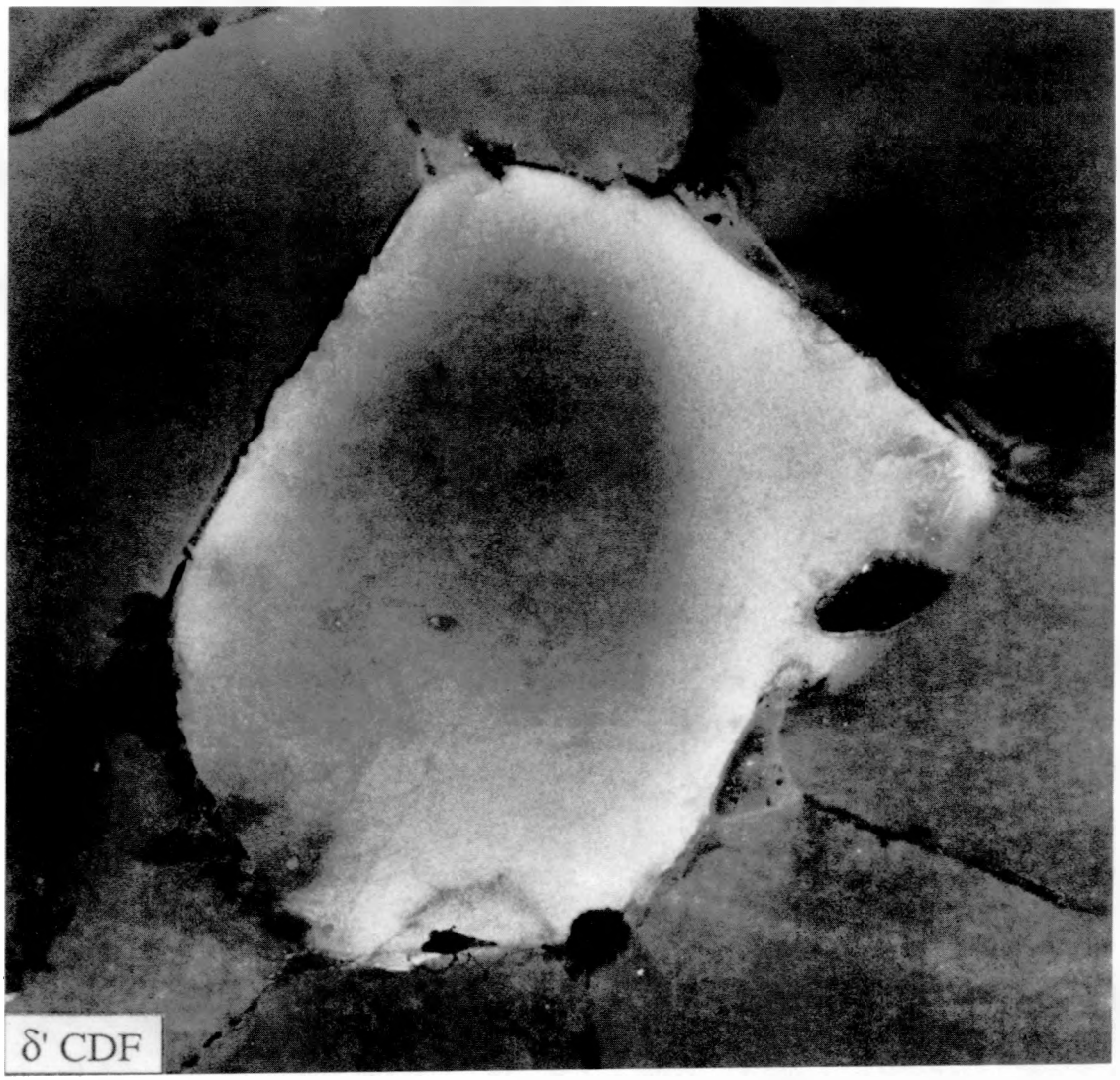

Figure III.9: TEM micrograph of EB fusion zone aged for one hour at 433 K. A δ' CDF image reveals a nonuniform distribution of δ' in the matrix, and the formation of intermetallics and continuous film at the boundaries. (XBB890-10210)

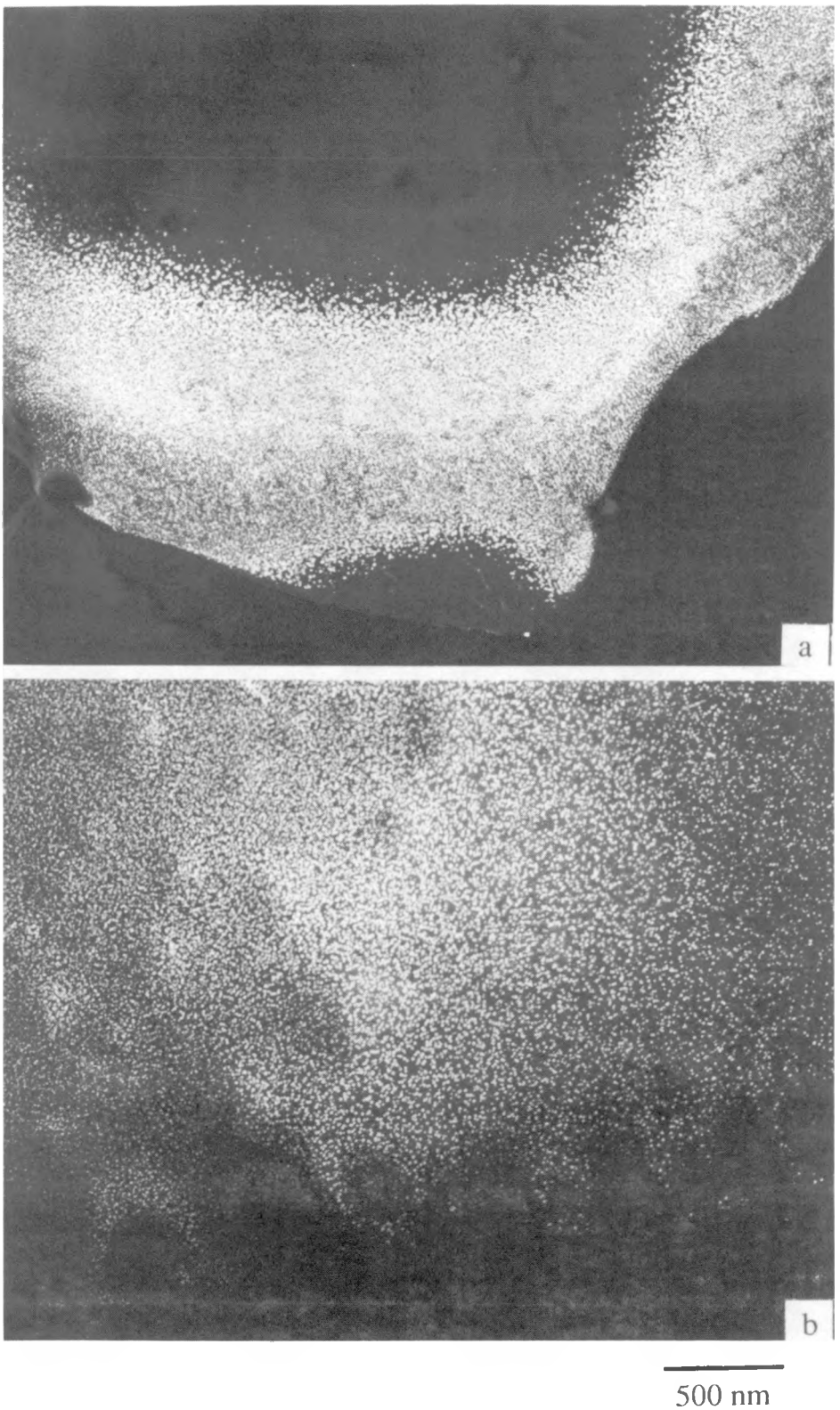

Figure III.10: TEM δ' CDF images of: a) electron beam, b) gas tungsten arc fusion zones aged for 8 hours at 433 K. (XBB890-10202A)

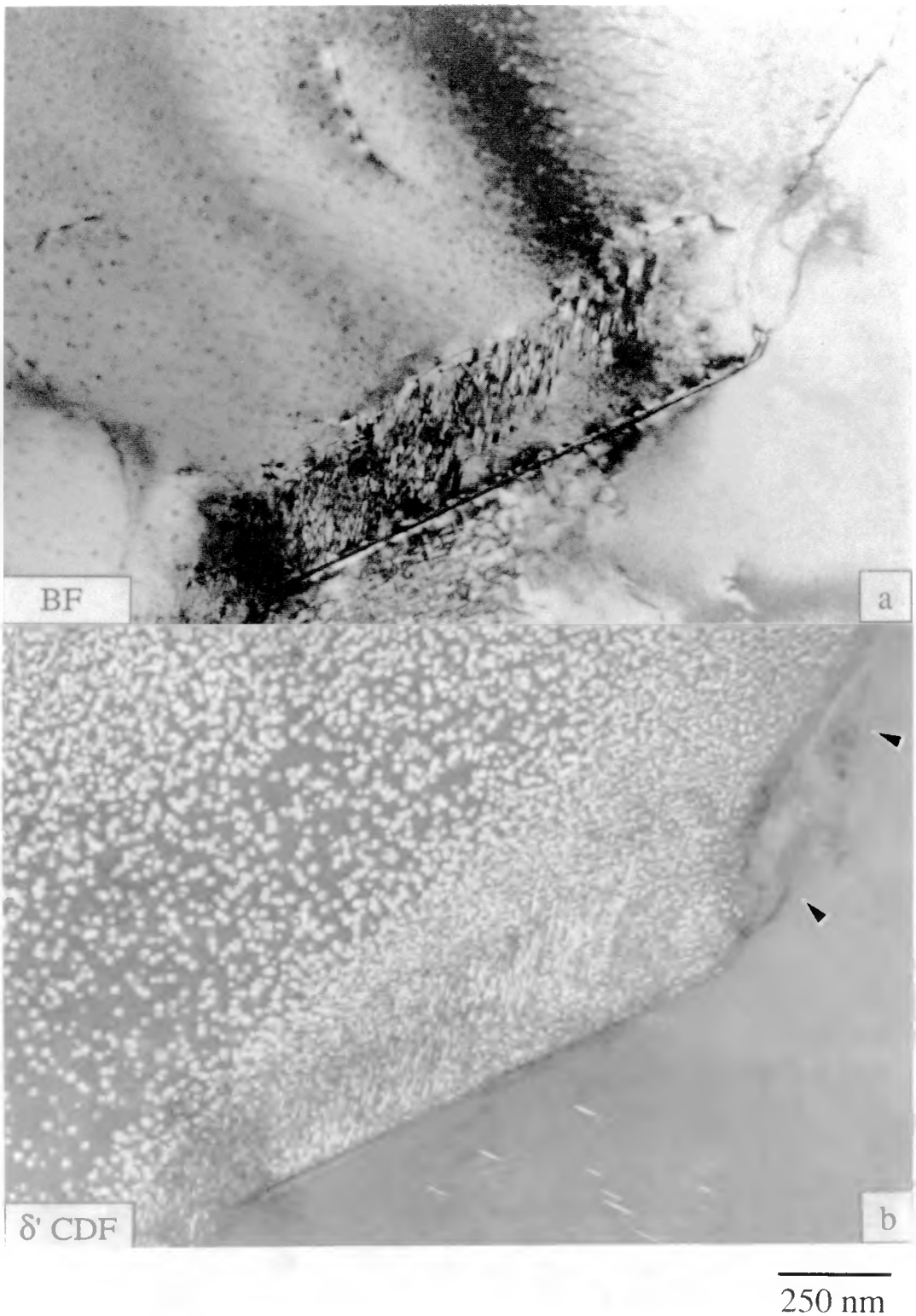

Figure III.11 TEM bright field and δ' CDF pair of EB fusion zone aged for 16 hours at 433 K showing the θ' localization at the boundary with the presence of T_1 and T_2 on the boundaries. The T_2 precipitate is as indicated in b). (XBB890-10208)

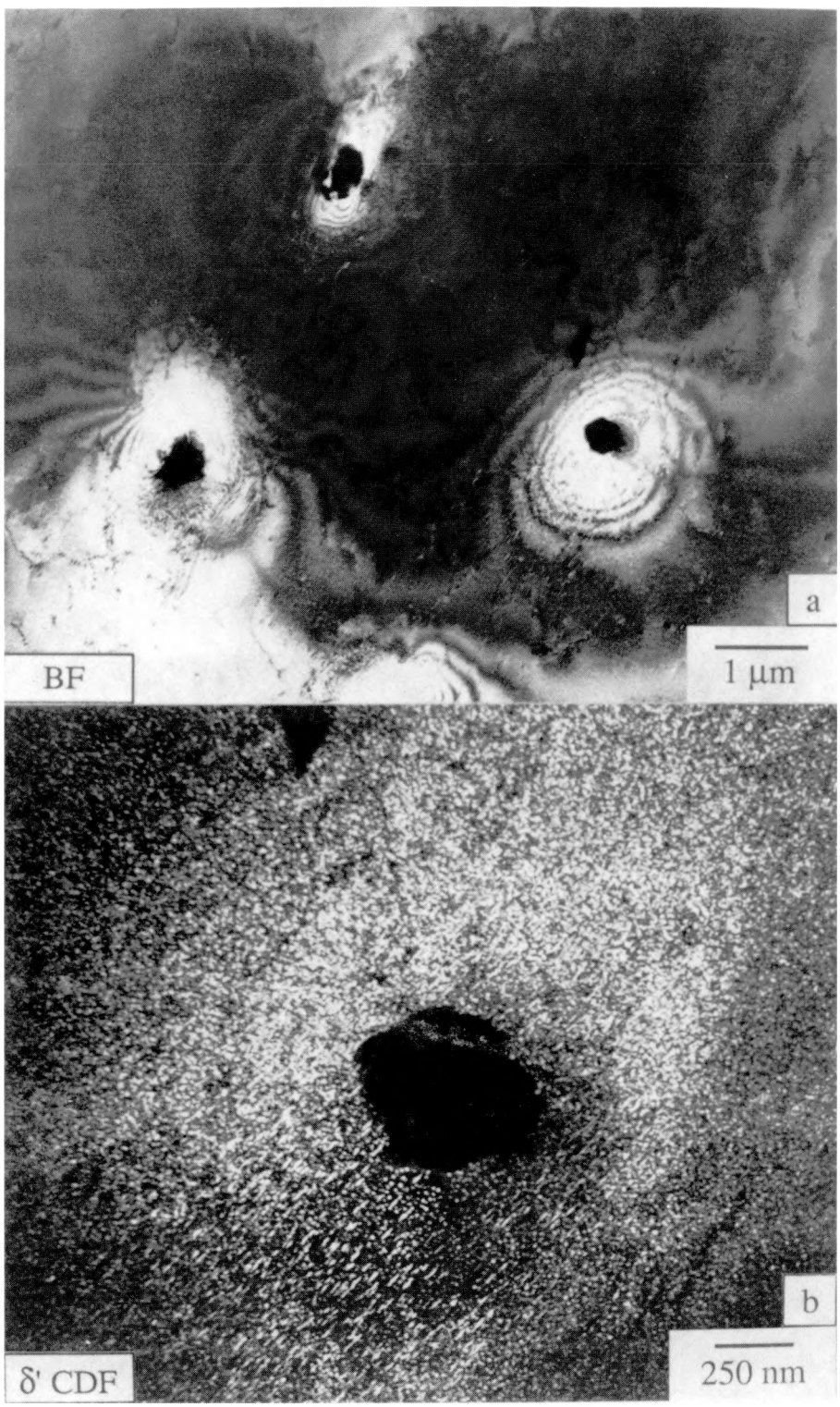

Figure III.12: TEM bright field and δ' CDF pair of GTA fusion zone aged for 16 hours at 433 K showing the localization of θ' at the vicinity of intermetallics. (XBB890-10212)

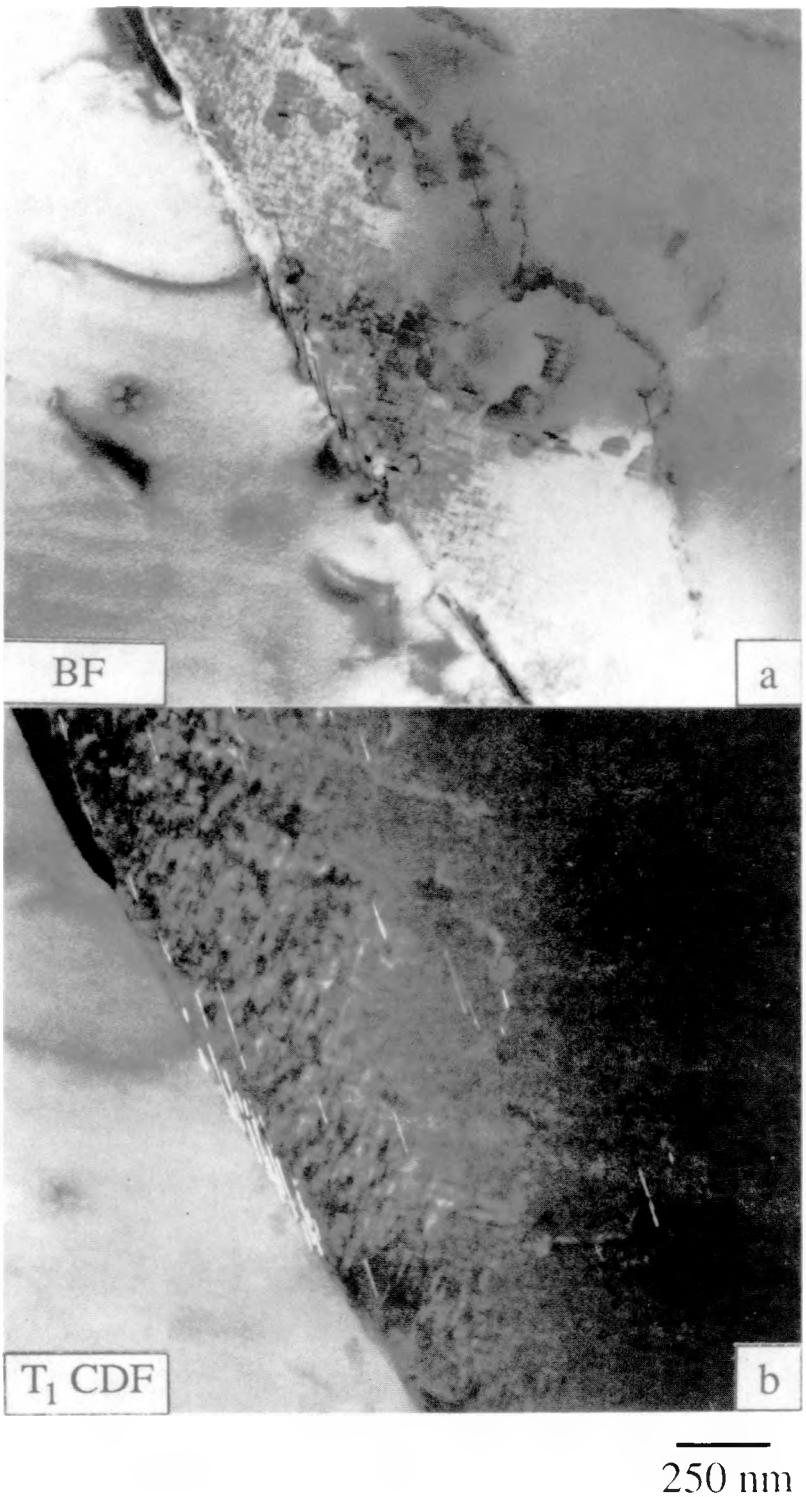

Figure III.13: TEM BF and T_1 CDF pair of peak-aged EB fusion zone. The micrographs show localization of θ' with T_1 sparsely distributed adjacent to and on the boundary. (XBB890-10207)

D.3.2.3 The Peak-Aged Microstructure

Continued aging did not change the distribution of θ' in the peak-aged EB fusion zones. The PLZ size remained about 250 nm. Figure III.13 shows the PLZ in the BF image and T_1 on the boundary and within the matrix in the T_1 CDF image of the EB fusion zone. Even at the dendrite boundary, the formation of T_1 is not continuous. Figure III.14 shows a BF, a δ' CDF, and two edge-on variants of T_1 images from the same area in the peak-aged GTA fusion zone near an intermetallic. The δ' distribution is more uniform throughout the matrix than that of the θ' and T_1. The size of the θ' is much smaller than the T_1 (T_1 is about 120 nm). Although the overall precipitate distribution of the GTA fusion zones is more homogeneous than in the EB fusion zones, the volume fraction of T_1 found in the fusion zone is insignificant compared to that in the base metal.

Chemical analysis using STEM-EDS indicates that the Cu content of the EB matrix is 40% less than that of the base metal matrix. High concentrations of Cu are found in either the intermetallics or the boundary film. The continuous film on the boundary in Figure III.15a consists of, in wt-%, mostly Al with 18% Cu and 5% Cl, while the film on the boundary in Figure III.15b is composed of 66% Al, 33% Cu, and a trace of Fe. The intermetallics within the dendrite contain 37% Cu, 10% Si, 5% Fe, and 3% Cl, remainder being Al. No trace of Zr or low melting point elements such as Na and K were observed in the EB fusion zones.

D.3.2.4 The Over-Aged Microstructure

The over-aged microstructure in the EB and GTA fusion zone is similar to the base metal. At 503 K, the δ' and θ' have dissolved, leaving only the equilibrium phases, T_1 and T_2. However, in comparison to the base metal, the volume fraction of T_1 in the fusion zone is still limited.

D.3.2.5 The Solutionized and Aged Microstructure

Alternative to the overaged condition, the solution heat treatment has dissolved all the strengthening phases and homogenized the solute distribution in the fusion zone. Subsequent aging leads to the growth of δ'. Unlike the other post-weld aged EB specimens with the same aging time, the SAD pattern and its respective δ' CDF image of a solutionized and aged EB specimen in Figure III.16 reveals only the superlattice reflections and shows mostly homogeneous δ' within the matrix and no localization of θ' adjacent to the boundary, respectively.

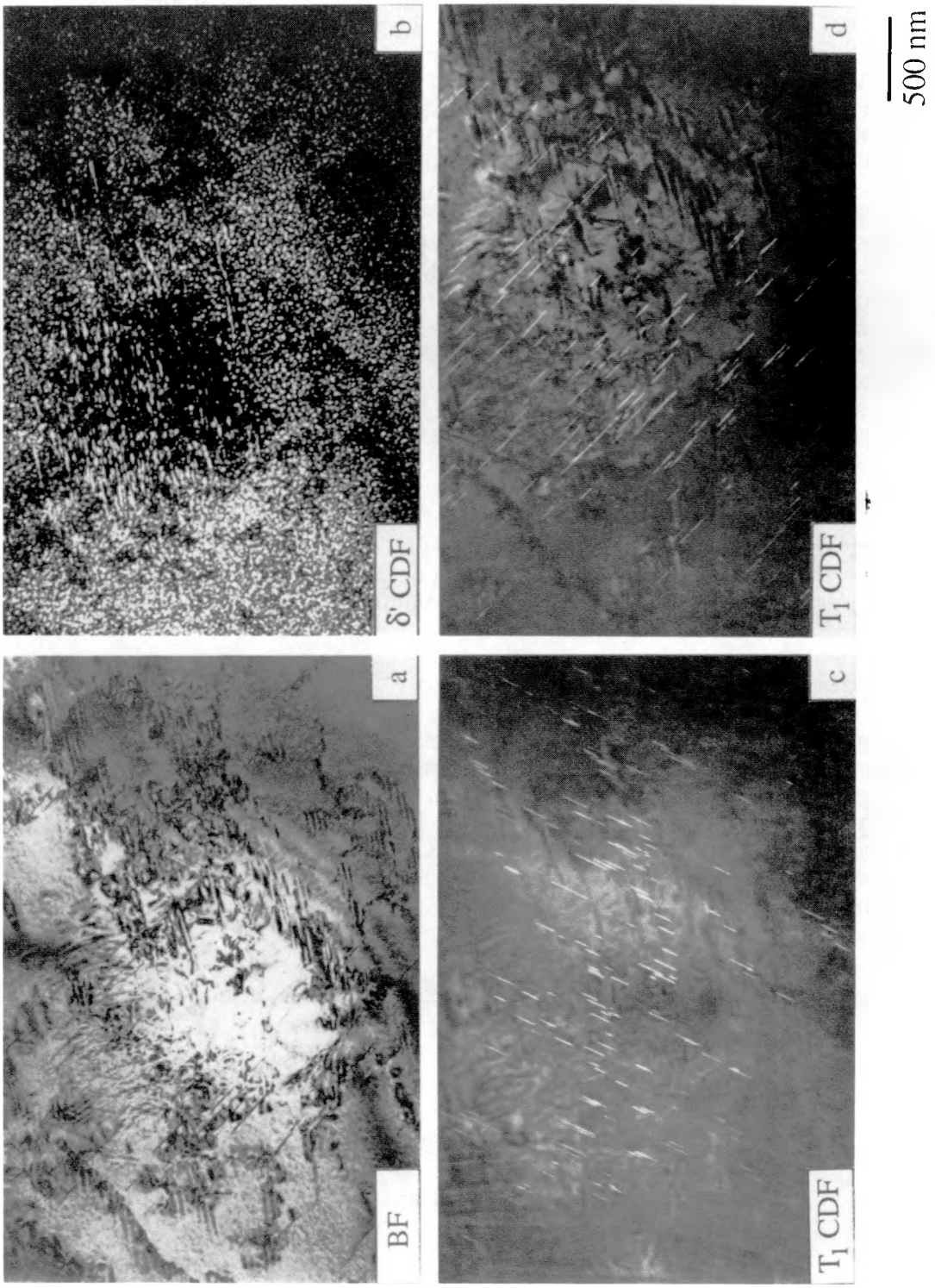

Figure III.14: TEM micrographs from the same region in peak-aged GTA fusion zone near an intermetallic: a) BF, b) δ' CDF, c) and d) T_1 CDF. (XBB890-10213)

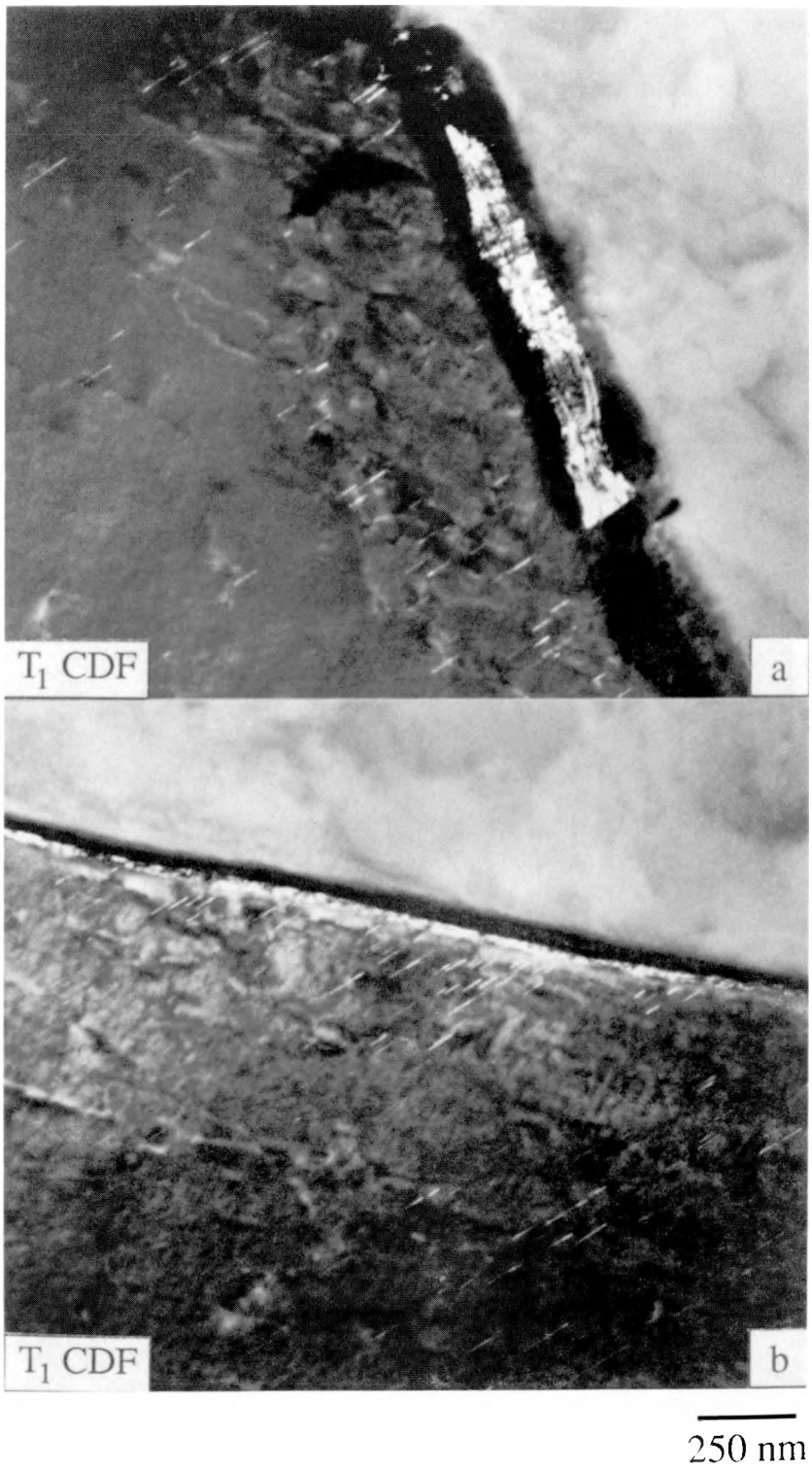

Figure III.15: TEM T_1 CDF images of peak-aged EB fusion zone showing the film formations at the boundaries. (XBB890-10201)

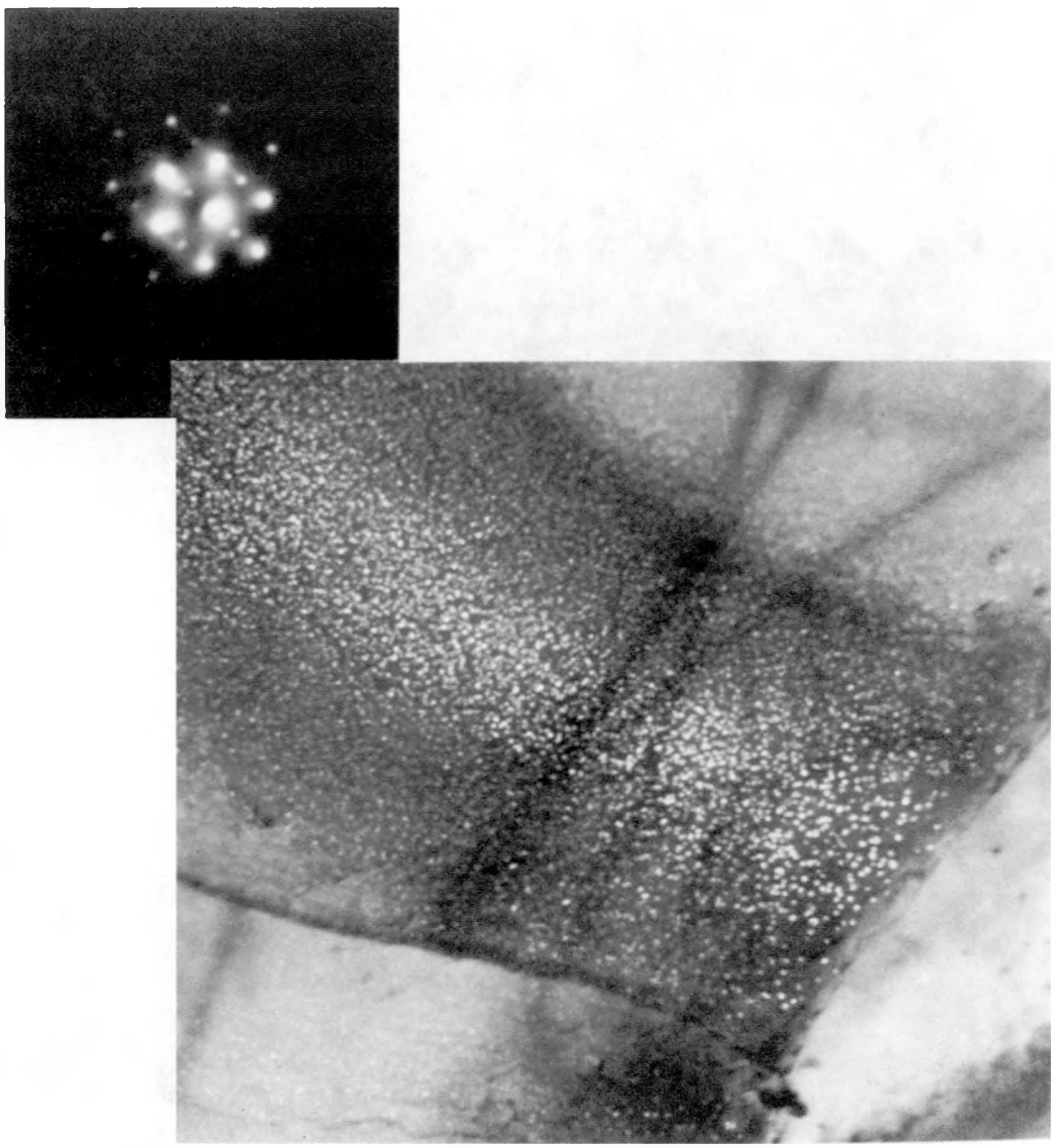

Figure III.16: TEM micrograph of solutionized and aged electron beam fusion zone. The [110] SAD pattern displays only the superlattice reflections and the bright field image shows homogeneous δ'. (XBB903-2690)

D.4 Hardness Profiles of Weldments

The effects of various heat treatments are seen in the Vickers hardness profiles of the EB weldments in Figure III.17. The hardness profiles of the GTA weldments are similar to the hardness profiles of the EB weldments except the size of the fusion zone and heat affected zone is wider. Although the hardness numbers of the as-welded and post-weld aged weldments are different, the overall profiles show similar trend, where they indicate a distinct change in hardness from the fusion zone to the parent metal. The hardness profile of the solutionized and aged weldment, on the other hand, shows more gradual increase in hardness from the fusion zone to the parent metal. The difference in the hardness profiles with post-weld aging will affect the deformation behavior in the weldment.

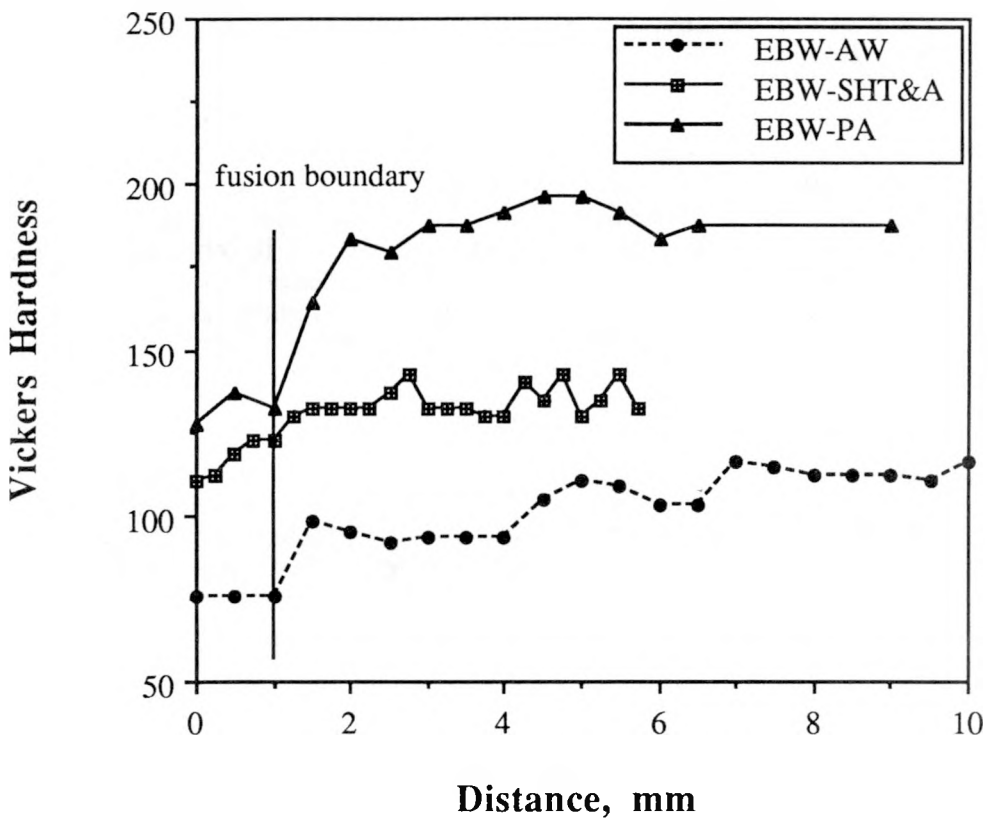

Figure III.17: Vickers hardness profiles of EB weldments from the fusion zone to the unaffected base metal, exhibiting the effects of various base metal heat treatments.

D.5 Tensile Behavior

D.5.1 293 K Tensile Properties

The tensile properties of the base metal, EB and GTA weldments tested at 293 K are presented in Table III.2, and the yield strength and elongation are plotted with respect to the aging temperature and time in Figures III.18. The results of the aging study show that the degradation of 2090 strength occurs at temperatures greater than 200°C. The yield strengths of the specimens aged at 230°C for 16 hours decreased to less than 50% of the 160°C peak-aged condition, and the elongation was the lowest value of all the aged conditions. The best overall strength-elongation combination for 2090 is obtained at lower aging temperature.

The aging response of the EB and GTA weldments was similar to the base metal. As the aging temperature increased, the peak strength was achieved in a shorter time. The highest yield strength of the EB weldment was obtained by aging at 160°C for approximately 32 hours. However, a higher yield strength was achieved for the GTA weldments aged at 190°C than at 160°C. Aging at 230°C also adversely affected both the EB and GTA weldment properties. The joint efficiencies (the ratio of the weldment yield strength to that of the base metal) of the EB and GTA weldments in the near peak-aged condition were 75% and 65%, respectively.

As the weldment strength increased with aging, the weldment elongation decreased precipitously. In the as-welded condition the weldment elongations were greater than 4% and then in the peak-aged condition, the elongations decreased to less than 1%. Visual observation of the tested as-welded EBW and GTAW specimens revealed localized deformation in the fusion zone and a minimal deformation in other areas. In the tested peak-aged weldments, there was no evidence of deformation in the fusion zone. In the overaged condition, the weldment elongation improved slightly. Although the as-welded composite specimens showed only 4% elongation, the all-weld metal GTA weld specimens showed 17% elongation. The all-weld metal specimen displayed similar decrease in elongation to 1.5% in the near peak-aged condition.

After the base metal and composite welded specimens were post weld solutionized, the strengths of the base metal, EB and GTA weldments were the same, particularly with the EB weldments having 18% elongation and failing at the base metal. In the solutionized GTA specimens, the void formations were observed at the fusion boundaries, but they seem to have insignificant effect on the properties since the specimens failed at the center of the fusion zone. Even after aging at 160°C for 4 and 16 hours, the yield strengths of the base metal and the EB weldments continued to be equivalent, but the weldment elongations started to decrease. Similar effect was also observed in the GTA weldments, although the strengths of the GTA weldments were not as high as the the EB weldments. Overall, these solutionized and aged properties are much better than that of the post-weld aged properties.

Table III.2 Tensile properties of electron beam weldments, gas tungsten arc weldments, and base metal tested at 293 K.

Heat Treatment (Ċ/Hours)	EBW/GTAW/BM σ_{YS} (MPa)	EBW/GTAW/BM σ_{UTS} (MPa)	EBW/GTAW/BM Total Elongation (%)
T3; As-welded	195 / 180 /280	290 / 270 / 350	5.5 / 3.5 / 9.5
PWA[2]			
160/8	360 / 255 / 515	405[1]/ 325[1]/ 590	0.5 / 1.0 / 9.0
160/16	- / 295 / 560	- / 315[1]/ 605	- / 1.0 / 9.5
160/32	440 / 315 / 575	445[1]/ 370[1]/ 610	0.5 / 1.0 / 9.5
190/2	320 / - / -	327[1]/ - / -	0.5 / - / -
190/4	355 / 290 / 495	380[1]/ 350[1]/ 540	0.5 / 0.5 / 9.0
190/16	350 / 334 / 496	365[1]/ 370[1]/ 547	0.5 / 0.5 / 11.0
190/24	- / 325 / -	- / 365[1]/ -	- / 0.5 / -
230/2	- / 230 / -	- / 290 / -	- / 1.0 / -
230/4	315 / 260 / 340	355[1]/ 320[1]/ 415	0.5 / 1.0 / 11.0
230/16	275 / 250 / 280	320[1]/ 300[1]/ 370	1.5 / 1.0 / 8.0
SHT & A[3]			
160/0	140 / 150 / 140	308 / 308 / 316	18.0/11.0/16.5
160/4	310 / 315 / 315	415[1]/ 400[1]/ 405[1]	5.5 / 2.5 / 7.0
160/16	415 / 385 / 415	480[1]/ 435[1]/ 485[1]	2.0 / 1.0 / 10.0
All Weld Metal[4]			
As-welded	- / 135 / -	- / 250 / -	- / 17.0 / -
160/32	- / 255 / -	- / 320 / -	- / 1.5 / -

Note: Strengths given to nearest 5 MPa and elongations given to 0.5%.
[1] Fracture strength.
[2] PWA: post weld aged condition.
[3] SHT&A: solution heat treatment and aged condition.
[4] See specimen configuration in Figure III.1.

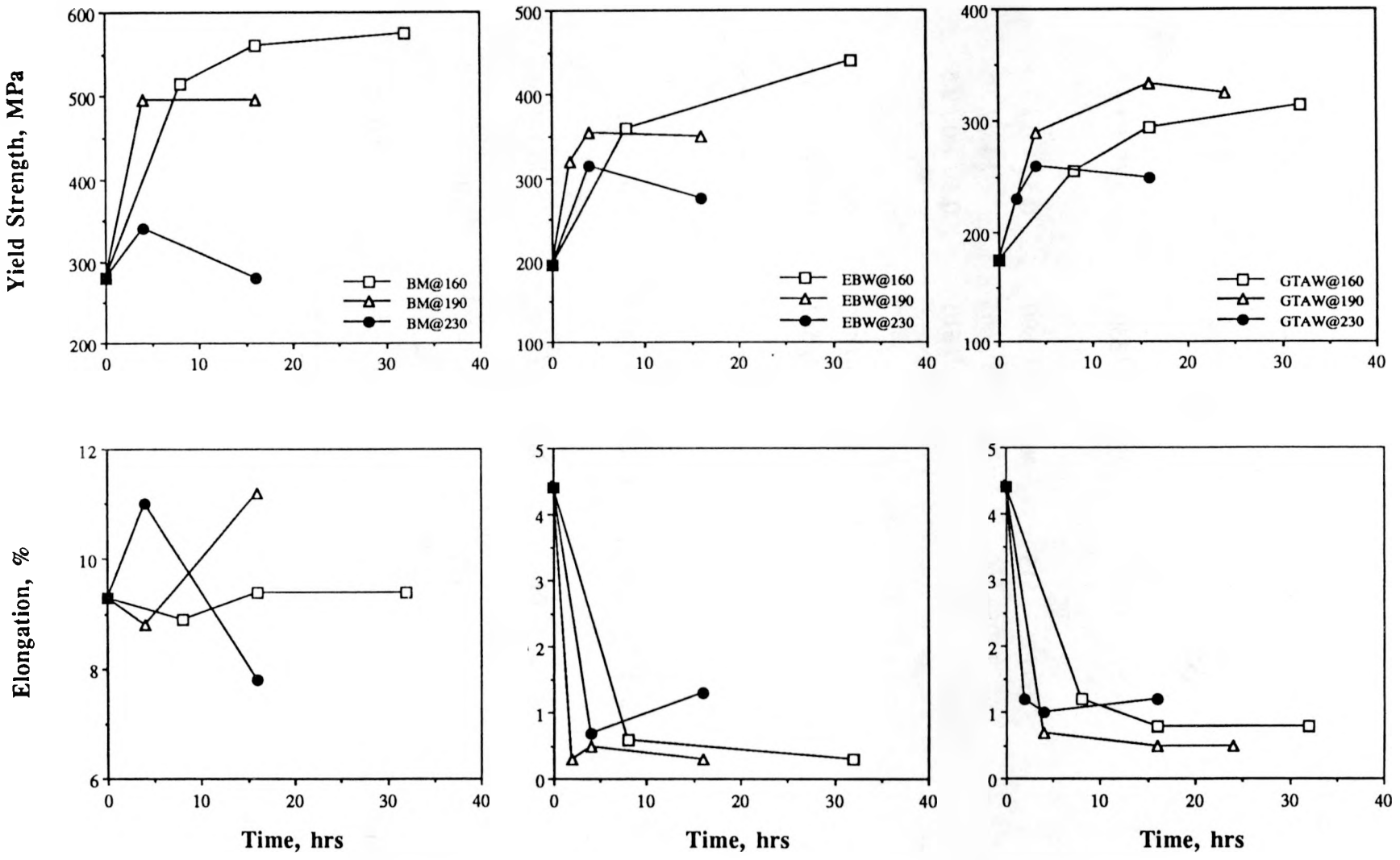

Figure III.18: Effects of various heat treatments on the yield strength and elongation of 2090, EB and GTA weldments.

D.5.2 The All-Weld Metal Tensile Behavior

The all-weld metal specimens in both the as-welded and aged conditions tend to have lower strength than that of the composite specimens. This may be due to the difference in the dendrite orientation and the base metal constraint on the fusion zone. The composite plots of true stress (σ) and the strain hardening rate ($d\sigma/d\varepsilon$) as function of true strain (ε) in Figure III.19 show that the as-welded all-weld metal specimen satisfied the necking criterion prior to failure. In case of the aged all-weld metal specimen, the specimen failed prematurely.

D.5.3 77 K Tensile Properties

The tensile properties of the base metal and the EB and GTA weldments tested at 77 K are summarized in Table III.3. With decreasing test temperature, the strengths of the base metal in both the T3 and aged conditions increased but the elongation decreased. The largest increase in the weldment yield strength was found in the as-welded condition with the EB weldments showing a 50% increase. The peak-aged EB weldment maintained its joint efficiency of 75% at both temperatures, but the GTA weldment joint efficiency decreased from 55% to 50% at 77 K. The aged weldments failed before reaching the ultimate strength at both test temperatures.

Table III.3 Tensile properties of electron beam weldments, gas tungsten arc weldments, and base metal tested at 77 K.

Heat Treatment (°C/Hours)	EBW/GTAW/BM σ_{YS} (MPa)	EBW/GTAW/BM σ_{UTS} [1] (MPa)	EBW/GTAW/BM Total Elongation (%)
As-welded/T3	300 / 240 / 345	405[1] / 325 / 460	1.0 / 2.0 / 11.5
PWA			
160/8	360 / 265 / 555	440[1] / 385[1] / 695	0.5 / 1.5 / 7.0
160/16	- / 305 / -	- / 385[1] / -	- / 0.5 / -
160/32	475 / 320 / 635	495[1] / 375[1] / 710	0.5 / 0.5 / 5.0

Note: Strengths given to nearest 5 MPa and elongations given to nearest 0.5%.
[1] Fracture strength.
[2] PWA: post weld aged condition.

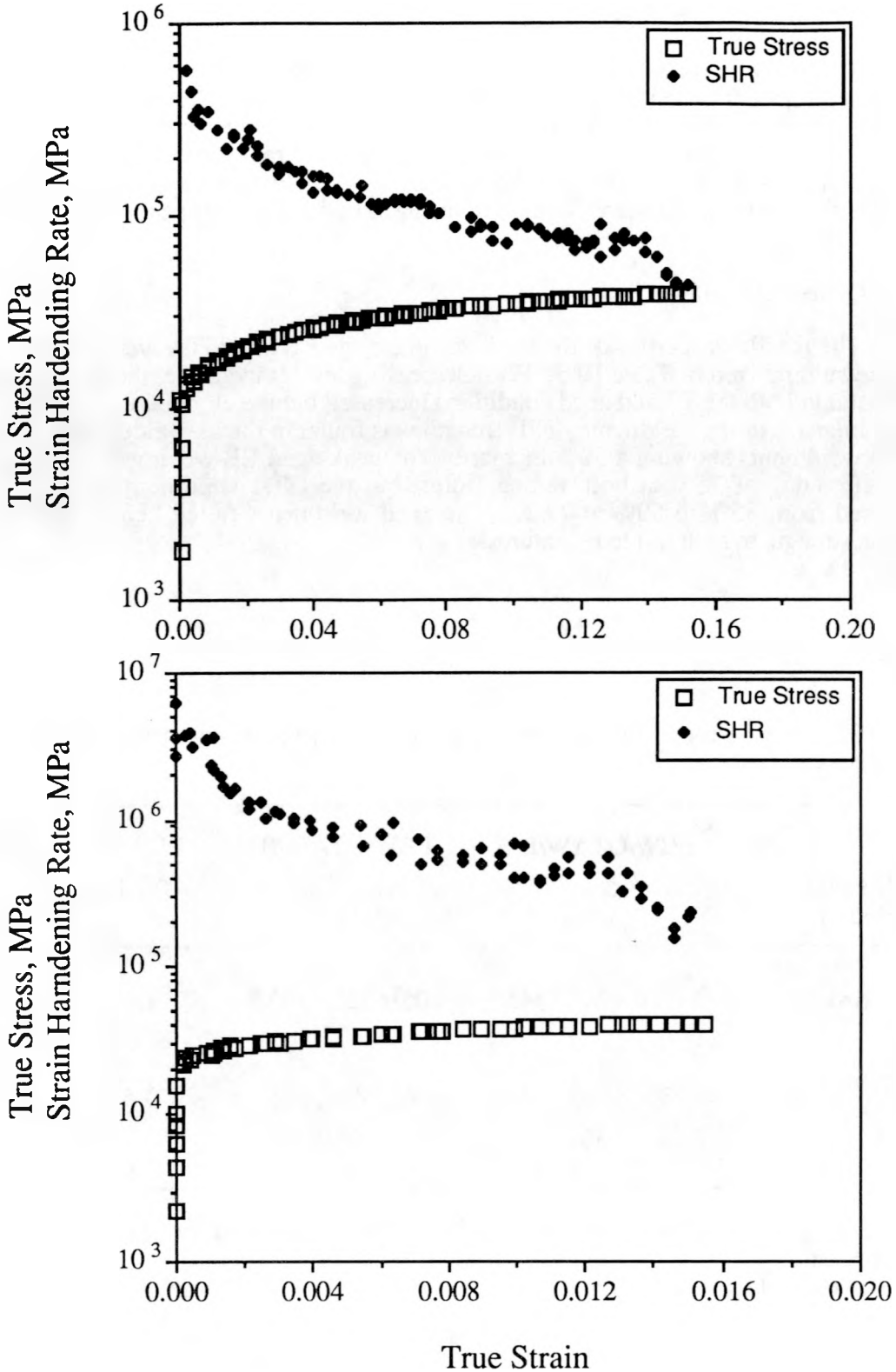

Figure III.19: Composite plots of true stress and strain hardening rate as a function of true strain for: a) as-welded, b) peak-aged all-weld metal GTA specimens.

D.6 Fractography

SEM fractographs showed different fracture modes for the base metal, EB weldments, and GTA weldments. The base metal tends to fail in shear. The fracture surfaces of the peak-aged base metal tested at 293 K and 77 K exhibit a typical bimodal fracture, a ductile failure with delamination in the through-thickness direction, Figure III.20. However, the fracture surface reveals more subgrain separation with decreasing test temperature.

The fracture surfaces of the EB weldments changed with the post-weld aging from ductile dimples in the as-welded condition to interdendritic failure in the peak-aged condition, but did not change with decreasing test temperature. Figure III.21 shows the EB fracture surfaces in the as-welded, peak-aged, and SHT&A conditions. The fracture surface of the as-welded EB specimens in Figure III.21a revealed ductile fracture with void formation and slip evident. Failures occurred at the fusion boundary. In the peak-aged condition, the fracture surface in Figure III.21b indicates interdendritic fracture, and failures occurred within the fusion zone. Very fine spherical particles decorated at the boundaries. For the SHT&A condition in Figure III.21c, a uniform void formation is observed at the dendrite surfaces but the fracture mode continues to be interdendritic fracture.

The GTA weldment fractures showed a mixed mode of ductile dimples and interdendritic fracture. Although the overall fracture mode did not change with subsequent aging and with decreasing temperature, the amount of deformation seen on the dendrite surfaces decreased from the as-welded to the peak-aged condition. Failure occurred close to the center of the fusion zone. Figure III.22 shows a fractograph and an optical micrograph of the under-aged GTAW specimens tested at 293 K. The fracture surface shows void formation and slip evident along the dendrite boundaries. Secondary cracks are seen along the dendrite boundary.

The fracture surface of the GTA specimen after SHT&A for 4 hours in Figure III.23a shows three distinct regions: the lamellar microstructure of base metal, the dendritic microstructure of the weld, and the partially melted region (PMR) of the HAZ. The PMR in Figure III.23b is identified by its smooth surface decorated with various size particles. PMR was also seen in the other fracture surfaces of the SHT&A GTA weldments. Figure III.24 shows the slip line formation in the dendrite surfaces of the SHT&A fracture specimen, where the lines are fine and uniformly distributed throughout the surfaces, compared to the as-welded fracture surface.

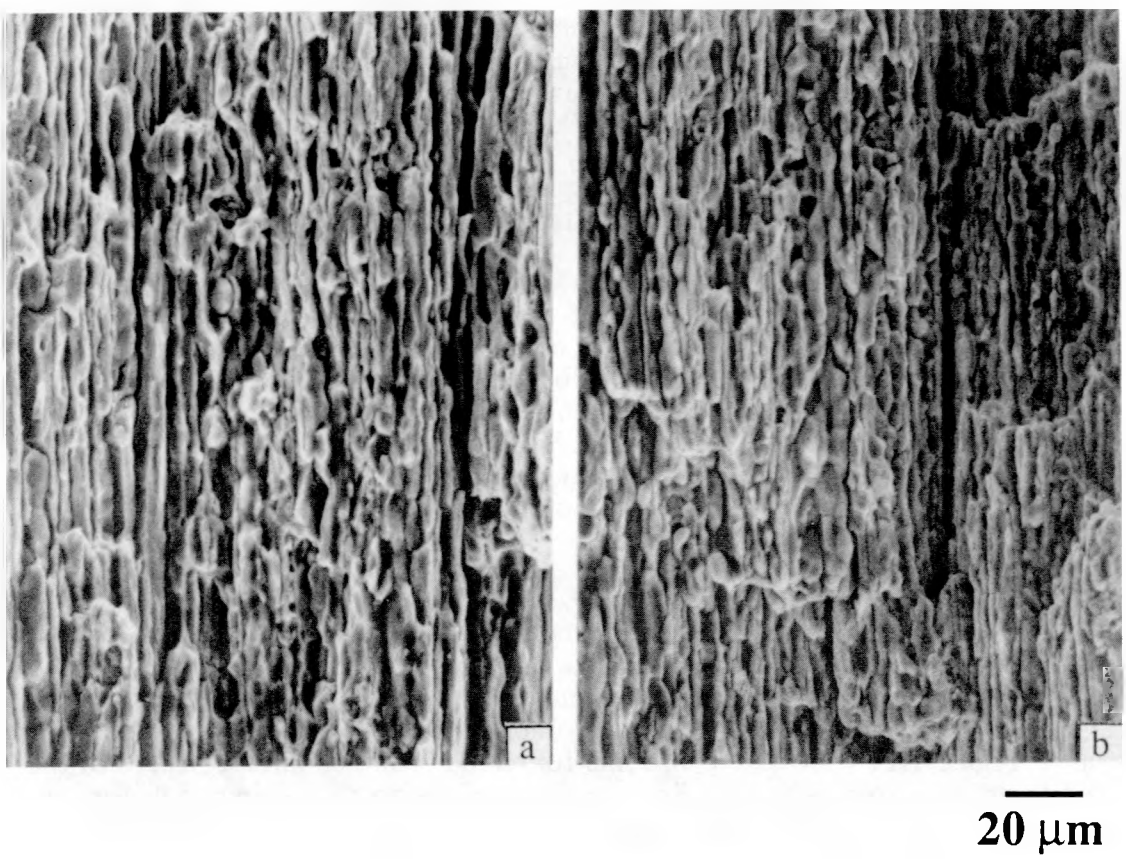

Figure III.20: SEM fractographs of 2090-T8 tested at: a) 293 K, b) 77 K. (XBB869-7889A)

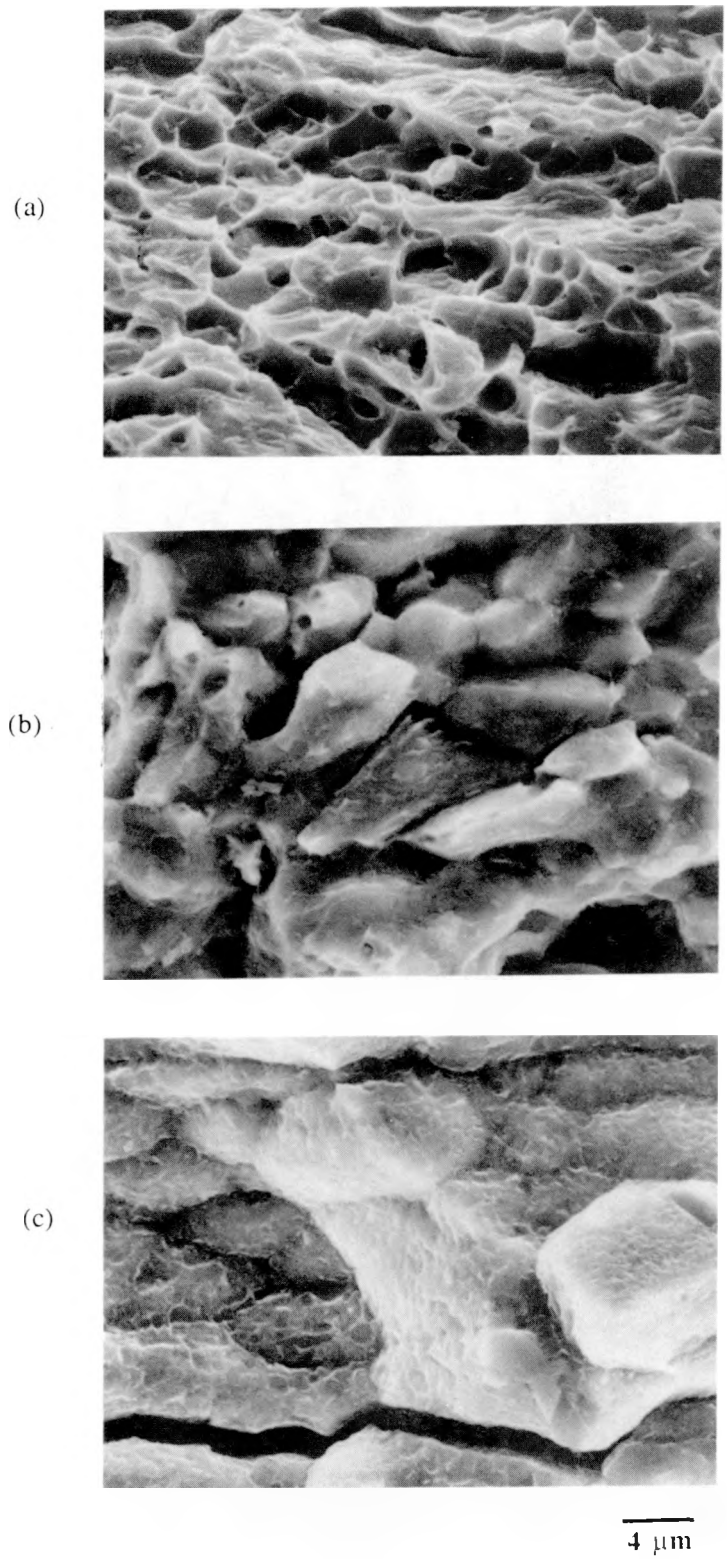

Figure III.21: SEM fractographs of EB composite weld specimens in various heat treated conditions: a) as-welded, b) peak-aged at 160κC for 32 hours, c) solutionized and aged at 160κC for 16 hours. The specimens were tested at 293 K. (XBB883-2256)

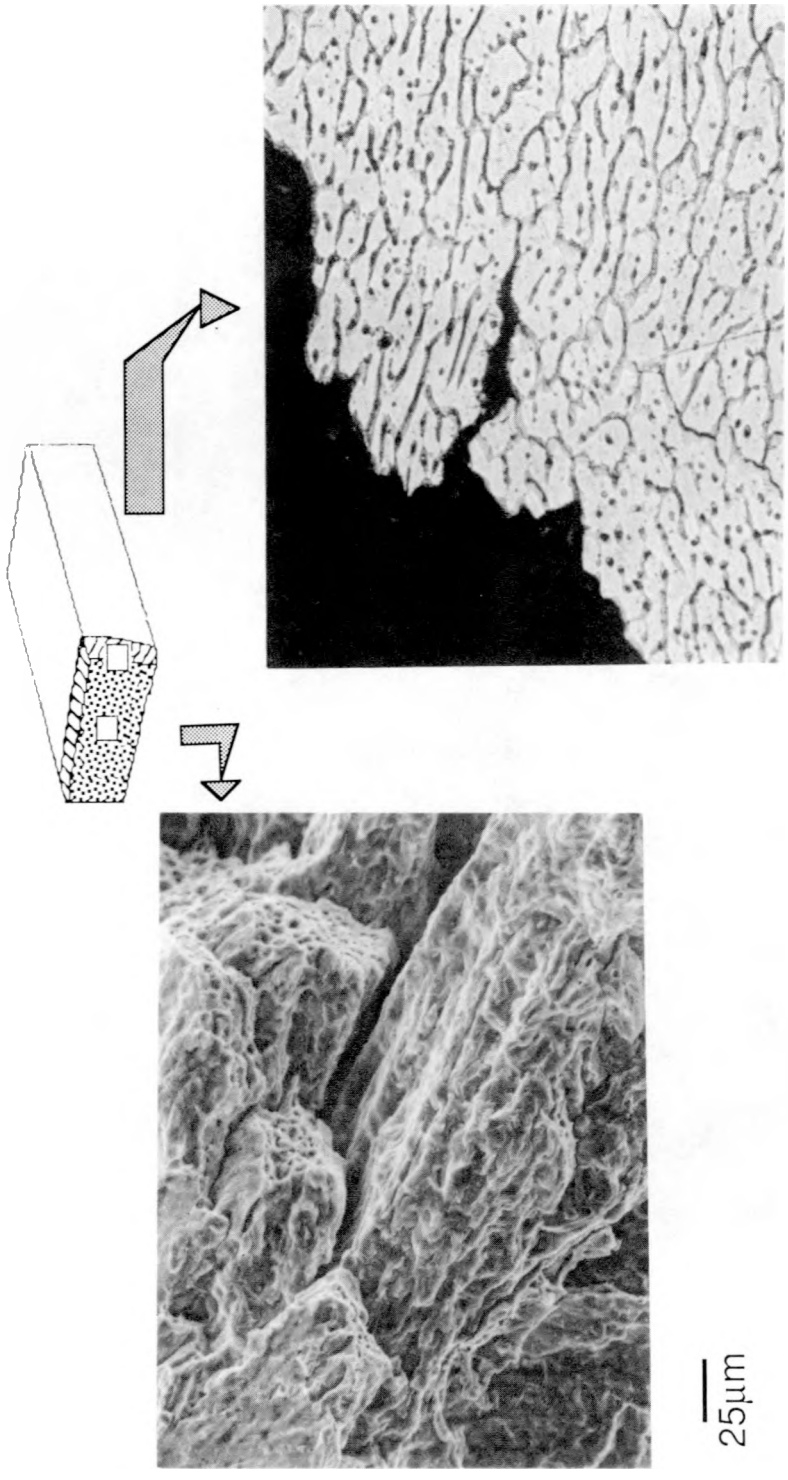

Figure III.22: a) SEM fractograph, b) optical micrograph of composite GTA weld specimens. The specimens were aged at 160°C for 16 hours and were then tested at 293 K. (XBB872-1035A)

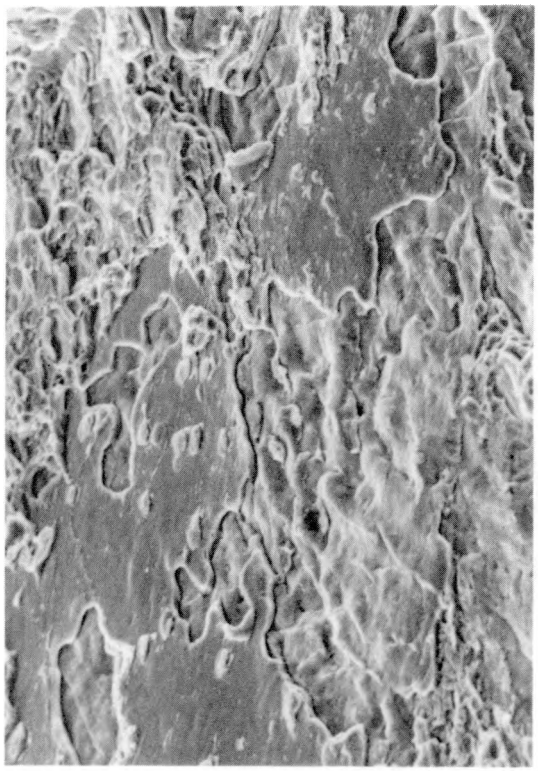

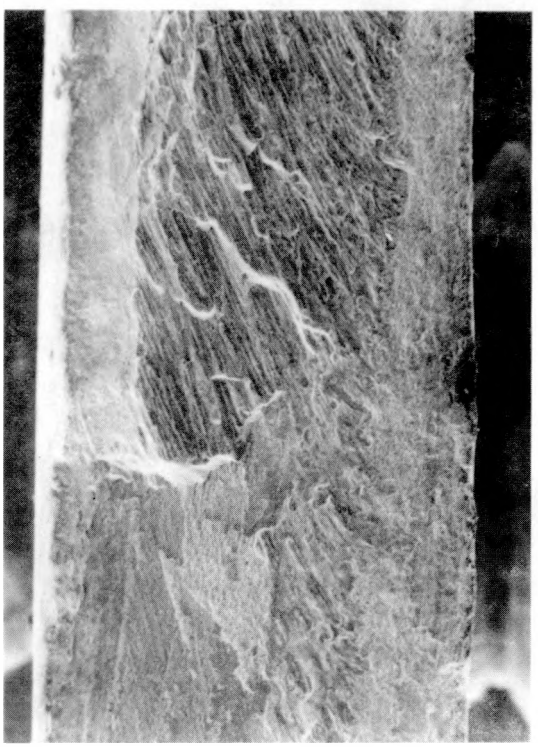

Figure III.23: SEM fractographs of GTA weld specimens in the solutionized and 4 hour aged condition: a) overall fracture surface, b) partially melted region. (XBB879-8277C)

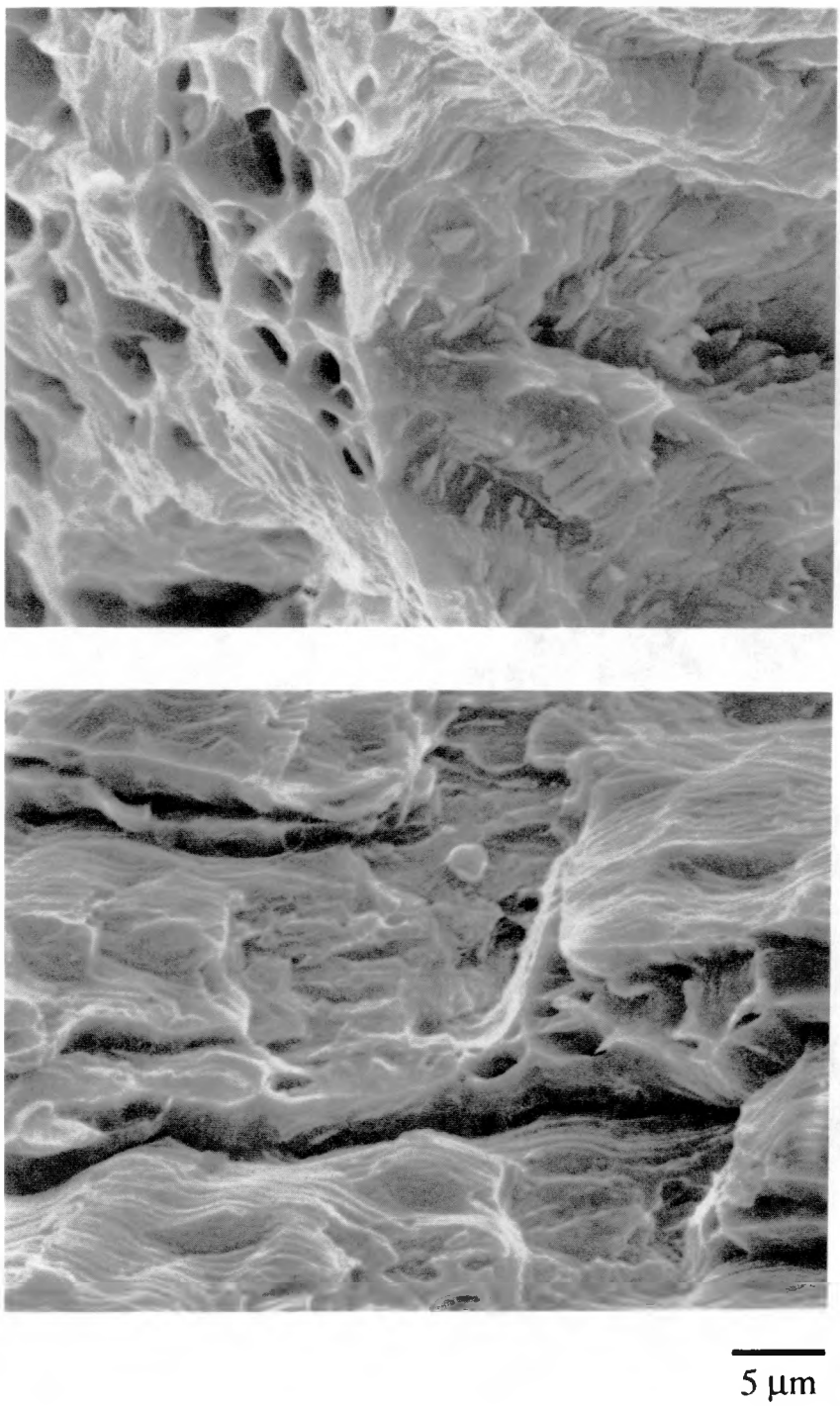

Figure III.24 SEM fractographs of a) as-welded, b) solutionized and 4 hour aged GTA weld specimens comparing the slip line formation. (XBB903-2649)

E. DISCUSSION

E.1. The Base Metal

Thermomechanical processing of the base metal has been developed to produce a beneficial combination of the size, volume fraction, and distribution of the strengthening precipitates [Hunt, 1983]. However, because δ' is a coherent, ordered phase, and T_1 is coherent with respect to the {111} matrix planes, these precipitates are easily sheared by dislocations [Sanders and Starke, 1982; Gregson and Flower, 1985, Jata and Starke, 1986]. The effectiveness of these precipitates as strengtheners is reduced once shearing occurs. As the dislocation pile-up and stress concentration increase with increasing strength, well-defined intense slip bands were observed in the peak-aged condition [Jata and Starke, 1986]. At 77 K, the increase in strengths is credited to a higher strain hardening rate, which is a result of a more homogeneous deformation [Glazer, et al, 1987].

The delamination of the base metal in the through-thickness direction may be caused by failure between the hard, incoherent precipitate, T_2, and the adjacent matrix [Vitatek and Chell, 1980; Van Stone, et al., 1985; Owen, et al., 1986; Vasudevan and Doherty, 1987; Graf and Hornbogen, 1987]. As the stress concentration increases at the boundary, microvoids initiate and decohesion occurs along the grain boundary. The increase in subgrain separations in the fracture surfaces at 77 K suggests that the reduced elongation may be attributed to a greater dislocation interaction with T_1 precipitates at the subgrain boundaries.

E.2 The Fusion Zone

E.2.1 The As-Welded Condition

In the as-welded condition, the EB weldments have a better strength and elongation combination than the GTA weldments. The weld strength is determined by solid solution and fine δ' precipitates, which are controlled by the solidification and cooling rates. The elongation is influenced by the dendrite morphology, which is also controlled by the solidification rate. A fine, equiaxed dendritic structure has better deformation characteristics than the cellular dendritic structure because the equiaxed microstructure can accommodate strain better than the cellular microstructure.

The influence of dendrite morphology on elongation is exhibited in the as-welded and solution heat treated conditions. Considering that localized deformation and failure occur in the fusion zone, the effective gage lengths for the EB and GTA weldments are 3.2 mm and 6.4 mm, respectively; hence, the actual as-welded elongation is equivalent to 40% and 16%, respectively. The all-weld metal GTA weld specimens had 17% elongation. Moreover, in the solution heat treated condition, the composite EB weld specimens had greater than 18% elongation and failed in the base metal while the composite GTA weld specimens had 11% elongation but failed in the fusion zones. The presence of the continuous film on the dendrite boundaries had very little effect on the as-welded and solutionized properties, probably because the strength of the dendrite matrix is much lower than the dendrite boundary decohesion strength.

At 77 K, the increase in weld strengths may be attributed to greater dislocation interaction with solutes, since the as-welded condition showed the greatest increase in strength. However, the strength of the matrix now exceeds the strength of the boundary and a premature, interdendritic failure tends to occur [Dew-Hughes, et al., 1988]. Hence, at 77 K, a lower elongation is exhibited in both the as-welded and aged conditions.

E.2.2 The Aged Conditions

The inverse relationship between the strength and elongation is a critical problem in the fusion zone. The hardness profiles and tensile properties suggest that even with post-weld aging, the strength compatibility between the base metal and the weld is difficult to achieve due to the nature of solidification. In both the EB and GTA fusion zones, the dendrite matrices are depleted of Cu and few nucleation sites to precipitate T_1 phase. (The fusion zone composition is similar to the base metal composition, with no Li loss.) During solidification, Cu either segregates to the boundaries or accumulates in other intermetallics. The composition of the 2090 is such that enough Cu and Li are present to create a solute-enriched film around the boundaries [Pumphrey and Jennings, 1948; Pumphrey and Lyons, 1948]. Small amounts of Fe, Si, or Cl impurities interact with Cu and have a detrimental effect on elongation. This film formation is not a problem for the base metal since the alloy is homogenized and the Fe, Si, and Cl are distributed more homogeneously.

During the early stages of aging, the δ' is the only strengthening phase present. As the δ' precipitates and coarsens with time, the yield strengths of the 8 hour aged EB and GTA welds increase significantly, but the elongation starts to decrease. A lower EB elongation in the aged conditions is attributed to a combination of the matrix strength exceeding the boundary strength, a localization of θ', and the formation of intermetallics and films around the boundaries [Graf and Hornbogen, 1987], which promotes premature, interdendritic failure.

GTA weldments always fail in a mixed fracture mode, ductile dimples with secondary cracks along the dendrite boundaries. The nature of the cellular dendrite morphology (high aspect ratio, with the long axis in tensile direction) and the fracture surfaces suggest that failure occurs in two-steps [Ludtka and Laughlin, 1982]: first, the decohesion occurs between the dendrites due to the film formation (these individual dendrites may act as independent tensile specimens during deformation); second, voids initiate at precipitates and coalesce to cause ultimate failure. The amount of deformation seen on the dendrite surfaces decreases with aging.

An incubation time is required to precipitate the θ' and T_1 phases, and even after a 16 hour aging, the θ' and T_1 are found only near the boundaries or other intermetallics. Other studies [Raman, et al, 1970; Ceresara, et al., 1977; have shown that the binding energy of Li and vacancy is high enough to allow lithium to trap vacancies during quenching and reduces the mobility of vacancies. A simple diffusion distance estimate, using $x=2.4(Dt)^{0.5}$ with $D= 1.42\times10^{-17}$ (mm^2/s) [Ahmad and Ericsson, 1985], indicates that for 16 hour and 32 hour aging the diffusion distance is about 200 nm and 300 nm, respectively. These distances are comparable to the observed θ' precipitate localized zone size.

The β' precipitates were not found in either of the EB or GTA welds. The STEM-EDS showed no indication of Zr in the EBW fusion zones, while Zr-containing intermetallics were observed in the GTA fusion zone. Zr has relatively low diffusivity and tends to remain in solid solution during casting and only precipitates during homogenization [Gregson and Flower, 1987, Gu, et al., 1985]. The intermetallics seen in the GTA dendrites may contain Zr (Figure III.12), because the partition coefficient of Zr is slightly greater than unity and Zr tends to remain in the interior of the dendrites rather than segregate to the boundaries.

E.2.3 The Over-aged Condition

In the over-aged condition of both the base metal and EB and GTA weldments, the strength loss is due to the dissolution of δ', which accounts for up to 30 vol-% in the matrix. Although the growth of T_1 precipitates was observed in the matrix, T_1, by itself, is not effective enough to maintain the strengths.

At 230°C, the dissolution of θ' precipitates also occurs. The previous adverse effects such as the θ' localization, T_2 phase and continuous film formation at the boundaries on the EB elongation have either dissolved or coarsened. As such, the elongation increases slightly.

E.2.4 The Solutionized and Aged Condition

In the solutionized condition, prior thermomechanical processing of 2090 as well as inhomogeneity of Cu and Li in the fusion zone have been removed. The approximate cooling rate from the solutionized temperature to water quench is 4500°C/s. As a result, the strengths of the base metal, and EB and GTA weldments are primarily obtained by the solid solution strengthening of Cu and Li. In comparison to the T3 temper and the as-welded condition, the strengths of the base metal and weldments in the solutionized condition are much lower. Without stretching prior to aging, the δ' precipitates were the only strengthening phase present on subsequent aging. As a result, the strength of the 2090-T6 was much lower than that of the 2090-T8. As for the weldments, the strength-elongation combination were much better.

When the properties of the solutionized and aged base metal and weldments are compared to the peak-aged binary Al-Li alloy, since the primary strengthening phase is also δ', the strength and elongation of the solutionized and aged condition are significantly higher. Even the under-aged weldments have 15% higher strengths and better elongations than that of the peak-aged binary Al-Li alloy [Glazer, 1989]. The difference in strength can be attributed to the solid solution strengthening of Cu. [Dorn, et al., 1950]

Since the grain size is known to influence the yield strength of an alloy, the effect of grain size on the yield strength is compared between the GTA weld and the base metal. In general, the grain size dependence on the strength can be predicted using the Hall-Petch relationship [Dollar and Thompson, 1987]. The average grain size of the GTA fusion zone is 150 μm, while the average grain size of the base metal in the longitudinal direction is an order of magnitude larger. Qualitatively, the GTA weldment is expected to be stronger, but similar yield strengths are found for the GTA weldments and the base metal in the solutionized and also in the under-aged condition, see Table III.2. This indicates that the grain size has a limited influence on the strength of this alloy.

F. CONCLUSIONS

In the post-weld aged conditions, both the EB and GTA fusion zones lack the volume fraction and homogeneity of the strengthening precipitates.

1. In the as-welded condition, the weld strength is primarily determined by the Cu and very fine δ' distribution and the elongation is influenced by the dendrite morphology. The EB welds have better overall properties than the GTA welds.

2. In the under-aged condition, the primary strengthener is the δ' phase. The composition of 2090 is such that enough Cu and Li are present to coat the dendrite boundaries. When Fe, Si, or Cl impurities are also present at the boundary, the elongation decreases.
3. Even in the peak-aged condition, the precipitation of T_1 is limited. The T_1 precipitates are found either in the vicinity of other intermetallics or at the boundaries. The joint efficiencies of EB and GTA weldments are 75% and 55% at 293 K and 75% and 50% at 77 K, respectively, with low weldment elongations.

4. In the over-aged condition, the volume fraction of T_1 is too low to be an effective strengthener. The over-aged strength of the weldments is higher than the as-welded condition, but the strength is lower than the 8 hour aged condition.

5. In the solutionized condition, δ' is the primary strengthening phase present for both the base metal and the fusion zone. Thus, the strengths of base metal, and EB and GTA weldments are equivalent and the elongations of the weldments improve.

IV. EFFECTS OF ALLOY ADDITIONS TO THE 2090 FUSION ZONE

A. INTRODUCTION

As shown above, even with post-weld aging, the strength compatibility between the base metal and the weld is difficult to achieve because of the nature of solidification. In both the EB and GTA fusion zones the dendrite matrices are depleted of the Cu needed to precipitate the T_1 phase. Although the solution heat treated and aged condition provides the strength compatibility, it is difficult to accomplish in real application due to size limitation of the weldment. This section investigates the effects of filler metal additions to the fusion zone to improve the weld strengths, while keeping the processing constant. The Cu and Mg additions are chosen as the solid solution strengtheners. The Sc is added as a grain refiner. Emphasis is placed on simulating the actual welding condition, where the base metal is utilized in a near peak-aged condition and the weldment is tested in the as-welded condition.

B. EXPERIMENTAL PROCEDURES

The weld coupons used in this study were cut from the same as-received 2090-T3 sheet as in Chapter III. The weld coupons, in 100 mm x 150 mm dimensions, were aged at 160°C for 16 hours to a near peak-aged condition (designated as T8) and were subsequently machined from 4.3 mm to 3.2 mm to remove the processing oxide and to eliminate distortion. A square groove of 3.2 mm was machined in the center of the weld coupon, as shown in Figure IV.1, and the filler metal of 3.0 mm x 2.0 mm dimensions was to fit inside the groove.

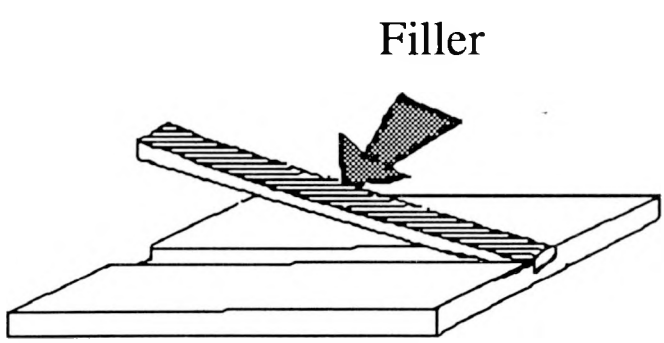

Figure IV.1: A schematic diagram of welding set-up used for filler metal addition.

Prior to welding, the weld coupons and filler additions were degreased and chemically cleaned sequentially with ethanol, and 5 vol-% sodium hydroxide in water, and were rinsed in concentrated nitric acid. The nominal compositions of the filler metal additions are listed in Table IV.1. Autogenous and filler added welds were produced using gas

tungsten arc (GTA) welding process on the T8 tempered base material. The welding condition is the same as the Chapter III. A higher heat input was used to produce a full penetration, filler added weld than autogenous weld, 635 J/mm vs. 310 J/mm. With the Mg containing fillers, the welding parameters had to be changed to prevent fusion boundary cracking, due to severe porosity. The travel speed decreased from 6.4 mm/s to 2.5 mm/s and the current was adjusted accordingly. The shielding gas flow rate was increased from 12 L/min to 19 L/min. Overall, it was more difficult to produce sound welds with the Mg containing fillers.

Table IV.1 Nominal chemical composition of filler metals (wt-%).

Filler Metal Designation	Cu	Mg	Sc	Al
6 Cu:	6.3	-	-	remainder
4 Mg+0.5 Sc:	0	4	0.5	"
3 Cu+4 Mg:	2.9	3.7	-	"
3 Cu+8 Mg:	3.2	8.2	-	"
6 Cu+4 Mg:	5.8	3.8	-	"

Both the autogenous and filler added welds were produced transverse to the longitudinal direction of the base metal in an inert atmosphere on a water-cooled chill block. After welding, the weldments were machined into tensile specimens, reducing the final thickness to 2.54 mm. In this study, the base metal tensile specimens are made in the longitudinal orientation. The tensile specimen configurations are the same as the ones shown in Figure III.1. Both the T8 tempered base metal and the as-welded composite weld specimens were tensile tested at 293 K and 77 K.

C. RESULTS

C.1 The Fusion Zone Microstructure

Figure IV.2 shows SEM micrographs of polished autogenous, 6 Cu, Mg-Sc, and 6 Cu-4 Mg added 2090 fusion zones. With the higher Cu content in the fusion zone (Figure IV.2.b), Cu segregation is more prominent at the boundaries, but the distribution is discontinuous. The Mg additions (Figure IV.2c and IV.2d) changed the dendrite morphology to a more cellular dendritic structure and the continuous Cu-containing interdendritic phases outlined the boundaries. The changes in the fusion zone microstructure and the distribution of Cu-containing interdendritic phases are expected to influence the deformation behavior in the fusion zone .

C.2 Composition of the Fusion Zone

The composition of autogenous, 6 Cu, and Mg+Sc welds was analyzed using atomic absorption spectroscopy (Table IV.2). About 40% of the filler metal was diluted into the 2090 fusion zone. With 6 Cu addition, the mean Cu content increased from

2.8 wt-% to 3.7 wt-% and Li decreased from 2.2 wt-% to 1.6 wt-%. With Mg+Sc addition, Mg content increased to 1.4 wt-% while Cu and Li contents decreased to 2.4 wt-% and 1.4 wt-%, respectively. As the fusion zone composition change with the filler addition, the Vickers hardness traces across the fusion zones indicate that the autogenous and 6 Cu-added fusion zones were the softest with an averaged hardness number of 105, while the fusion zone of 6 Cu-4 Mg addition was the hardest with an averaged hardness number of 135.

Table IV.2 Chemical composition of the fusion zone (wt-%).

	Cu	Li	Mg	Zr	Al
2090	3.0	2.2	-	0.2	remainder
autogenous	2.8	2.2	-	0.2	"
6 Cu	3.7	1.6	-	0.1	"
4 Mg+0.5Sc	2.4	1.4	1.4	0.1	"

C.3 Tensile Behavior

C.3.1 293 K Tensile Properties

The 293 K tensile properties of the base metal and GTA weldments with various filler metal additions are presented in Table IV.3. When the strengths of a near peak-aged base metal and the weldments are compared, the difference in the strengths between the parent metal and the weld is obvious. Even with the alloy additions, the ultimate tensile strength (UTS) of the weldments is only 50% of the base metal yield strength. Consequently, deformation is confined to the softer fusion zone in the weldment. For the 6 Cu added fusion zone, necking occurred at both temperatures, and some deformation extended into the HAZ at 77 K. With Mg+Sc addition, necking also occurred in fusion zone at 293 K, but very little deformation was seen at 77 K. The other Cu-Mg added welds showed very little deformation even at 293 K, and tend to fail prematurely at both test temperatures.

When the strengths of the autogenous and the filler added welds are compared, the filler added welds show limited increase in strength for the amount of change in the fusion zone composition. Although the yield strength of the 6 Cu added welds is the lowest, the elongation is superior to that of the autogenous and Mg-containing additions by about 300%, and the UTS is roughly the same. With the 4 Mg additions, the yield strengths increased slightly but had an adverse effect on the elongation, except for the Mg+Sc addition. The higher Mg addition did not improve either the strength or the elongation.

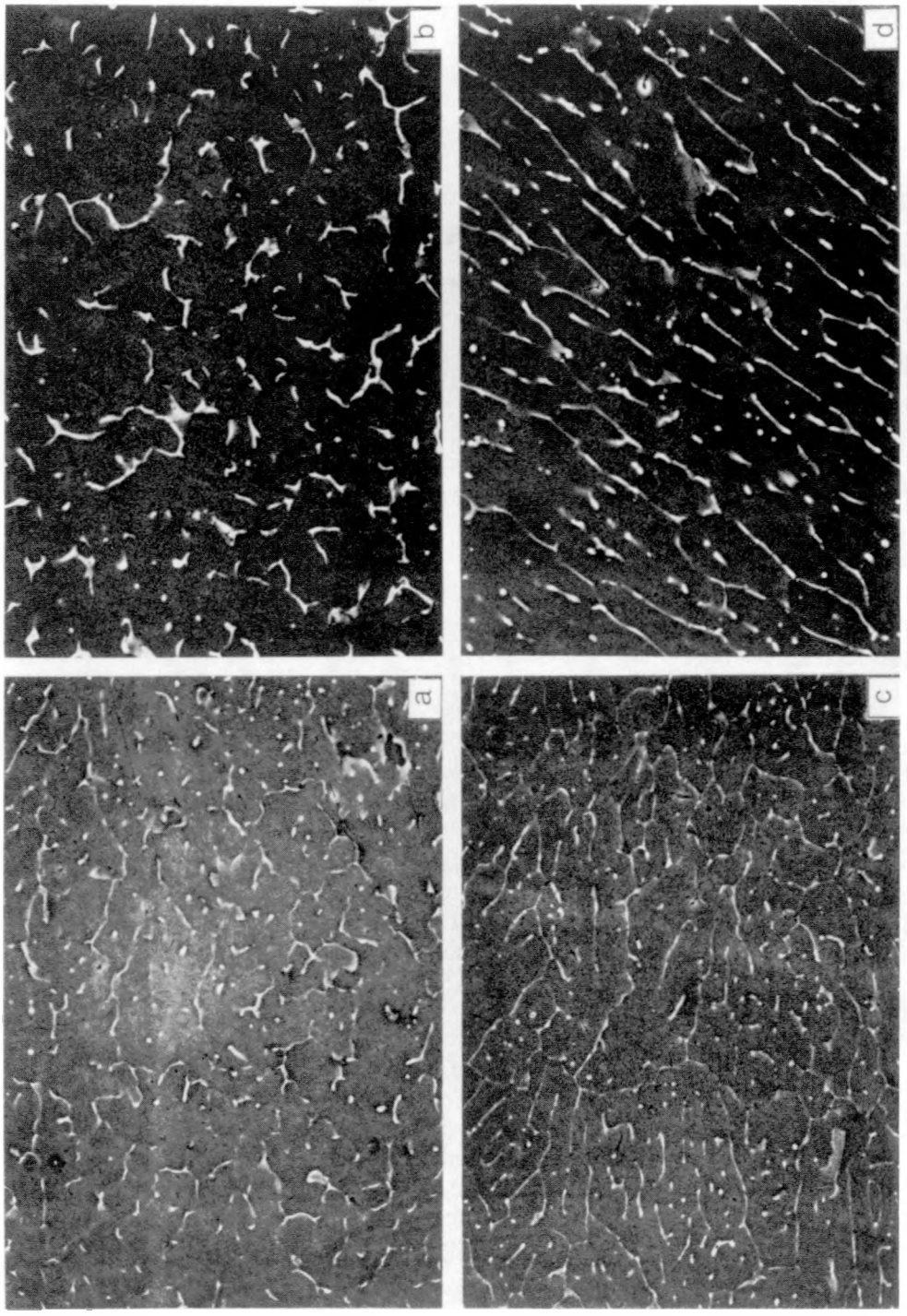

Figure IV.2: SEM micrographs of polished top surface of: a) autogenous, b) 6Cu added, c) 4Mg+0.5Sc added, d) 6Cu+4Mg added 2090 fusion zones. (XBB892-988)

Table IV.3 Tensile properties of the base metal, and autogenous and filler added gas tungsten arc weldments tested at 293 K and 77 K.

Filler Additions	σ_{YS} MPa	σ_{UTS} [1] MPa	Total Elongation (%)
293 K			
Base Metal	500(72)	525(76)[1]	1.3
Autogenous	150(22)	260(38)	4.5
6 Cu	140(20)	265(39)	13[2]
6Cu+4Mg	180(26)	259(38)[1]	1.5
3Cu+4Mg	175(25)	245(36)[1]	1.5
3Cu+8Mg	155(23)	240(35)	2.0
4Mg+0.5Sc	190(27)	270(39)	4.5
All Weld Metal Specimens[2]			
Autogenous	135(20)	250(36)	17.0
6 Cu	105(15)	240(35)	13
3Cu+4Mg	150(22)	275(40)[1]	7
77 K			
Base Metal	525(76)	625(91)	6.0
Autogenous	160(23)	255(37)[1]	1.5
6 Cu	185(27)	370(54)[1]	10.5
6Cu+4Mg	-	185(27)[1]	0.2
3Cu+4Mg	-	215(31)[1]	0.1
4Mg+0.5Sc	-	240(35)[1]	0.2

Note: Strengths given in nearest 5 MPa and elongations given in nearest 0.5%.
[1] Fracture strength.
[2] See specimen configuration in Fig. III.1.

C.3.2 All-Weld Metal Tensile Behavior

Without the base metal constraint to the fusion zone, the all-weld metal specimens tend to have a lower yield strength than that of the composite specimens. Of these, the Mg added all-weld metal specimen displayed higher strength. The elongations exhibited in the all-weld metal specimens are the true elongations of the weldments.

When the true stress (σ) and the strain hardening rate ($d\sigma/d\varepsilon$) as a function of ε are compared between the autogenous and 6 Cu added all-weld metal specimens (Figure IV.3), the necking criterion was satisfied for both welds. However, the slopes of the strain hardening rate versus ε are different for the autogenous and 6 Cu added all-weld metal specimens. For the 6 Cu added all-weld metal specimen, the slope of strain hardening rate tends to be less steep at the beginning but shows a sharp decline at near the necking point. The specimen failed in shear.

C.3.3 77 K Tensile Properties

At 77 K, the autogenous and 6 Cu added welds are the only weldments that failed after yielding. In addition, the 6 Cu addition led to at least 30% increase in strength while maintaining its elongation at 10%. At both temperatures, the elongations of 6 Cu addition were even better than that of the base metal. All the Mg containing welds have failed prior to or at yielding.

C.4 Fractography

The fracture surfaces of autogenous weldments did not change with the test temperature and continue to show a mixed fracture mode, as describe in Chapter III. Figure IV.4 compares the fracture surfaces of the 6 Cu and 6 Cu-4 Mg welds tested at 293 K. The 6 Cu welds failed in shear and the fracture surface appeared planar with slanted dimples. The fracture mode of the Cu-Mg combined welds was similar, predominantly interdendritic; the fracture surface of a 6 Cu-4 Mg specimen tested at 293 K (Figure IV.4b) shows very brittle dendrite surfaces. The fracture surfaces of the Mg-Sc added welds in Figure IV.5 change in mode from mixed to predominantly interdendritic as the test temperature decreases to 77 K.

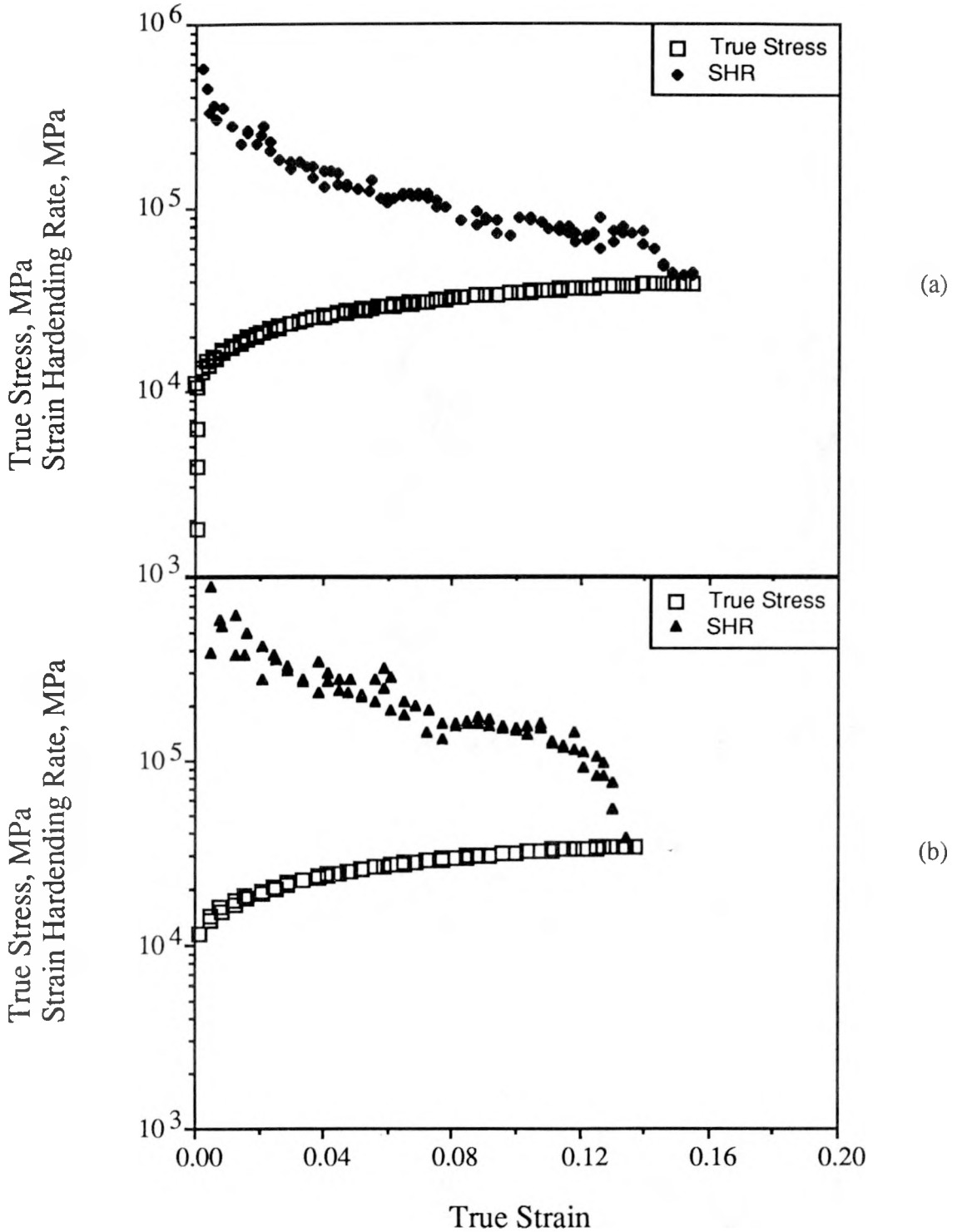

Figure IV.3: Composite graphs of true stress and strain hardening rate as a function of true strain: a) autogenous, b) 6 Cu added all-weld metal GTA specimens.

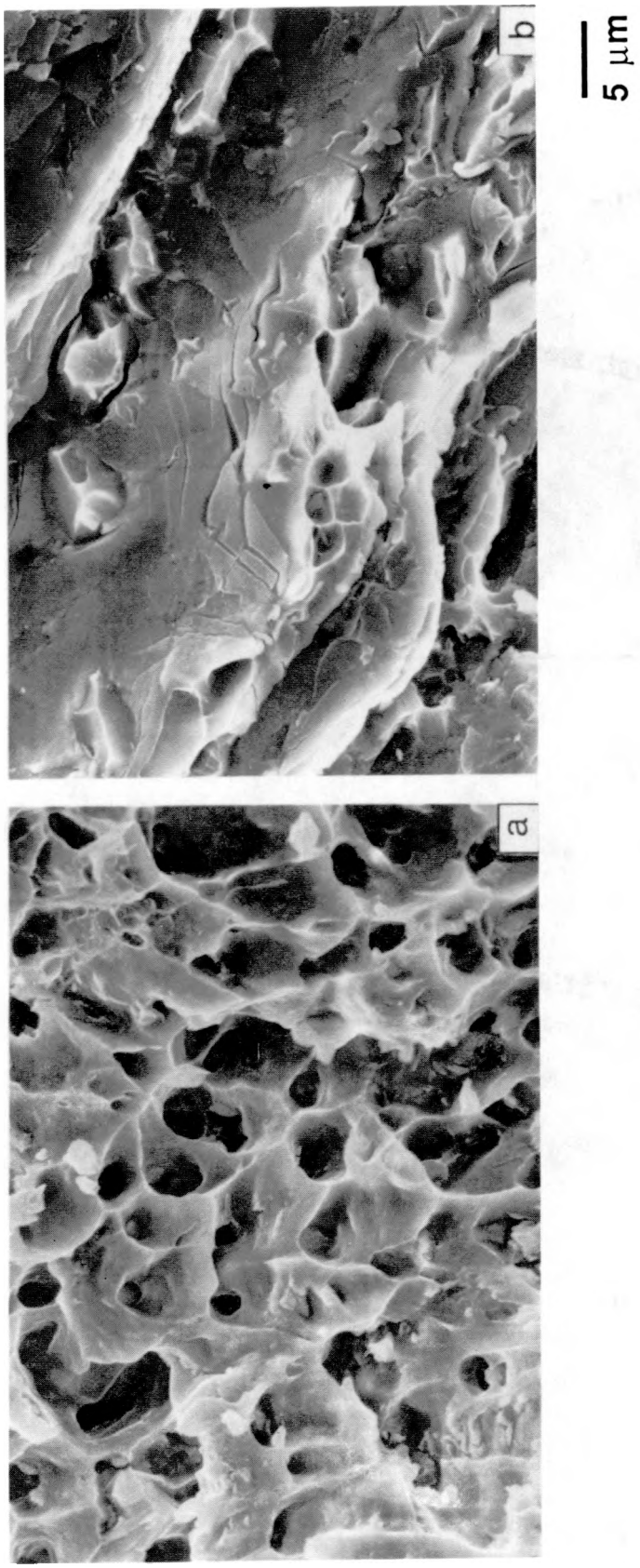

Figure IV.4: SEM fractographs of a) 6Cu added, b) 6Cu+4Mg added 2090 welds tested at 293 K. (XBB892-990)

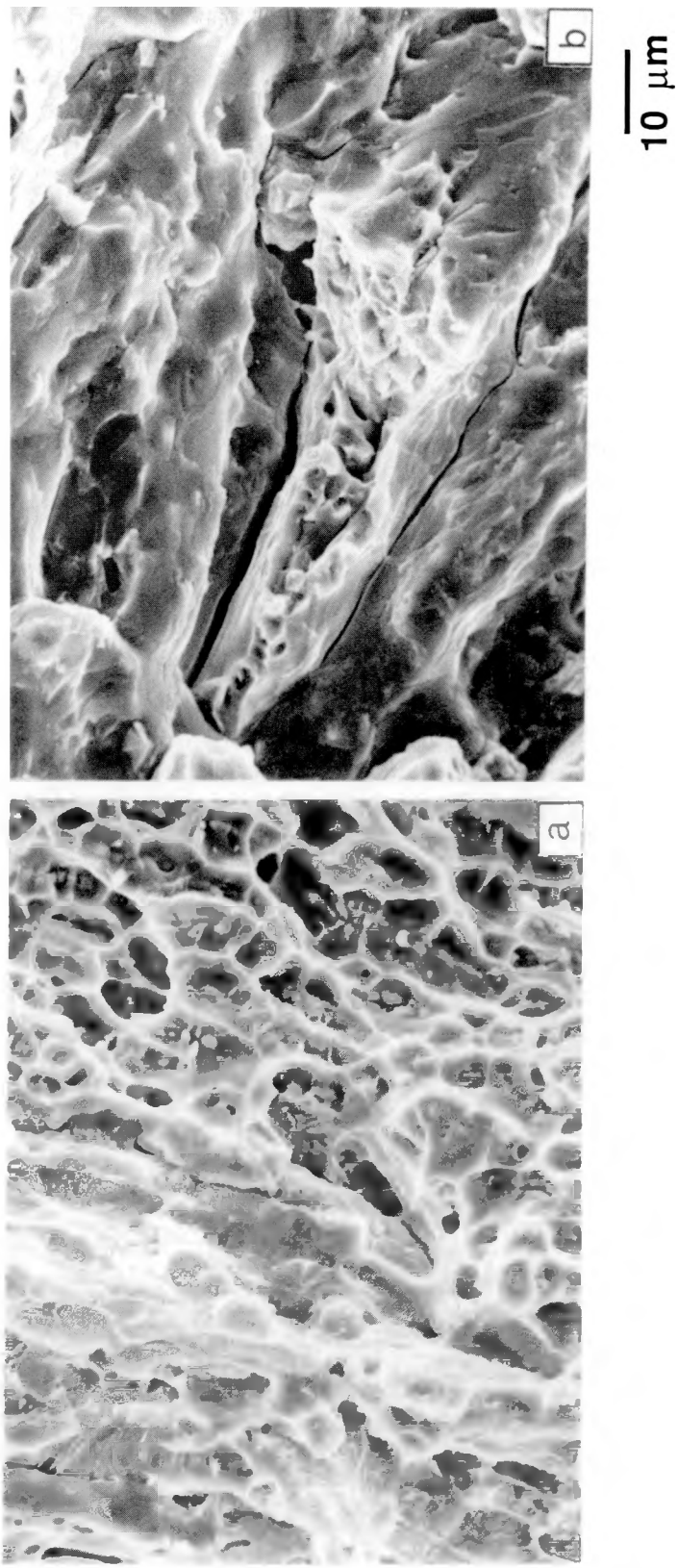

Figure IV.5: SEM fractographs of 4Mg+0.5Sc added 2090 welds tested at: a) 293 K, b) 77 K. (XBB892-989)

D. DISCUSSION

Current practice in the industry is to peak age the base metal prior to welding and to utilize the weldment in the as-welded condition. With the T3 tempered base metal, the joint efficiency of the as-welded GTA weldment is 65%, and with the T8 tempered base metal, the joint efficiency decreases to 30%. Since deformation and strain localization are confined to the softer fusion zone, it is therefore unnecessary to peak-age the base metal when the failure is going to occur in the weaker fusion zone.

However, there are advantages and disadvantages to the base metal constraint to the fusion zone. The base metal constraint to the fusion zone induces a notch strengthening effect, which tends to increase the fusion zone strength. However, the notch strengthening does not increase the fusion zone strength enough to initiate homogeneous deformation throughout the weldment.

Even with the alloy additions, the solid solution strengthened fusion zone is incapable of achieving the strength of the precipitate strengthened base metal. On the other hand, the solid solution strengthening potential of Cu is not fully utilized in the fusion zone due to the nature of solidification. During solidification, a pronounced Cu segregation occurs to the dendrite boundaries and the dendrite matrices are depleted of Cu, limiting the Cu available in the matrix for strengthening. The averaged hardness number of the 6 Cu added weld was the lowest, compared to other filler added welds. The increase in strength is feasible with Mg additions, but the Cu-Mg combination leads to embrittlement at 77 K. With the Mg-containing fillers, it is difficult to produce defect-free welds. Ishchenko, et al. [1982] examined the cryogenic weldment properties of Al-Mg-Mn alloys, and also reported brittle fracture at low temperature. However, they attributed the embrittlement to the Fe and Si contents.

Similar to this work, a problem of fusion zone porosity was observed with the Mg-containing parent materials, such as 8090, 8091 [Wu, et al., 1987], and even the Soviet-developed Al-Mg-Li-Zr alloy, 01420 [Pickens, 1985], which is known to have "good" weldability. Even with the other alloys, the strength incompatibility between the parent metal and the weld, and the inverse relationship between the strength and ductility in the weld are the continuing problems in the weldment. Edwards and Stoneham [1987] investigated the weldability of 8090 with various filler additions and found that the fracture mode changes with the filler additions. 8090 with 8090 filler had about 40% higher yield strength than that of 8090 with the higher Mg-containing filler but exhibited lower ductility and brittle intergranular fracture. 8090 with the higher Mg-containing filler tends to fail transgranularly.

Intergranular fractures are also seen in the Al-Cu-Li-Mg alloys. Several mechanisms have been proposed to interpret this behavior. Owen, et. al. [1986] have identified that the S phase (Al_2CuMg) and Fe-Cu rich intermetallic, $Al_6(Fe,Cu)$, form adversely at the grain boundaries of the as-cast material. Even after solution heat treatment, the Fe-rich phase was still present at the grain boundaries. They concluded that the Fe-rich phase nucleates voids at the grain boundaries, which subsequently leads to premature failure, reducing the overall ductility. Miller, et. al. [1986] have characterized the grain boundary precipitates as δ- and T-phases, or Fe-Cu rich intermetallic which contribute to intergranular failure.

The 2xxx and 5xxx series Al alloys, the Al-Cu and Al-Mg systems, respectively, seem to maintain good weld strength-ductility combination at both ambient and cryogenic temperatures, even though there is some trade-off between the strength and ductility [Kaufman and Johnson, 1960]. The best elongation values were observed for those parent

and filler alloys having the same strength level. The strength compatibility between the parent and weld decreases the tendency for localized deformation in the weld; hence a greater degree of homogeneity in the weldment is achieved [Nelson, et al. 1969].

The results of the present work suggest that low weld ductility is associated with the Cu-Mg combination in the weld. Although just Al-Cu-Mg system has not been studied, the source of low ductility in 8090 has been attributed to the grain morphology rather than the grain size, since the 8090 EB welds with much finer grains have failed brittle and intergranularly and small additions of Zr did not significantly increase the strength or ductility [Edwards and Stoneham, 1987]. From this work, the Cu-Mg combination seems to change the fusion zone microstructure to more cellular dendritic structure with the continuous interdendritic phases outlining the boundaries. Energy dispersive x-ray spectroscopy of the interdendritic phases found small concentration of Fe or Si in the Cu-Mg combined fusion zones. Even though microsegregation of Fe or Si is present in the interdendritic phases, they may play minor roles in promoting embrittlement. The difference between the Cu added welds and the Cu-Mg combined welds is that in the Cu-Mg combined welds, the solutes tend to segregate and coat the cellular dendrites, forming continuous, brittle surface. At low temperature, intergranular failure intrudes because the strength of the grain interiors is greater than that of the grain boundary [Dew-Hughes, et al. 1988].

E. CONCLUSIONS

The effects of alloy additions to the fusion zone have been investigated to improve the weld strength.

1. In the weldment, deformation and failure tend to occur in the softer fusion zone. The strength mismatch is present due to the difference in strengthening mechanism: the fusion zone obtains its strength through solid solution strengthening and the base metal obtain its strength through precipitation strengthening. As a result, the ultimate tensile strength of the weld is only 50% of the base metal yield strength.

2. A substantial increase in weldment elongation can be accomplished by increasing the Cu content in the fusion zone. At the 77 K test temperature, a 6 Cu addition has the best combination of UTS and elongation of all the weldments tested in this work.

3. The Mg additions to 2090 change the fusion zone microstructure to more cellular dendritic structure, which affects the distribution of Cu segregation at the boundaries. The Mg added welds show higher yield strengths, but the Cu-Mg combination leads to brittle, interdendritic fractures at both the 293 K and 77 K test temperatures.

V. EFFECTS OF THERMAL CYCLES ON THE HEAT AFFECTED ZONE

A. INTRODUCTION

This section focuses on the heat affected zone (HAZ) of the weldment. The HAZ is created by the high local temperature that was present during welding. Heat conduction from the weld pool causes microstructural changes in the HAZ which in turn cause changes in the mechanical properties. Unlike the fusion zone and base metal properties, the HAZ properties are influenced by the initial base metal mechanical properties and heat conduction from the fusion zone. This region is particularly of interest since 2090 properties are obtained through precipitation-strengthening, any thermal cycle will affect the precipitation behavior. As the strength of the fusion zone increases with the alloy additions, the HAZ will be the next weakest region in the weldment.

The purpose of this study is to investigate the effects of HAZ thermal cycles on the microstructure and properties of 2090 Al alloy in the T3 and T8 tempered conditions. Because the HAZ is an intricate part of the weldment, it is difficult to isolate and to test only the HAZ. The approach used in this study is to obtain experimentally sthe temperature history of the HAZ and to simulate it using a GLEEBLE. The thermal cycle can be divided into three regimes: heating, peak temperature, and cooling. The effects of the three regimes have been studied independently, and only the peak temperature was found to have a significant influence on the response of precipitates [Dumolt, 1983]. Emphasis is placed on the effects of various HAZ peak temperatures on the microstructure and mechanical properties of 2090.

B. BACKGROUND

B.1 Motivation for the Study

The motivation for the HAZ study of 2090 is shown in the Vickers hardness profiles of the weldments. The profile after gas tungsten arc welding (GTAW) on the T3 tempered base metal (T3 represents solution heat treatment and stretch.) exhibits a peak in hardness at a certain point in the temperature gradient. When the effect of base metal tempers is compared for a constant heat input, the profile after GTAW on the T8 tempered base metal (T8 represents T3 temper with subsequent peak-aging.) shows a higher hardness in the unaffected region and then a gradual decrease to the fusion boundary with some levelling of the hardness at certain points in the temperature gradient, Figure V.1a. Moreover, when the effect of the different heat inputs of electron beam welding (EBW) and GTAW on the HAZ is compared for a constant base metal condition, such as T8, the slopes of the profiles are very similar and the primary difference is the HAZ size, Figure V.1. The base metal temper does have influence of the HAZ behavior.

B.2 Other Studies

The HAZ microstructure of welded 2219 and 6061 alloys has been characterized by Dumolt [1983], who found that the HAZ transformation in 2219 is dominated by the dissolution of precipitates, while changes in 6061 are dominated by precipitate coarsening. A brief HAZ study [Martukanitz, et al., 1987] of 2090 showed that when the peak temperature of the HAZ exceeds the phase solvus temperature, dissolution of the strengthening phase (and degradation of properties) occurs. However, no detailed study has been conducted to correlate these microstructural changes to the mechanical properties. Other studies [Zacharia and Aidun, 1988; Balaguer, et al., 1989] have focussed mainly on

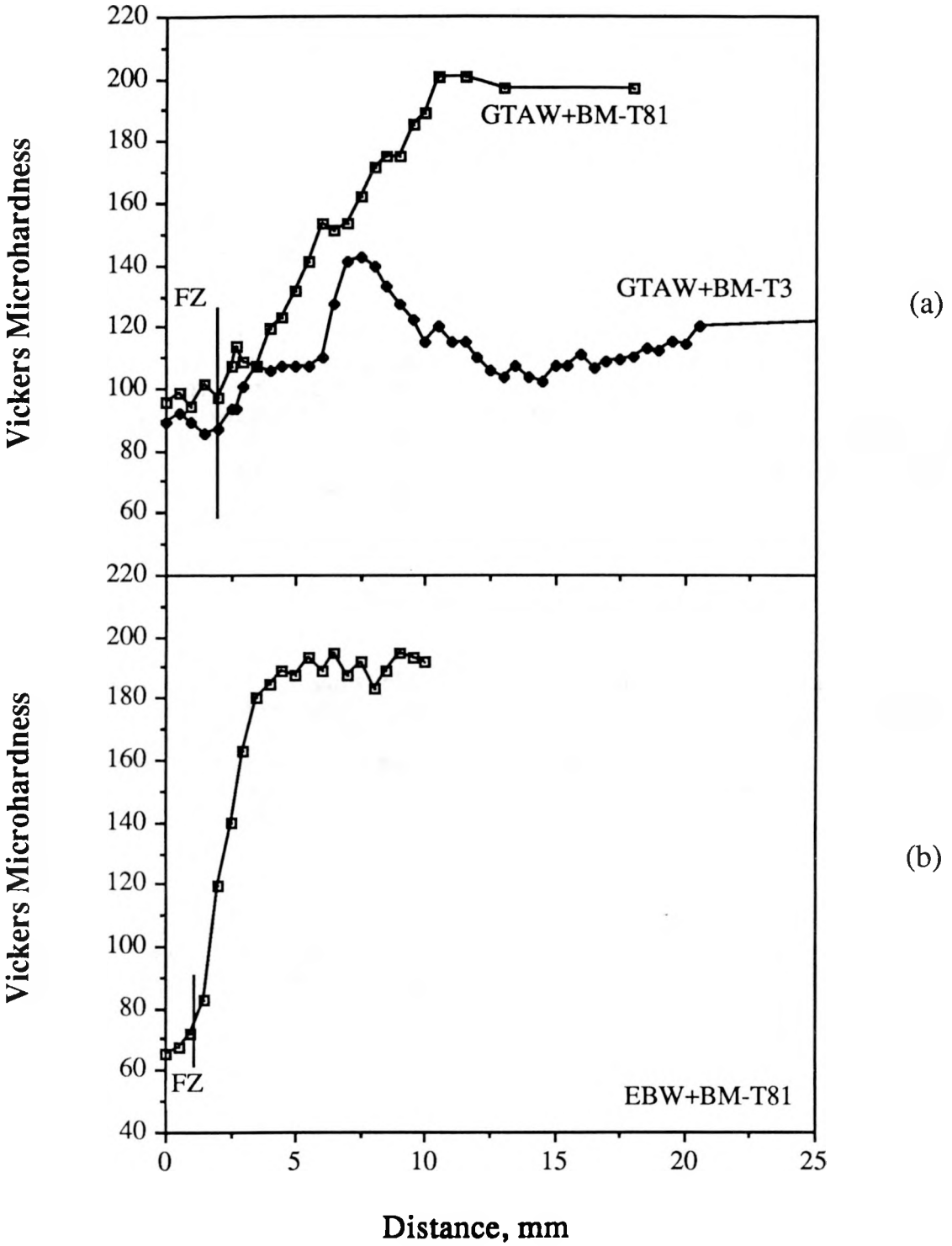

Figure V.1: Vickers hardness profiles of the weldments from the fusion zone to the unaffected base metal after: a) gas tungsten arc welding on the T3 and T8 tempered base metal, b) electron beam welding on the T8 base metal. These hardness profiles are from a single pass, full penetration weld on a 3.0mm sheet.

the hot cracking and hot ductility of the HAZ. Since 2090 is being considered for cryogenic, welded application, the knowledge of the HAZ properties at temperature is essential.

C. EXPERIMENTAL PROCEDURE

The nominal composition of 2090 Al alloy is, in wt-%, 2.8 Cu-2.2 Li-0.12 Zr-Al. The as-received T3 and T8 tempered 2090 microstructures consist of fine equiaxed grains with residual texture in the rolling direction. The T8 tempered 2090 is shown in Figure V.2.

The hardness profile of GTAW-T3 in Figure V.1a was used to determine the thermocouple locations. Six chromel-alumel thermocouples were embedded in small holes at approximately 3 mm, 4 mm, 8 mm, 11 mm, 17 mm, and 34 mm from the centerline, Figure V.3. Earlier study showed that the fusion zone width is approximately 6.4 mm for a single pass, full penetration weld on a 3.0 mm sheet with a heat input of 310 J/mm (refer to Chapter III, Experimental Procedure); therefore, the fusion boundary is about 3 mm from the centerline. The same welding set-up and parameters were used for these GTA weldment.

The experimentally obtained temperature cycles are shown in Figure V.4a. These six HAZ thermal cycles were then individually simulated using a GLEEBLE on the T3 and T8 tempered base metal. The simulated zone width is approximately 9.5 mm. The GLEEBLE is a closed-loop device that utilizes the electrical resistance for controlled heating and applies a gas or liquid quench spray for controlled cooling of the specimen. Temperature control was provided by a chromel-alumel thermocouple percussion welded to the specimens. The temperature simulations are summarized in Figure V.4b. The highest peak temperature simulated was 853 K due to localized melting at the grain boundaries for the temperatures above the solvus. Henceforth, the thermally cycled specimens will be referred by its peak temperature and the respective temper, e.g. 443-T3 for the 443 K peak temperature on T3 tempered base metal.

All the specimens were made in the longitudinal direction and, after simulation, were machined into tensile specimens, schematically illustrated in Figure V.5. The thicknesses of the as-received base metal (BM) and the thermally cycled specimens in T3 and T8 tempers were 1.6 mm and 2.5 mm, respectively. After the thermocouple percussion weld was machined off (the percussion weld created a stress concentration in the specimen) the thicknesses of the thermally cycled specimen -T3 and -T8 were reduced to 1.3 mm and 2.0 mm, respectively. The initial set of the thermally cycled specimens was tensile tested using a 25.4 mm gage length, but these specimens failed in the base metal and not in the simulated region. To insure testing of the simulated region, an 8 mm gage length was machined within the original 25.4 mm gage length of the simulated specimens, Figure V.5c. The 25.4 mm gage length was used for the BM-T3 and -T8 specimens. The tensile tests were conducted at 293 K and 77 K.

Transmission electron microscopy (TEM) specimens were made from the BM-T8 and the simulated region of the thermally cycled specimens-T8 in the L-S direction. The foils were prepared from disks by mechanically polishing to 0.125 mm thickness and then jet-polishing using a potential of 20V in 20 vol-% nitric acid in methanol cooled to 247 K. The foils were viewed at 100 KV using a Philips EM 301. All the centered dark field (CDF) images are taken using a two-beam condition of a [110] zone axis. Energy dispersive spectroscopy (EDS) was performed on a scanning transmission electron microscope, Philips EM 400, to analyze the intermetallics composition.

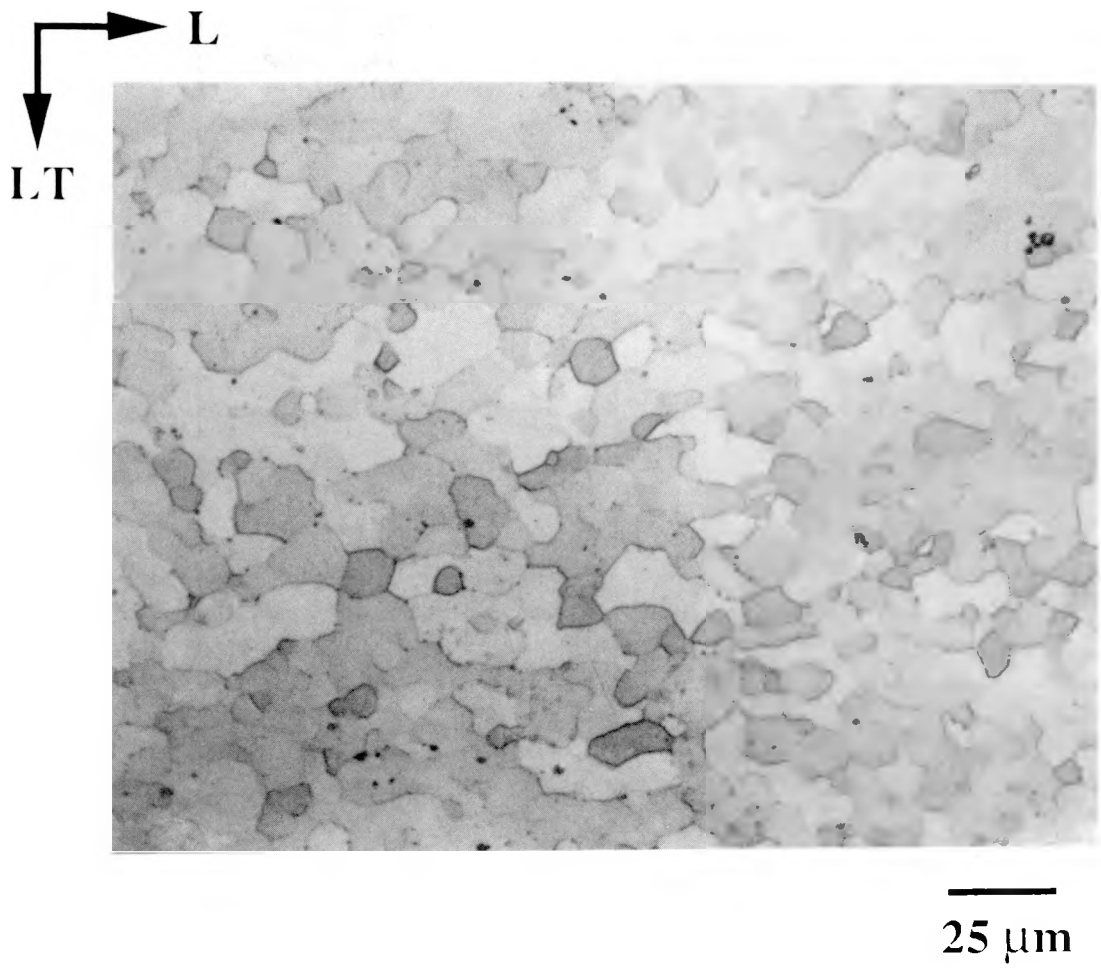

Figure V.2: Optical micrograph of a polished top surface of 2090-T8, showing an equiaxed microstructure with residual texture to the rolling direction. (XBB899-8169)

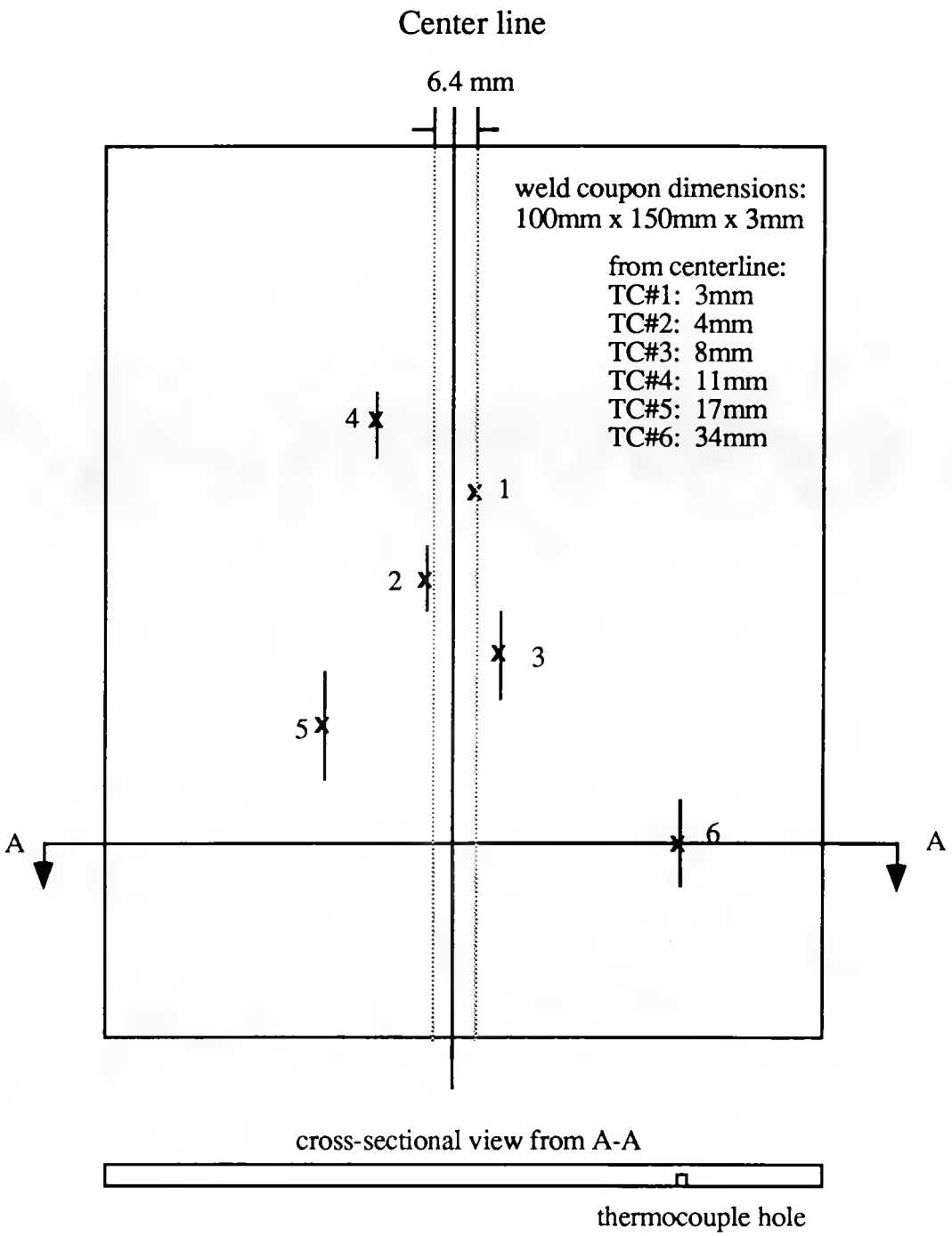

Figure V.3: A schematic diagram of weld coupon showing thermocouple locations. Dash lines represent the fusion boundaries. The cross-sectional view shows how the thermocouples were embedded.

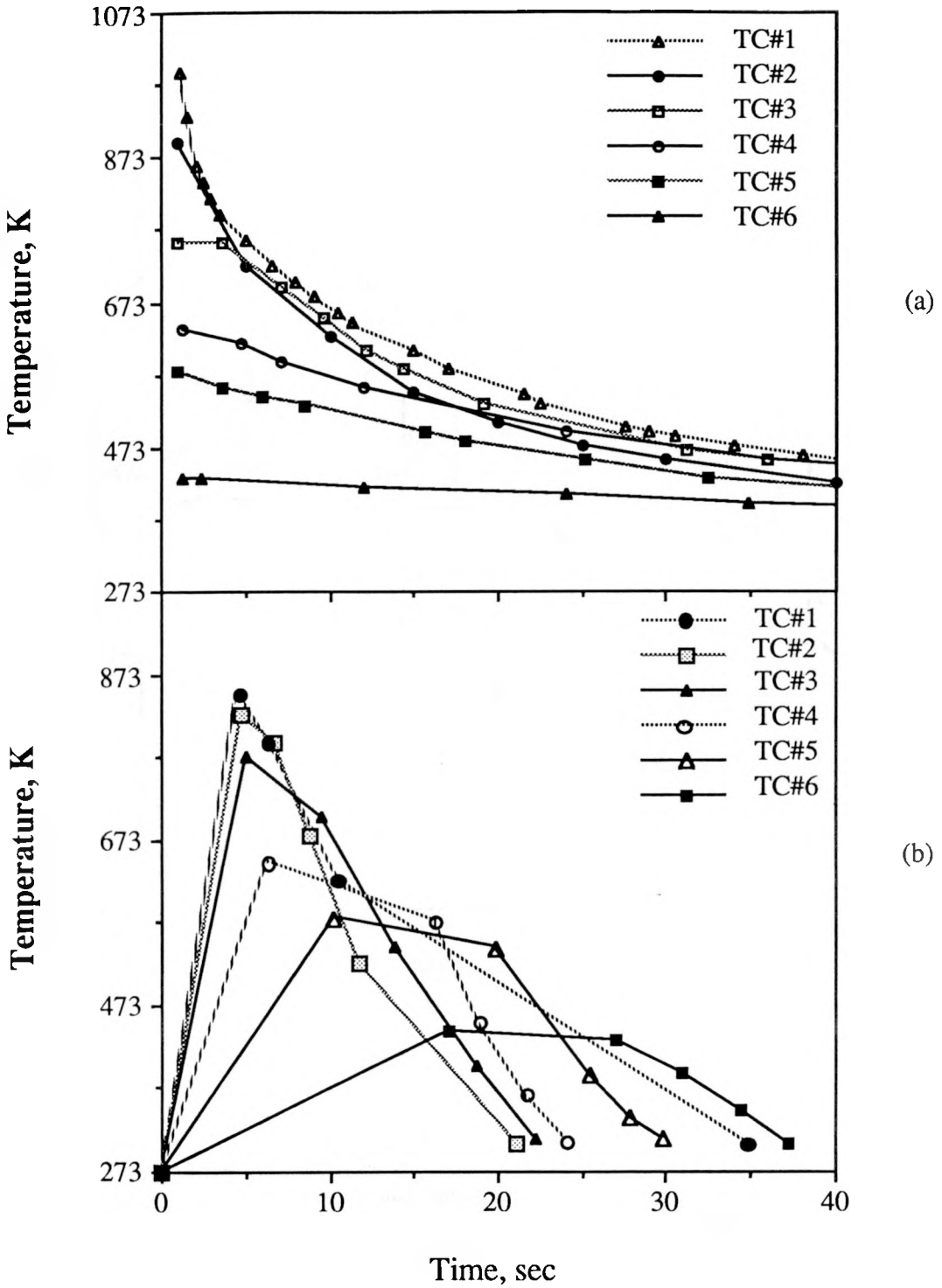

Figure V.4: a) Experimentally obtained heat affected zone temperature history, b) GLEEBLE thermal cycle simulations.

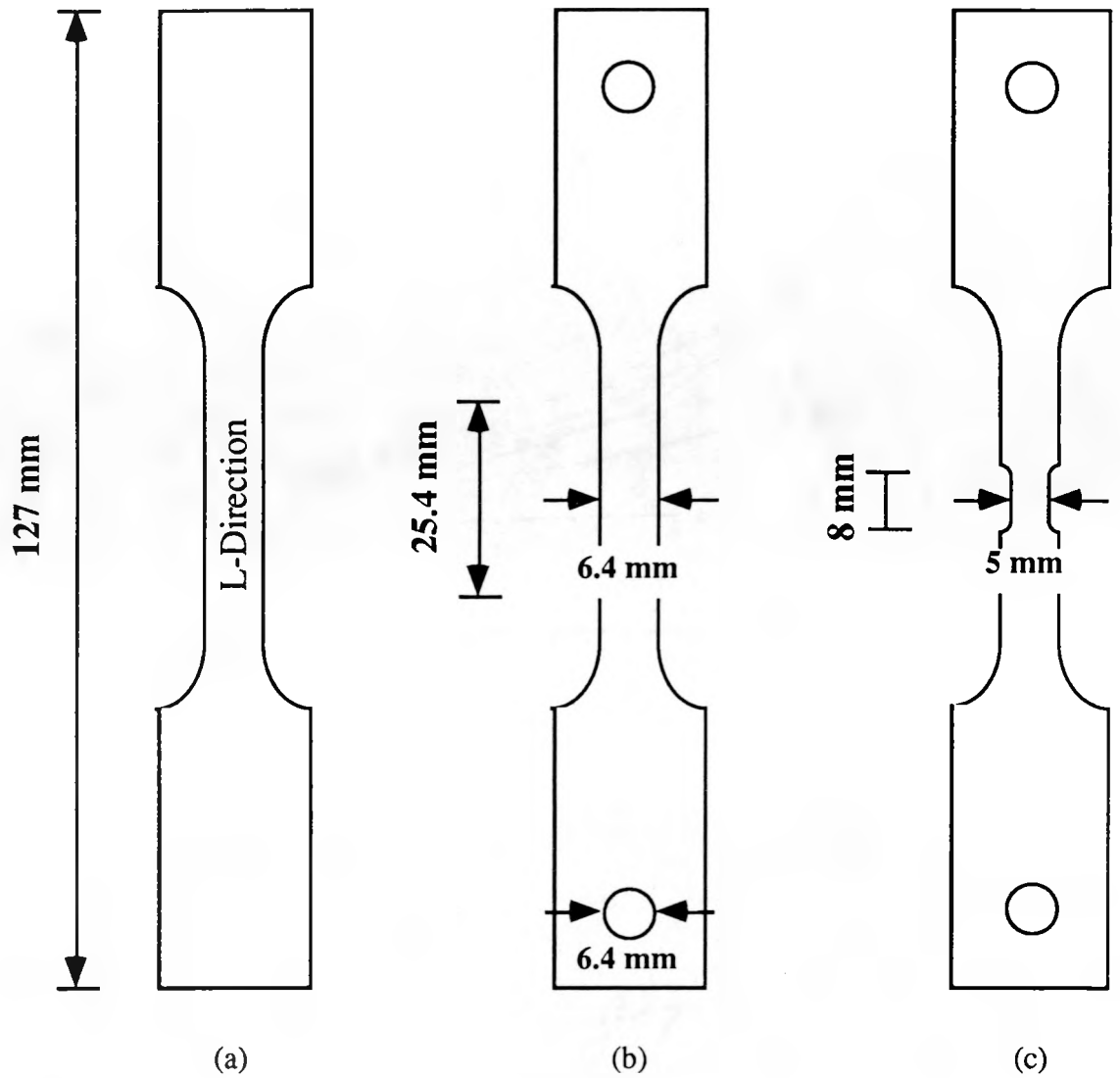

Figure V.5: Specimen configurations: a) GLEEBLE specimen, b) base metal tensile specimen with a 25.4 mm gage length, c) thermally cycled tensile specimen with a 8 mm gage length. All the specimens are made in the longitudinal orientation.

D. RESULTS

D.1 Transmission Electron Microscopy

The effects of various peak temperatures on the precipitation behavior are apparent from the evolution of selected area diffraction (SAD) patterns from the BM-T8, and the 578-T8, 648-T8, and 773-T8 in Figure V.6. The SAD patterns are from a [011] zone axis and an idealized SAD pattern is schematically illustrated in Figure V.6e. (The precipitates present in this work are the same as discussed earlier in the Section III.B.) The discrete superlattice reflections are from the δ'/β' precipitates. The streaks in the <100> directionsare from the thin θ' precipitates, and those in the <111> directions and the reflections at 1/3{113} are from the T_1 precipitates.

In comparison to the SAD pattern of the BM in Figure V.6a, the pattern of the 578-T8 in Figure V.6b shows more distinct T_1 streaks and reflections. With the 648-T8 in Figure V.6c, the T_1 streaks and reflections are the prominent features in the pattern, while the superlattice reflections are very faint. With the 773-T8 in Figure V.6d, the T_1 streaks and reflections have disappeared, and only the diffused superlattice reflections are present.

Figures V.7, V.8, and V.9 compare the size and distribution of the precipitates from the BM-T8, and the 443-T8 and 648-T8, respectively. The δ'/β' and T_1 CDF images are taken using the superlattice reflection and the edge-on variant of the T_1 phase, respectively. The CDF images of the BM and the 443-T8 in Figures V.7 and V.8, respectively, show no observable change in the size or the distribution of the δ' and T_1 precipitates, as both conditions reveal a homogeneous δ', a few β', and very fine T_1 platelets in the matrix and also at the subgrain boundaries. However, θ' precipitates are not visible in the δ' CDF image although the streaks in the <100> were present in the SAD of the BM.

With the 648-T8, the CDF image of superlattice reflection (Figure V.9a) shows only the β' in the matrix with T_2 precipitates at the boundaries (Figure V.9a and V.9b). With the dissolution of δ', the presence of more Li and combining that with a higher thermal energy leads to the growth of the equilibrium phases. As the size of T_1 increases in the matrix, so did the size of the T_1 and T_2 at the boundaries.

For peak temperatures above 773 K, all the strengthening phases have dissolved. Figure V.10 shows only the β' precipitates in the matrix with sparsely distributed spherical intermetallics (as indicated) and equilibrium phases at the boundaries and triple points. Qualitative results from the EDS indicate that the matrix is composed of, in wt-%, 95% Al and 5% Cu and the intermetallics are composed of 21% Cu, 3.5% Fe, and 2.5% Cl, the remainder being Al.

D.2 Tensile Properties

The effects of various peak temperatures on the 293 K and 77 K tensiles properties are summarized in Table V.1, and the ultimate tensile strength (UTS) and elongation are plotted with respect to its peak temperature in Figure V.11. The effects of base metal tempers and various peak temperatures are clearly seen by the differences in the strength and elongation. For the T3 tempered base metal, even the 443 K thermal excursion, which corresponds to aging temperature in 2090, had a deleterious effect on the strength, decreasing by 15%. For the T8 tempered base metal, the strength generally decreases with peak temperatures, although the strength of the 648-T8 showed a slight increase. As the strength decreased, the elongation increased.

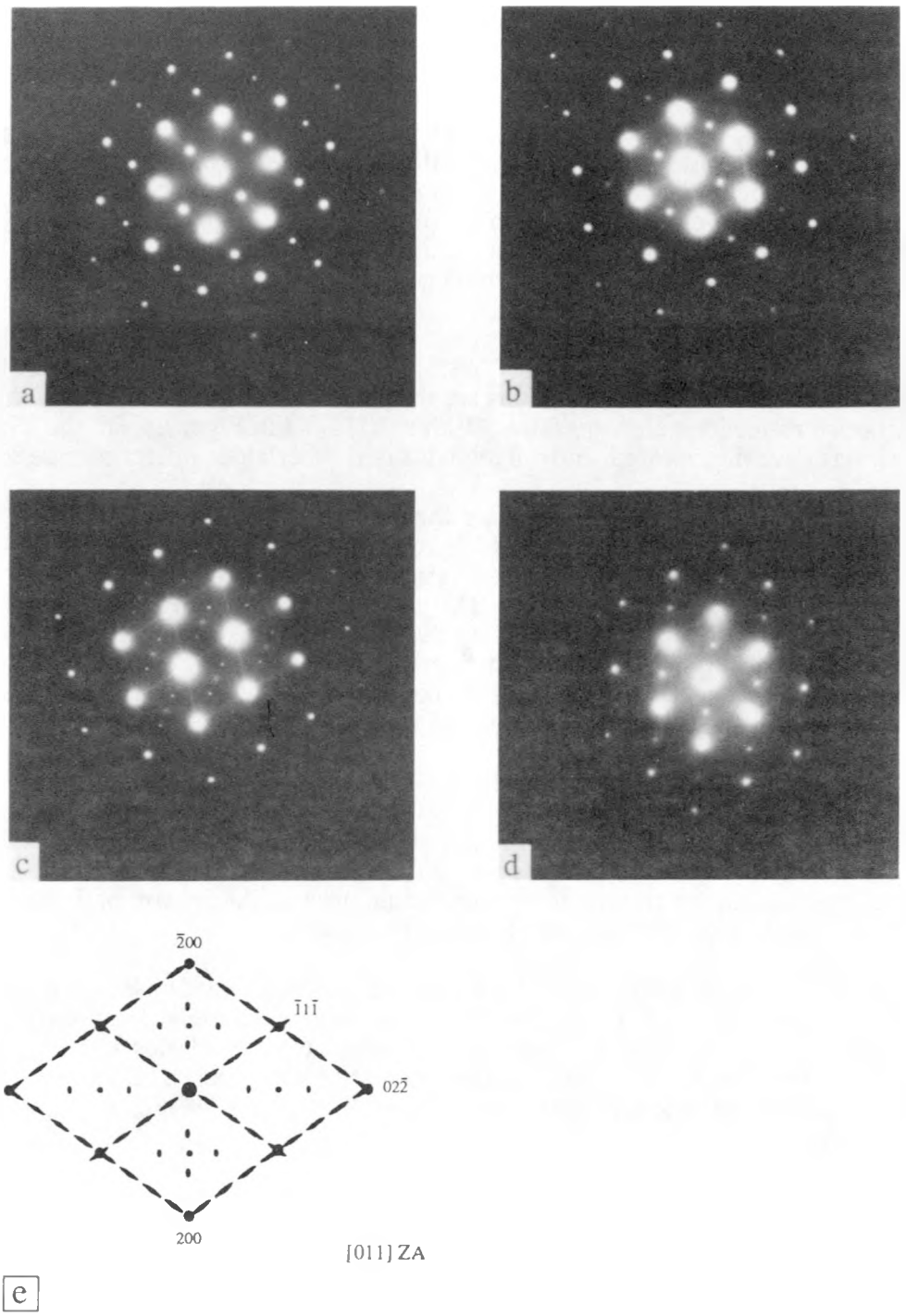

Figure V.6: TEM SAD patterns of a <110> zone axis from: a) base metal-T8, b) 578-T8, c) 648-T8, d) 773-T8, e) an idealized SAD pattern. The superlattice reflections are from δ' and β', and the streaks in <100> are from θ'. The streaks in <111> and the reflections at 1/3 {113} are from T_1. (XBB899-8170A)

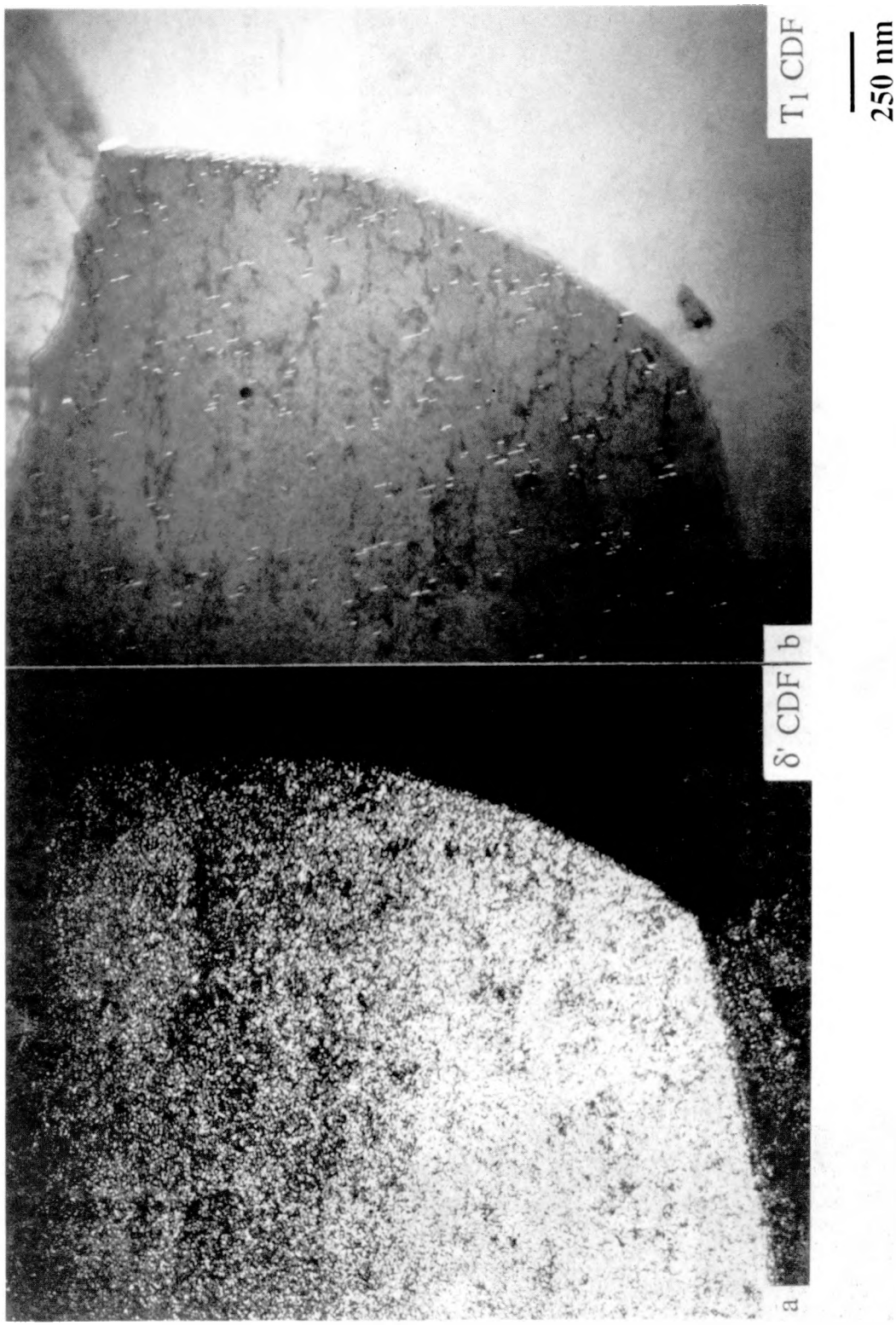

Figure V.7: TEM CDF images of 2090-T8: a) superlattice reflection, b) edge-on variant of T_1. (XBB899-8175)

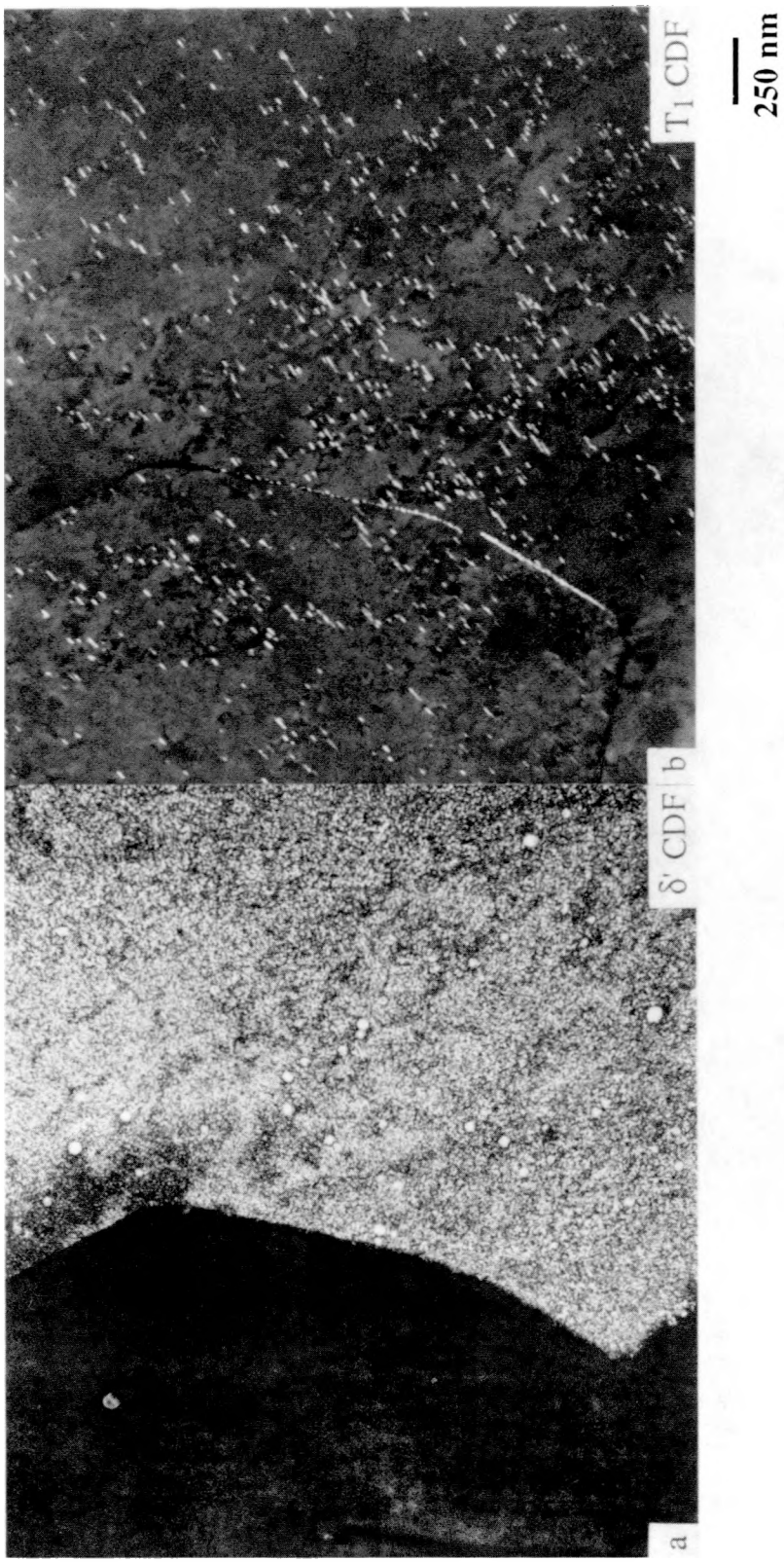

Figure V.8: TEM CDF images of 443-T8: a) superlattice reflection, b) edge-on variant of T_1. (XBB899-8176)

Figure V.9: TEM CDF images of 648-T8: a) superlattice reflection, b) edge-on variant of T_1. The T_2 precipitates are as indicated in both a) and b) (XBB899-8177)

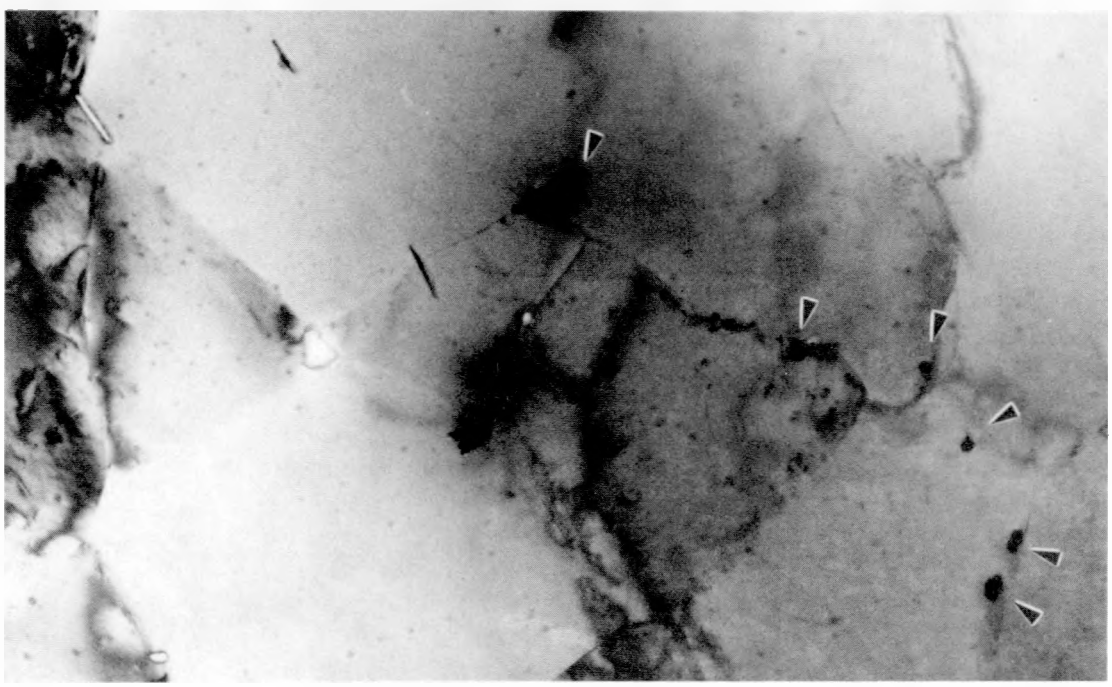

Figure V.10: TEM bright field image of 773-T8 showing mostly the β' dispersoids in the matrix with the spherical intermetallics (as indicated) and the equilibrium phases at the boundaries. (XBB903-2688)

Table V.1 HAZ tensile properties of the base metal and the thermally cycled specimens in T3 and T8 tempers tested at 293 K and 77 K.

Peak Temp. K(°C)	σ_{YS} MPa(ksi)	σ_{UTS}[1] MPa(ksi)	Elongation[2,3] %
Test Temp.: 293 K			
-T3			
BM	360(52)	440(64)	4.5[2]
443(170)	310(45)	380(55)	8.0[3]
578(305)	315(46)	415(60)	13.5[3]
648(375)	340(50)	440(64)	11.0[3]
773(500)	200(29)	340(49)[1]	11.5[3]
823(550)	230(33)	345(50)[1]	12.5[3]
853(580)	235(34)	355(52)	13.0[3]
-T8			
BM	500(72)	545(79)[1]	2.0[2]
443(170)	510(74)	535(78)	2.5[3]
578(305)	325(47)	425(61)	12.0[3]
648(375)	360(52)	439(64)	10.5[3]
773(500)	200(29)	345(50)	12.0[3]
823(550)	205(30)	360(52)	17.5[3]
853(580)	205(30)	355(51)	15.0[3]
Test Temp.: 77 K			
-T3			
BM	425(62)	560(81)	14.0[2]
443(170)	380(55)	510(74)	23.0[3]
578(305)	380(55)	495(72)	27.5[3]
648(375)	440(64)	545(79)	12.0[3]
773(500)	245(36)	455(66)	26.0[3]
823(550)	280(41)	470(68)	31.0[3]
853(580)	265(38)	476(69)	27.5[3]
-T8			
BM	530(77)	675(98)[1]	5.5[2]/10.0[3]
443(170)	540(78)	670(97)	9.5[3]
578(305)	395(57)	530(77)	17.0[3]
648(375)	405(59)	520(75)	11.0[3]
773(500)	240(35)	450(65)	25.0[3]
823(550)	250(36)	480(70)	33.5[3]
853(580)	245(36)	460(67)	33.0[3]

Note: Strengths given to nearest 5 MPa and elongations given to nearest 0.5%

[1] Fracture strength.

[2] 25.4 mm gage length.

[3] 8 mm gage length.

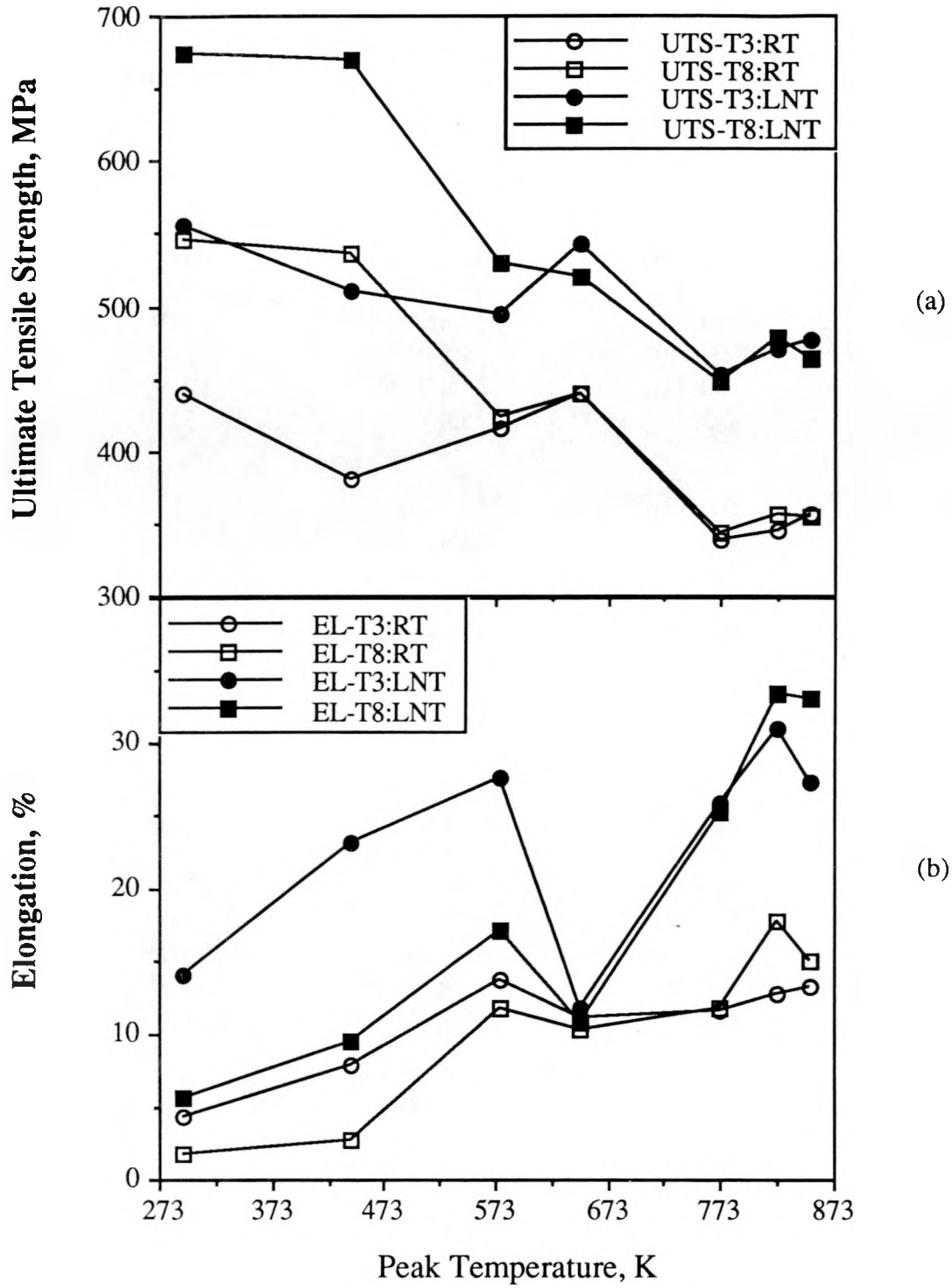

Figure V.11: 293 K and 77 K tensile properties of 2090 and the thermally cycled specimens with respect to the peak thermal cycle temperature: a) ultimate tensile strength, b) elongation. The base metal properties are plotted at 293 K.

The UTS of the thermally cycled specimens in the T3 and T8 started to coincide at 578 K and followed a similar trend with the peak temperature above 648 K. Thus, the base metal temper becomes irrelevant with the peak temperatures above 578 K. The strengths of the 773 K and above thermally cycled specimens were equivalent to those of the solution heat treated condition.

At 77 K, the strengths and elongation of both the base metal and thermally cycled specimens in the T3 and T8 tempers increased. Like at 293 K, the overall UTS of the T3 and T8 thermally cycled specimens followed a similar trend, but the actual strengths did not coincide until 773 K. With the peak temperatures from the 443 K to 853 K, the elongation of the T3 and T8 tempers increased from 23% to 31%, and 10% to 33%, respectively, except with the 648 K peak temperature where the elongation did not increase with decreasing temperature.

D.3 Fractography

Fracture surfaces of the BM-T8, and the 578-T8 and 773-T8 tested at 293 K changed with decreasing test temperature (Figure V.12), although all the specimens tested at 293 K failed mostly in single shear. The BM fracture surface in Figure V.12a reveals a mixed mode of failure consisting of smooth, transgranular regions with deformed grain surfaces and shallow dimples. The fracture surface of the 578-T8 in Figure V.12b shows a more planar, intergranular failure with dimples at the grain edges, in comparison to the BM fracture surface. The fracture surface of the 773-T8 in Figure V.12c exhibits predominantly void coalesced failure, and at higher magnification the grain boundary areas were found to be decorated with a fine dispersion of precipitates. Unlike the other fracture surfaces, the dimple morphology of the 773-T8 is deep and round and the grain boundaries are difficult to discern.

A transition in deformation was found with decreasing temperature. The specimens tested at 77 K failed mostly in double shear in comparison to the single shear at 293 K, and the fracture surfaces showed a distinct delamination in the through-thickness direction. In addition, the fracture surfaces of the BM and 578-T8 reveal well defined subgrain boundaries, unlike those at 293 K, as shown in Figure V.13a and V.13b. The fracture surface of the 578-T8 indicates mostly intergranular failure. Alternatively, the fracture surface of the 773-T8 in Figure V.13c consists primarily of dimpled regions with some delamination.

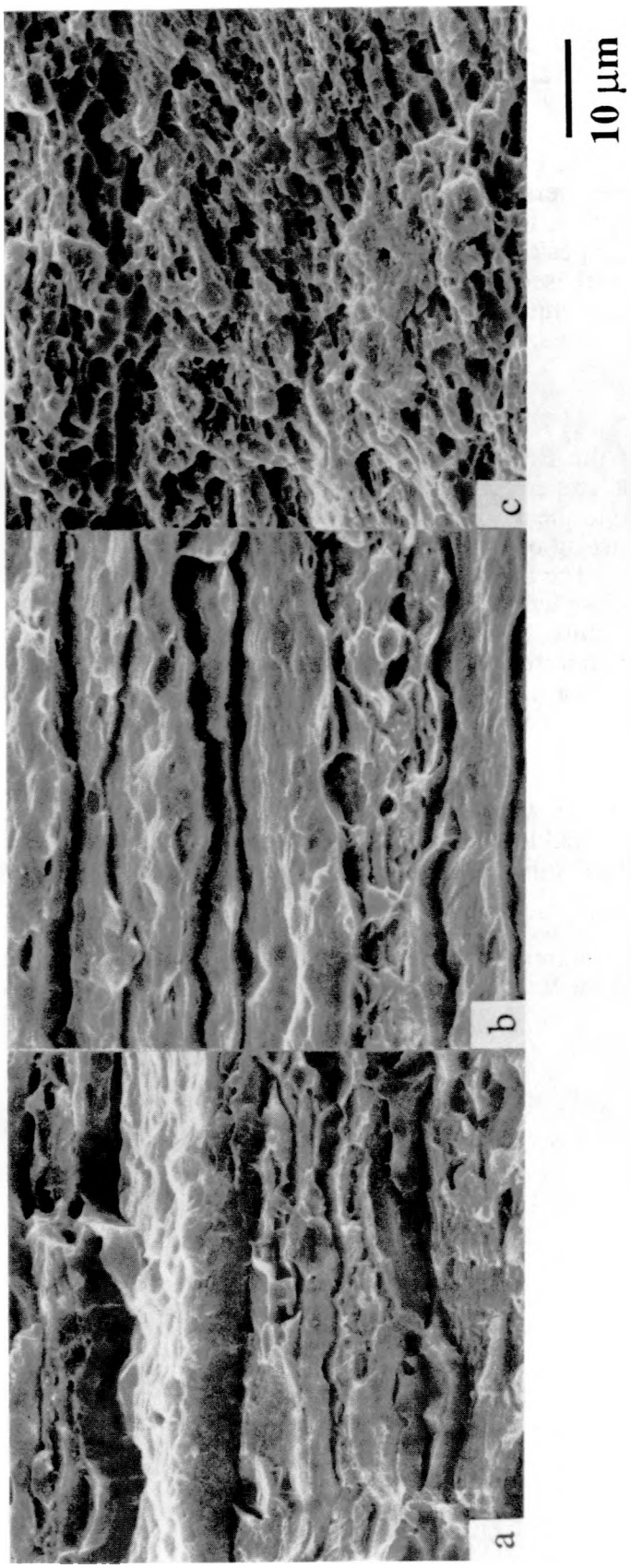

Figure V.12: SEM fractographs of the specimens tested at 293 K: a) 2090-T8, b) 578-T8, c) 773-T8. (XBB899-8173)

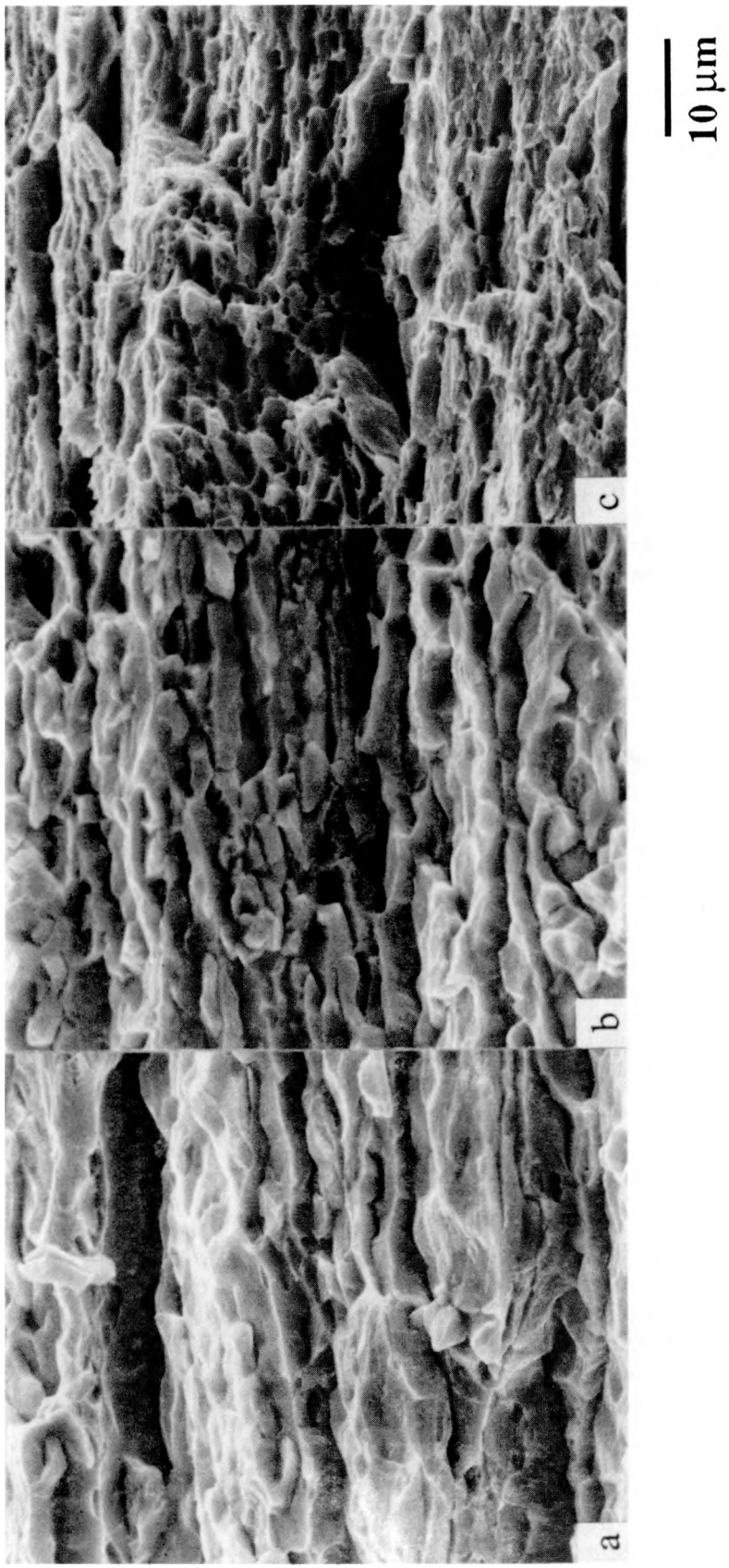

Figure V.13: SEM fractographs of the specimens tested at 77 K: a) 2090-T8, b) 578-T8, c) 773-T8. (XBB899-8174)

E. DISCUSSION

E.1 Effects of Thermal Cycles on Microstructure

A TEM investigation of the microstructures suggests that 2090 is highly sensitive to peak temperatures and these results agree closely with other microstructural studies on 2090 and 8090 alloys. Tosten, et. al.[1988] found that in the as-quenched condition, the microstructure exhibits the diffused superlattice reflections due to the inhomogeneous dispersion of β' precipitates and very fine (~ 2-4 nm diameter) δ' precipitates. Rioja and Ludwiczak [1986], utilizing differential scanning calorimetry (DSC), have indicated that the dissolution of δ' takes place between 473 K to 533 K, depending on the size of δ', and that T_1 and T_2 are the only phases present at 652 K for both the as-quenched and aged samples.

A similar DSC study by Mukhopadhyay, et al. [1987] has also shown that the 443 K exothermic reaction in the specific heat capacity curve of Al-Li alloy is attributed to δ' precipitation or the growth of δ' from that present due to quenching. Moreover, 443 K represents the temperature at which the driving force for the precipitation and diffusion is optimized, and therefore the temperature for maximum precipitation. From 473 K to 523 K, the volume fraction of δ' in the aged sample decreases by a factor greater than 2 to maintain the equilibrium concentration of Li in solution [Mukhopadhyay, et al., 1987].

Hardy and Silcock [1955-56] used x-ray analysis to determine the ternary phase diagram of Al-rich Al-Cu-Li alloys at 623 K and at 773 K. For the 2090 in this study, T_1 and T_2 are the only phases present at 623 K, and the 2090 is within the limits of Al solid solution at 773 K. At 773 K and above, Cu and Li additions are in solid solution except for the Fe-containing intermetallics. Upon cooling, a combination of the high diffusion rate of Cu (and Li) and the Fe-containing intermetallics already present at the boundaries leads to the growth of the intermetallics and the heterogeneous precipitation of the equilibrium phases.

Other studies [Miller, et al.,1986; Owen, et al, 1986] have characterized the grain boundary precipitates as δ- and T- phases, or Fe-Cu rich intermetallics in 2090, and S-phase and Fe-Cu rich intermetallics in 8090. In the present work, the presence of Cl in the intermetallics results from the use of Cl gas as a flux during casting [Gu, et al.,1985; Dorn, et al., 1950; Rioja, 1989]. Chlorine is known to form intermetallics with Cu and other trace elements [Rioja, 1989].

E.2 Effects of Thermal Cycles on Properties

E.2.1 293 K Properties

The overall UTS curves of the BM-T3 and -T8 follow closely to the hardness profiles of the respective GTA weldments. The problem region in the weldment is the region that undergoes a thermal cycle above 773 K, such as the partially melted region and the fusion boundary. This is due to dissolution of the strengthening phases in the matrix and the formation of equilibrium phases and intermetallics at the boundaries. The EB weldments in the as-welded and solutionized conditions have failed at the fusion boundary and at the heat affected zone, respectively.

The microstructural changes associated with the peak temperatures have a measurable effect on the properties. The T3 tempered base metal lacks the volume fraction and homogeneity of the strengthening precipitates, as compared to the T8 tempered base metal, resulting in more homogeneous deformation [Jata and Starke, 1986]. However, due to the difference in thermomechanical processing of this 2090-T8, the size and the volume

fraction of T_1 are too small to be a potent strengthener. The average diameter of T_1, after aging for 18 hours at 463 K, has been measured in the TEM by Tosten [1988] as 125 nm and the volume fraction [Huang and Ardell, 1987] of T_1 is 10% to 25% that of δ'.

The δ' phase is a coherent ordered phase and as such, dislocations can easily shear the δ' precipitates as deformation progresses [Gregson and Flower,1985; Sanders and Starke, 1982]. An initial unit dislocation forms an antiphase boundary within the sheared δ', making it easier for second dislocation to shear through and to restore ordered δ'. As more super-dislocations form with deformation, the effective area of δ', and thus the strengthening potential of δ', is reduced. Consequently, intense planar slip causes dislocation pile-up at the grain boundaries. A combination of the boundary precipitates and localized stress concentrations caused by dislocation pile-up at the boundaries promotes premature failure in alloys primarily strengthened by δ'. The 293 K elongation of the BM-T8 is only 2%.

The decrease in strength of the 443-T3 can be attributed to the growth of a larger number (or larger size) of δ' present as-quenched [Mukhopadhyay, et al., 1987]. With the 578 K peak temperature and above, a combination of the dissolution of δ' Cu in solid solution, and additional thermal energy enhance the growth of equilibrium phases in the matrix as well as the boundaries, but the volume fraction of T_1 is too low to be a dominant strengthener. Although the strengths of both the 648-T3 and -T8 increase, they are equivalent to or lower than that of the initial condition, respectively. With the dissolution of δ', the propensity to planar slip lessened which results in a higher elongation. However, due to the growth of the equilibrium phases at the boundaries, the elongation of the 648-T3 and -T8 is the lowest for the 578 K and above thermally cycled specimens.

With the temperature cycles above 773 K, the cooling rate and its quench path are important factors in controlling the grain boundary and matrix precipitation [Shakesheff, et al., 1989; Sawtell, 1984], since they affect the vacancy supersaturation and the loss of solutes. The quench path of the 773 K thermal cycle is such that a slower cooling between 673 K and 773 K may have helped to precipitate intermetallics and equilibrium phases at the boundaries. Compared to the 823 K and 853 K thermally cycled specimens, the strength and elongation of the 773 K thermally cycled specimens were the lowest.

E.2.2 77 K Properties

At the lower temperature, the increase in strength of the base metal is attributed to a decreased propensity for planar slip. Less thermal activation energy is available for dislocation movement, and as a result, the increase in dislocation interaction creates more uniform deformation [Glazer, et al., 1987]. Moreover, the change from a single shear to a double shear fracture at 77 K indicates that multiple slip systems are involved in deformation. There also appears to be more dislocation interaction with T_1 at the subgrain boundaries, where the fracture surfaces of the BM-T8 and 578-T8 tested at 77 K revealed more subgrain separation. Since both the T_1 precipitates and dislocations are oriented in the same {111} plane at 293 K, the dislocations can easily shear through on the broad face of T_1 to another subgrain [Gregson and Flower, 1985] or can easily cross-slip to avoid T_1. The deformation study [Jata and Starke, 1986] has shown that the slip bands are most often continuous across the subgrains. The subgrain boundaries were difficult to distinguish at 293 K. But at 77 K, with limited dislocation movement and multiple slip systems operating, the orientation of the dislocations and the T_1 precipitates may not always be favorable at the boundary and deformation may cause a dislocation pile-up to occur. Subsequently, the dislocation interaction causes stress concentrations and leads to subgrain separation.

In addition to T_1 at the subgrain boundaries, the presence of T_2 precipitates at the grain boundary creates a strain incompatibility between the incoherent, hard precipitates and the adjacent matrix [Vitatek and Chell, 1980; Owen, et al., 1986; Vasudevan and Doherty, 1987], providing nucleation sites for microvoids which ultimately lead to failure. The stress and strain incompatibility between the incoherent precipitate and the matrix are greater at lower temperature [Vasudevan and Doherty, 1987]. Thus, the fracture mode of the base metal and 578-T8 was predominantly intergranular.

F. CONCLUSIONS

The effects of various HAZ peak temperatures on the microstructure and properties of 2090-T3 and -T8 tested at 293 K and 77 K have been investigated.

1. The difference in properties of the heat affected zone and the base metal is primarily caused by the dissolution of strengthening phases. At 578 K, degradation of the strengths occurs due to dissolution of δ' phase and at 773 K, dissolution of T_1 phase. The thermal cycles to 648 K leads to an observable growth of T_1 phase, but the volume fraction is too low to be an effective strengthener. Minimizing time at temperatures between 673 K-773 K is crucial in limiting the growth of equilibrium phases and intermetallic formation at the grain boundaries.

2. At the 293 K test temperature, the base metal tempers become irrelevant for the peak temperatures above 578 K, as the UTS curves of both the BM-T3 and -T8 coincide and follow the same trend up to the 853 K.

3. At the 77 K test temperature, the strength and elongation of the base metal and the thermally cycled specimens in the T3 and T8 tempered conditions follow the trend seen at 293 K, and exhibit at higher strengths and elongations.

VI. SUMMARY

2090-T81 alloy is of interest to the aerospace industry because of its combination of low specific density, high elastic modulus, and excellent cryogenic properties. The weldability of this alloy has been a concern since some cryogenic applications require welding. The task of this work is to determine the weldability of 2090, with emphasis on understanding the fusion zone and the heat affected zone microstructural behavior.

Ideally, compatibility in strength, toughness and ductility is desired between the base metal and the weld. This compatibility is very difficult to obtain in practice for the following reasons. First, in the fusion zone, prior thermomechanical processing of the base metal is erased during welding, and the weld properties are governed by the constitutional undercooling of the welding process, which consequently determines the microstructure and solute distribution in the fusion zone. In the as-welded condition, the weld strength is primarily determined by the Cu and very fine δ' and the elongation is influenced by the dendrite morphology. The EB welds have overall better properties than that of the GTA welds.

Second, due to the nature of solidification, the post-weld aged fusion zones lack the precipitates, size, volume fraction, and homogeneity of the base metal. In the peak-aged condition, the precipitation of T_1 is limited. The T_1 precipitates are found either in the vicinity of other intermetallics or at the boundaries. In addition, the composition of 2090 is such that enough Cu and Li are present to coat and form a continuous film around the dendrite boundaries. As the strength of the dendrite matrix increases and exceeds the strength of the dendrite boundary, the weldment fails prematurely. The joint efficiencies of EB and GTA weldments are 75% and 55% at 293 K and 75% and 50% at 77 K, respectively, with low weldment elongations.

Third, the strength compatibility between the base metal and weld can be achieved in the solutionized condition. However, it is difficult to attain the critical quench rate in real application because of the size of the weldment.

Fourth, Cu and Mg combinations have been added to the 2090 fusion zone to improve the weld strength. The strength mismatch continues to exist due to the difference in strengthening mechanism: solid solution strengthening in the fusion zone and precipitation strengthening in the base metal. As a result, the ultimate tensile strength of the as-welded weldments is only 50% of the base metal yield strength, and deformation and failure continue to occur in the softer fusion zone.

A weldment elongation increases substantially with increasing Cu content in the fusion zone. At the 77 K test temperature, a 6 Cu addition has the best combination of UTS and elongation of all the weldments tested. Magnesium additions to 2090 change the fusion zone microstructure to a more cellular dendritic structure, which affects the distribution of Cu segregation at the boundaries. The Mg welds show higher yield strengths, but the Cu-Mg combination leads to brittle, interdendritic fractures at both the 293 K and 77 K test temperatures.

At this time, the strength of the fusion zone is still lower than that of the heat affected zone, and thus the heat affected zone is not a major concern. However, because 2090 is a precipitate-strengthened alloy, any thermal cycle will affect the precipitation behavior. The investigation of HAZ peak temperatures on the microstructure and properties of 2090-T3 and -T8 tested at 293 K and 77 K has shown that the difference in properties of the heat affected zone and the base metal is primarily caused by the dissolution of strengthening phases. At 578 K, the strength degrades due to dissolution of δ' phase

and at 773 K, dissolution of T_1 phase. A thermal cycle to 648 K causes the growth of the equilibrium phases: T_1 at both the matrix and the subgrain boundaries, and T_2 at the grain boundaries. The 648 K thermally cycled specimens show a slight increase in the strength, but the elongation is the lowest in comparison to other thermally cycled specimens.

The next problem region in the weldment will be the region that undergoes a thermal cycle above 773 K, such as the partially melted region and the fusion boundary. This is due to dissolution of the strengthening phases in the matrix and the formation of equilibrium phases and intermetallics at the boundaries. The EB weldments in the as-welded and solutionized conditions have failed at the fusion boundary and at the heat affected zone, respectively. The best way to prevent the grain boundary liquation or HAZ cracking is to utilize fast cooling process, like EB welding or GTA welding on a water-cooled chill block to enhance the cooling rate.

VII. FUTURE WORK

The results of this work suggest that there are limited ways to improve the weld strength. One obvious way such as post-weld heat treatment however is not feasible due to the continuous film formation at the dendrite boundaries. The next possible way to increase the weld strength is to add alloy additions to the fusion zone. Even with Cu and Mg additions as the solid solution strengthener, the strengths of the as-welded welds are limited in comparison to the precipitate-strengthened base metal.

However, there has been some success in improving the weld strength with small additions of Mg+ Ag to the fusion zone [Polmear, 1964; Auld and Vietz, 1968]. Silver is a very potent solid solution strengthener in Al. Unlike other elements, such as Cu or Mg, there is no lattice strain associated with Ag in the Al matrix. The strengthening mechanism is primarily associated with the difference in valence electrons between Ag and Al [Dorn. et al., 1950]. Al-Cu-Mg-Ag addition to 2090 should be investigated as a possible filler addition to 2090.

VIII. ACKNOWLEDGEMENT

Very special thank you is extended to Prof. J.W. Morris, Jr. for having faith in my abilities. I like to express gratitude to my qualifying examination committee members, Profs. R.O. Ritchie, G. Thomas, D.A. Dornfeld, and Dr. E.N.C. Dalder, and especially, Profs. R.O. Ritchie and D.A. Dornfeld for reviewing this dissertation.

I would like to thank my friends in Morris Group past and present for their support and encouragement. I am especially indebted to J.W. Chan for always being there to provide me with a helping hand. My other helping hands were S. Miyasato and E.L. Bradley, III. Thanks!

I would like to thank ALCOA for providing the materials and for providing the specimens for the heat affected zone study, and B.L. Olson and D. Hoffman of Lawrence Livermore National Laboratory for making the electron beam weldments. This work was funded by the Director, Office of Energy Research, Office of Basic Energy Science, Material Sciences Division of the U.S. Department of Energy under Contract No. DE-AC03-76SF00098.

Loving thanks are extended to my husband, Seifu, for encouraging me to think positive and for sharing my joys and sorrows. And I will always be grateful to my parents for providing me with the opportunities to continue my education.

IX. REFERENCES

AWS Welding Handbook, C. Weisman, ed., vol. 1, 7th edition, American Welding Society, USA, 1976.

Ahmad, M. and T. Ericsson: *Scripta Metall.*, vol. 19, pp. 457-462, 1985.

Auld, J.H. and J.T. Vietz: *The mechanism of Phase Transformations in Crystalline Soliss*, Proc. Int. Symp., Institute of Metals, London, pp. 77-79, 1968.

Balaguer, J.P., D. W. Walch, and E.F. Nippes: *Weld. J.*, vol. 68, pp. 253s-261s, 1989.

Bartage, C., M.H. Tosten, P.R. Howell and E. R. Ryba: *J. Mat. Sci.*, vol. 22, pp. 1663-1669, 1987.

Borland, J.C.: *British Weld. J.*, vol. 8, pp. 508-512, 1960.

Ceresara, S., A. Giarda and A. Sanchaz: *Phil. Mag.*, vol. 35, pp. 97-110, 1977.

Clyne, T.W. and G.J. Davies, *TMS Proc. Int. Conf. Solidification*, pp. 275-278, 1977.

Cross, C.E., D.L. Olsen, G.R. Edwards and J.F. Capes: *Aluminium-Lithium Alloys II*, Proc. of Aluminum-Lithium Conf., eds. T.H. Sanders, Jr. and E.A. Starke, Jr., AIME, pp. 675-682, 1983.

Dew-Hughes, D., E. Creed and W.S. Miller: *Mat. Sci. Tech.*, vol. 4, pp. 106-112, 1988.

Dollar, M. and A.W. Thompson: *Acta Metall.*, 35, vol. 1, pp. 227-235, 1987.

Domult, S.D.: Ph.D. Dissertation, Carnegie-Mellon University, 1983.

Dorn, J.E., P. Pietrokowsky and T.E. Tietz: *J. of Metals*, vol. 188, pp.933-943, 1950.

Dvornak, M.J., R.H. Frost and D.L. Olson: *Weld. J.*, vol.68, pp. 327s-335s, 1989.

Edward, M.R. and V.E. Stoneham: *J. de Physique*, Proc. 4th Int. Al-Li Conf., eds. G. Champier, B. Dubost, D. Miannay and L. Sabetay, les editions de physique, France, vol. C3, pp. 293-299, 1987.

Fricke, W.G. and M.A. Przystupa: *Mat. Sci. Tech.*, vol. 31, 1989.

Glazer, J., S.L. Verzasconi, R.R. Sawtell and J.W. Morris, Jr.: *Metall. Trans. A*, vol. 18A, pp. 1695-1701, 1986.

Glazer, J: Ph.D. Dissertation, University of California, Berkeley, 1989.

Graf, M and E. Hornbogen: *Acta metall.*, vol. 25, pp. 883-889, 1977.

Gregson, P.J. and H.M. Flower: *Acta metall.*, vol. 33, pp. 527-537, 1985.

Gregson, P.J. and H.M. Flower: *Mat. Sci. Tech.*, vol 3, pp. 81-90, 1987.

Gu, B.P., G.L. Liedl, T.H. Sanders, Jr. and K. Welpmann: *Mat. Sci. Eng.*, vol. 76, pp. 147-157, 1985

Hardy, H.K. and J.M. Silcock: *J. Inst. Metals*, vol. 84, pp. 423-428, 1955-56.

Huang, J.C. and A.J. Ardell: *J. de Physique*, Proc. 4th Int. Al-Li Conf., eds. G. Champier, B. Dubost, D. Miannay and L. Sabetay, les editions de physique, France, vol. C3, pp. 373-383, 1987.

Hunt, W.H.: ALOCA ALTC Division Report 56-83-AH417, 1983.

Ishchenko, A. Ya., A.D. Vasil'ev and S.Z. Stasyuk: *Adv Cryo. Eng. Mat.*, vol. 26, pp. 219-226, 1982.

Jata K.V. and E.A. Starke, Jr.: *Metall. Trans. A*, vol. 17A, pp. 1011-1026, 1986.

Jensrud, O. and N. Ryum: *Mat. Sci. Eng.*, vol. 64, pp. 229-236, 1984.

Kaufman, J.G. and E.W. Johson: *Adv. Cryo. Eng.*, vol. 6, pp.637-649, 1960.

Khachaturyan, A.G., T.F. Lindsey and J.W. Morris, Jr.: *Metall. Trans. A*, vol. 19A, pp.249-258, 1988.

Kramer, L.S., F.H. Heubaum and J.R. Pickens: *Al-Li Alloy*, Proc. of Fifth Int'l Al-Li Conf., eds. T.H. Sanders, Jr. and E.A. Starke, Jr., Mat. Comp. Eng. Pub. Ltd., UK, vol. III, pp.1415-1424, 1989.

Lees, K.C.G.: *J. Inst. Metals*, vol. 72, p. 343, 1946.

Lippold, J.C.: *Al-Li Alloy*, Proc. of Fifth Int'l Al-Li Conf., eds. T.H. Sanders, Jr. and E.A. Starke, Jr., Mat. Comp. Eng. Pub. Ltd., UK, vol. III, pp. 1365-1375, 1989.

Ludtka, G.M and D.E. Laughlin: *Metall. Trans. A*, vol. 13A, pp. 411-425, 1982.

Marsico, T.A. and R. Kossowsky: *Al-Li Alloy*, Proc. of Fifth Int'l Al-Li Conf., eds. T.H. Sanders, Jr. and E.A. Starke, Jr., Mat. Comp. Eng. Pub. Ltd., UK, vol. III, pp. 1447-1456, 1989.

Martukanitz, R.P., C.A. Natalie, and J.O. Knoefel: *J. of Metals*, vol. 39, pp. 38-42, 1987.

Miller, W.S., J. White and D.J. Lloyd: *Al Alloy-Physical and Mechanical Properties*, Proc. Int'l. Conf., eds. E.A. Starke, Jr. and T.H. Sanders, Jr., Eng. Mat. Advisory Service LTD., vol. III, pp. 1799-1836, 1986.

Miller, W.S., M.P. Thomas, D.J. Lloyd and D. Creber: *Mat. Sci. Tech.*, vol. 2, pp. 1210-1216, 1986.

Mukhopadhyay, A.K., C.N.J. Tite, H.M. Flower, P.J. Gregson, and F. Sale: *J. de Physique*, Proc. 4th Int. Al-Li Conf., eds. G. Champier, B. Dubost, D. Miannay and L. Sabetay, les editions de physique, France, vol. C3, pp. 439-445, 1987.

Nelson, F.G, J. G. Kaufman and E.T. Wanderer: *Adv. Cryo. Eng*, vol. 14, Plenum Press, pp. 71-82, 1969.

Noble, B. and G.E. Thompson: *J. Mat. Sci.*, vol. 6, pp.114-120, 1971.

Nock, Jr. J.A., M. Holt and D.O. Sprowls: *Metal Progress*, 1961.

Owen, N.J., D.J. Field and E.P. Butler: *Mat. Sci. Tech.*, vol. 2, pp. 1217-1222, 1986.

Polmear, I.J.: *Met. Trans.*, vol. 230, pp. 1331-1339, 1964.

Pickens, J.R.: *J. of Mat. Sci.*, vol. 20, pp.4247-4258, 1985.

Pumphrey W.I. and J.V. Lyons: *J. Inst. Metals*, vol. 74, pp. 439-455, 1948.

Pumphrey, W.I. and P.H. Jennings: *J. Inst. Metals*, vol. 75, pp. 235-256, 1948.

Raman, K. S., E.S. D. Das and K.I. Vasu: *Scripta Metall.*, vol 4, pp. 291-293, 1970.

Rioja, R.J., and E.A. Ludwiczak: *Aluminium-Lithium Alloys III*, Proc. Aluminum-Lithuim Conference, eds. C. Baker, P.J. Gregson, S.J. Harris, and C.J. Peel, The Institute of Metals, pp. 471-482, 1985.

Rioja, R.J., P.E.Bretz, R.R.Sawtell, W.H. Hunt and E.A. Ludwiczak,: *Aluminum Alloys Their Physical and Mechanical Properties*, Proc. Int'l. Conf., eds. E.A. Starke, Jr. and T.H. Sanders, Jr., Eng. Mat. Advisory Service LTD., vol. III, pp. 1781-1797, 1986.

Rioja, R.J.: personal communication, ALCOA, ALCOA Center, PA, 1989.

Sanders, Jr. T.H. and E.A. Starke, Jr.: *Acta metall.*, vol. 30, pp. 927-939, 1982.

Savage, W.F., C.D. Lundin and A.H. Aronson: *Weld. J.*, vol. 44, pp. 175s-181s, 1965.

Savage, W.F. and A.H. Aronson: *Welding Journal*, vol. 45, pp. 85s-89s, 1966.

Sawtell, R.R.: *Aluminium*, vol. 3, pp.198-202, 1984.

Shakesheff, A.J., D.S. McDarmaid, and P.J. Gregson: *Mat. Letters*, vol. 7, pp. 353-358, 1989.

Spencer, D., R. Mehrabian and M.C. Flemings: *Metall. Trans. A*, vol. 3, p. 1925, 1972.

Sunwoo, A.J. and J.W. Morris, Jr.: *Al-Li Alloy*, Proc. of Fifth Int'l Al-Li Conf., eds. T.H. Sanders, Jr. and E.A. Starke, Jr., Mat. Comp. Eng. Pub. Ltd., UK, vol. III, pp.1481-1487, 1989.

Sunwoo, A.J. and J.W. Morris, Jr.: *Weld. J.*, vol. 68, pp. 262s-268s, 1989.

Tosten, M.H., A.K. Vasudevan and P.R. Howell: *Metall. Trans. A*, vol.19A, pp. 51-66, 1988.

Tosten, M.H., A.K.Vasudevan. and P.R. Howell: *Aluminium-Lithium Alloys III*, Proc. Aluminum-Lithuim Conference, eds. C. Baker, P.J. Gregson, S.J. Harris, and C.J. Peel, The Institute of Metals, pp. 490-495, 1985.

Van Stone, R.H.,T.B. Cox, J.R. Low, Jr. and J.A. Psioda: *Int'l Metals Rev.*, vol.30, pp. 157-179, 1985.

Vasudevan, A.K. and R.D. Doherty, *Acta metall.*, vol. 35, pp. 1193-1219, 1987.

Vitek, V. and G.G. Chell: *Dislocation Modelling of Physical System*, Acta-Scripta Metall. Conf., eds. M.F. Ashby, R. Bullough, C.S. Hartley and J.P. Hirth, Pergamon Press, pp. 92-109, 1980.

Wu, K.C., T.D.Byun and G.R. Turk: Northrop Internal Report, 1987.

Zacharia, T. and D.K. Aldun: *Weld. J.*, vol. 67, pp. 281s-288s, 1988.